Field, Experimental and Numerical Investigations into the Mechanisms and Drivers of Lateral Erosion in Bedrock Channels

A DISSERTATION
SUBMITTED TO THE FACULTY OF
UNIVERSITY OF MINNESOTA
BY

Theodore Kent Fuller

IN PARTIAL FULFILLMENT OF THE REQUIREMENTS
FOR THE DEGREE OF
DOCTOR OF PHILOSOPHY

Christopher Paola and Karen Gran, Co-Advisers

January, 2014

Acknowledgements

Thank you to Karen Gran, Chris Paola and Leonard Sklar for taking me on as one of their own graduate students in the middle of my dissertation and for guiding me through this long journey. The experimental and numerical modeling aspects of this dissertation could not have been completed without the talent and time that Karen, Chris and Leonard have contributed. A traineeship from NSF's IGERT program (Award# 0504195) and a research assistantship from the National Center for Earth-surface Dynamics (an NSF Science and Technology Center) provided financial support that allowed me to conduct the research presented here.

Lesley Perg, my initial faculty adviser, conceived much of the sampling scheme on which the field study is based. Lesley also provided her expertise on the laboratory procedures associated with processing cosmogenic isotope samples. Jane Willenbring was an integral part of the success of the field study. She provided laboratory expertise in the processing of ^{10}Be samples, initiated the incorporation of OSL samples into our study and helped collect ^{10}Be and OSL samples in the field. Ken Lepper provided expertise on OSL sample collection procedures and conducted the OSL sample measurements and analysis in his laboratory at North Dakota State University. Bill Dietrich provided initial encouragement to conduct a study of the strath terraces at the Angelo Coast Range Reserve using cosmogenic isotopes. Dylan Blumentritt provided assistance collecting ^{10}Be samples in the field and processing samples in the laboratory.

Thank you to the many dedicated and talented research scientists and staff members at Saint Anthony Falls Laboratory for their assistance in conducting the physical experiments presented in chapter 2 of this thesis. Thanks in particular go to Chris Ellis and Jim Mullin for developing the data acquisition cart that enabled data collection during the experiments, Mike Plante, Ben Erickson, Dick Christopher and Jim Tucker for assistance with the initial construction phase of the experiments and Kristen Maccaroni for her assistance with experimental setup, monitoring and data collection. Thank you to Noah Finnegan and Leonard Sklar for allowing me to participate in a set of physical experiments conducted at the Richmond Field Station in Berkeley, CA that inspired the set of physical experiments presented in chapter 2.

Dedication

This thesis is dedicated first and foremost to my wife, Jeanne, who initially agreed to come to Minnesota (from Florida) for a two year Master's degree. And now eight years later we find ourselves the parents of three boys who have only known Minnesota as their home. It was always ‘just one more year’ and then we would settle down. Now all we want to do is stay in Minnesota to raise our family in this great place. Life has been a little messy and uncertain over the past eight years, hopefully the next eight will be a little less messy. I love you.

To Adam, Sam and Ben….if my pursuit of this research caused me to miss spending time with you during the first years of your life, it is my hope that this work will enable me to find happiness in what I do, to generously share that sense of happiness with each of you and to guide you in your own search for happiness.

Table of Contents

List of Tables

List of Figures

CHAPTER 1:

CHAPTER 2:

CHAPTER 3:

INTRODUCTION TO THESIS RESEARCH

INTRODUCTION

It is widely believed that river incision into bedrock plays a key role in setting the physical boundary conditions for hillslope and landscape evolution. The relative rates at which a bedrock river incises its bed (vertical incision) versus erodes its banks (lateral erosion) help to determine the boundary conditions felt by the surrounding landscape. The process of vertical bedrock incision has been well studied [Howard and Kerby, 1983; Seidl et al., 1994; Howard, 1994; Whipple et al., 2000] with recent emphasis on identifying and modeling specific incision mechanisms and the role of relative sediment supply in determining incision rates [Sklar and Dietrich, 2004].

Significantly less effort has been devoted to understanding the controls and mechanisms of lateral bedrock erosion. This knowledge gap persists despite abundant field evidence that suggests lateral erosion can be the dominant mode of channel erosion for extended periods of time (i.e. strath terraces) and despite the potentially important role that lateral erosion plays in determining bedrock channel width and maintaining bedrock channel geometry.

Hypotheses regarding the influence of boundary conditions on the process of lateral erosion and planation of a strath surface have been proposed. Changes in boundary conditions such as an increase in sediment supply [Gilbert, 1877; Hancock and Anderson, 2002], increased discharge [Merritts et al., 1994] and tectonic quiescence [Bull, 1991] have all been associated with enhanced lateral erosion and the carving of flat bedrock surfaces. However, quantitative field-based evidence is sorely needed to confirm or reject these hypotheses.

In addition to the role that lateral erosion plays in carving flat bedrock (strath) surfaces, the process of lateral bedrock erosion enables a bedrock channel to adjust its width in response to changes in boundary conditions. Understanding what controls bedrock channel width remains a fundamental problem in geomorphology [Montgomery and Gran, 2001; Finnegan et al., 2005; Finnegan et al., 2007] with wide ranging implications. A better understanding of the mechanisms by which a bedrock channel changes or maintains its width could prove to be valuable for future studies of landscape evolution at the scale of entire mountain ranges and for more local morphodynamic studies of bedrock channel evolution and sediment transport processes.

The body of work herein seeks to improve our understanding of lateral bedrock erosion by identifying specific mechanisms, evaluating the influence of channel characteristics on rates of lateral bedrock erosion and exploring how changes in the boundary conditions of a bedrock river influence the relative rates of vertical incision versus lateral erosion with regard to strath terrace generation. To achieve this goal we have conducted three distinct but complimentary studies using a variety of investigative techniques applied across a range of spatial scales.

First we report results from a field-based study designed to explore the control of sediment supply on the ratio of vertical incision to lateral erosion as it relates to strath terrace formation. At the heart of this field-based study is the measurement of cosmogenic isotope concentrations (^{10}Be) in sediment samples from two different location types: paleo sediment deposits located directly on top of strath surfaces and modern sediment deposits located within the modern channel. From these isotopic measurements we are able to estimate basin-wide denudation rates and infer sediment supply conditions that existed during periods of strath cutting (based on isotope concentrations in paleo strath terrace sediment) versus sediment supply conditions that existed during periods of vertical incision (based on isotope concentrations in modern channel sediment). Results from this study indicate that changes in the sediment supply boundary condition exert a control on the ratio of vertical to lateral erosion rates and therefore on the ability of a bedrock channel to laterally erode a strath surface. Specifically, the results indicate that during periods of elevated sediment supply, lateral erosion is the dominant channel process. This study provides much needed quantitative field data that are used to evaluate existing hypotheses regarding the influence of sediment supply on the process of lateral bedrock erosion.

Previous investigations of lateral bedrock erosion indicate that the first order control of relative sediment supply on bedrock channel incision is the prevention of vertical bedrock incision. Results from a numerical modeling study of strath terrace formation suggest that changes in relative sediment supply do not significantly change the rate at which a bedrock channel erodes its banks but simply inhibits vertical incision of the bed [Hancock and Anderson, 2002]. While the results from our field study provide quantitative data that suggests lateral erosion is dominant during periods of elevated

sediment supply, the data do not give us the ability to determine if rates of lateral erosion are constant in the face of changing sediment supply.

To answer this question and to identify specific mechanisms of lateral erosion, we conducted a set of physical experiments which represent the second distinct study in this dissertation. The physical experiments were designed to identify specific mechanisms of lateral erosion and explore how channel conditions, particularly those that are sensitive to changes in sediment supply, might influence rates of lateral erosion. It is well established that changes in relative sediment supply can drive changes in channel bed roughness [Dietrich et al., 1989]. In the case of channels incising into bedrock, the response of channel bed roughness to changes in relative sediment supply can manifest itself as a coarsening or fining of the existing alluvial cover or as increased exposure or coverage of a rough or smooth bedrock surface. Given the potential for channel bed roughness to change in response to a change in relative sediment supply, we designed the set of experiments to investigate the influence of channel bed roughness on rates of lateral bedrock erosion. Analysis of the experimental data enabled us to identify specific mechanisms of lateral bedrock erosion and to demonstrate that changes in bed roughness, which often accompany changes in relative sediment supply, can lead to significant variation in rates of lateral erosion.

The set of physical experiments allowed us to identify a novel mechanism of lateral bedrock erosion in which saltating bedload particles are deflected by roughness elements on the bed and directed into the channel walls. This deflection event imparts sufficient wall normal momentum to the deflected bedload particle such that it causes wall erosion on impact. The set of physical experiments showed that lateral bedrock erosion via deflected particle impacts is sensitive to changes in channel bed roughness and enabled us to identify several defining characteristics of the mechanism including: 1) erosion due to this mechanism is focused near the base of the channel wall resulting in channel cross sections with undercut banks; 2) a minimum roughness element to bedload particle size ratio must be met in order to generate significant lateral wall erosion due to this deflection mechanism; 3) once the minimum roughness threshold has been crossed such that particle deflections are frequent and effective, rates of lateral erosion gradually reach a stable value such that further increases in the size of roughness elements do not result in higher rates of lateral erosion; 4) there appears to

be a trade-off between increased deflection surface area associated with larger roughness elements and a concomitant increase in form drag associated with the larger elements such that rates of lateral erosion do not scale linearly with shear stress on the bed. In order to confirm that these observed erosion characteristics were produced by the impacts of deflected bedload particles, we developed a numerical model of lateral bedrock erosion that incorporates this specific process as the only source of lateral wall erosion.

Development of this numerical lateral erosion model represents the third component of our investigation into the process of lateral erosion in bedrock rivers. Critical components of the numerical model include: 1) calculation of the downstream bedload particle velocity including a correction for form drag associated with roughness elements on the bed; 2) an estimate of the number of bedload particle deflections per unit time based on roughness element size, protrusion height and the mean free space between roughness elements; 3) tracking the wall-normal velocity of deflected bedload particles from the moment of deflection to the moment of wall impact by solving an ordinary differential force balance equation between particle momentum and fluid drag forces; 4) tracking the bed-normal particle velocity and vertical position of deflected bedload particle by solving a force balance equation between bed-normal particle momentum and the forces of fluid drag and gravity acting on the particle; 5) implementation of an empirical relationship between wall-normal particle velocity and the amount of bedrock material removed per impact that allows the model to estimate rates of lateral bedrock erosion for a given set of bedload supply and bedload transport conditions.

We run the model using the same boundary conditions established in the set of physical experiments to see if we can replicate the key characteristics of lateral bedrock erosion via bedload particle impacts. As was the case in the set of physical experiments, the primary variable in the set of numerical experiments was channel bed roughness. Using the same sediment supply, bed roughness and flow conditions used in the set of physical experiments, our model is able to reproduce the magnitude of channel wall erosion measured during the physical experiments within a reasonable margin of error. The model is able to reproduce the minimum roughness threshold required for significant lateral erosion that was observed in the physical experiments by implementing a ‘deflection rule’ based on the size ratio between bedload particle and bed roughness

element. In addition the model is able to reproduce the observed erosion rate stabilization that we believe is driven by a trade-off between an increase in the number of particle deflections and an increase in form drag as the size of the roughness element increases. Finally, the model does a fair job of reproducing the undercut morphology that was observed in the physical experiments. The model underestimates the maximum height of erosion above the bed by a factor of 2 and therefore the lateral erosion is concentrated at the base of the channel wall resulting in an overestimation of the maximum lateral depth of the undercut.

The three distinct studies described above complement each other to form a cohesive body of work that seeks to improve our understanding of the process of lateral bedrock erosion. More specifically, this body of work seeks to understand how changes in relative sediment supply and the concomitant changes in channel bed roughness influence the mechanisms and rates of lateral bedrock erosion. The field-based study uses a watershed scale approach to provide much needed quantitative data that are used to determine the influence of sediment supply on the relative rates of vertical and lateral erosion, and ultimately on strath terrace generation. The field-based study confirms a long standing hypothesis that an increase in relative sediment supply encourages lateral planation of strath surfaces [Gilbert, 1877; Hancock and Anderson, 2002]. However, this field scale approach is not sufficient to address another long standing hypothesis which states that an increase in relative sediment supply is effective at preventing vertical incision of the bed but does little to change rates of lateral bedrock erosion [Hancock and Anderson, 2002]. This hypothesis exists in part due to a lack of understanding regarding the specific mechanisms of lateral bedrock erosion. The physical experiment described above compliments the field-based study first by identifying a specific mechanism of lateral erosion and second by determining how that mechanism is influenced by the feedback between sediment supply and channel bed roughness. While the field-based study confirms a long standing hypothesis about the link between sediment supply and lateral erosion of a strath surface, the set of physical experiments enables us to show that changes in sediment supply not only affect rates of vertical incision but can increase or decrease rates of lateral bedrock erosion depending on how channel bed roughness responds to a change in sediment supply. The numerical

model serves to confirm our findings from the physical experiment and enables us to further explore the link between channel bed roughness and rates of lateral erosion.

CHAPTER 1

Field evidence for climate-driven changes in sediment supply leading to strath terrace formation

Geology, May 2009; v. 37; no. 5; p. 467-470; doi: 10.1130/G25487A.1

1.1. INTRODUCTION

Despite the widespread use of strath terraces in fluvial and tectonic geomorphology, the conditions surrounding planation of a strath surface are not well understood. The most frequently invoked hypothesis for strath planation suggests that climate-driven increases in sediment supply relative to transport capacity drives aggradation and armors the bed of the channel [Gilbert, 1877]. Under these conditions, vertical incision is limited and lateral planation becomes the dominant mode of incision.

Among the numerous studies that invoke climate-driven increases in sediment supply as a driver of strath planation [e.g., Hancock and Anderson, 2002; Wegmann and Pazzaglia, 2002; Personius et al., 1993], there has yet to be a study that quantifies sediment supply conditions associated with strath planation. Here we show that sediments capping a broad, late Pleistocene strath terrace in northern California record high sediment supply rates relative to post-abandonment rates, providing quantitative support for the Gilbert hypothesis of strath terrace formation.

1.2. FIELD AREA

The South Fork of the Eel River and its headwater tributaries occupy forested valleys in the Coastal Range of northern California. Regional rock uplift rates are highly variable ranging from 4 mm y^{-1} near the Mendocino triple junction to 0.4 mm y^{-1} along the coast near the headwaters of the South Fork Eel [Merritts et al., 1994]. The bedrock is part of the Central and Coastal belts of the Franciscan Complex and consists predominately of mudstone, with localized outcrops of sandstone [Jayco et al., 1989]. Seidl and Dietrich [1992] mapped a series of strath terraces along Elder Creek and the South Fork Eel (Figure 1.1) located within the Nature Conservancy's Angelo Coast Range Reserve. It is these terraces that we investigate here.

1.3. METHODS

The concentration of ^{10}Be in terrace sediment has been shown to be a reliable estimator of long-term, basin-averaged erosion rates during the period of deposition [Schaller et al., 2002]. In this study, we use the concentration of ^{10}Be in strath terrace sediment to determine basin-averaged erosion rates during deposition (and presumably during planation of the strath surface). Strath terrace sediment samples were collected

underneath large alluvial boulders (~40–60 cm in diameter) as close as possible to the strath-alluvium contact to increase the likelihood that the sediment is in place and was deposited during strath planation (Figure 1.2). We discarded the outer 10–20 cm of bulk sediment to minimize the effect of post-depositional production due to lateral exposure. In addition to strath terrace samples, we have measured the ^{10}Be concentration in active fluvial deposits adjacent to each terrace sample location. In both cases, the 0.25 – 0.50 mm grain size fraction was processed using standard ^{10}Be extraction techniques [Kohl and Nishiizumi, 1992].

^{10}Be production rates (SLHL of 4.5 atm g^{-1} y^{-1}) and topographic shielding factors (Appendix 1.1) were calculated from LiDAR elevation data (www.ncalm.org) using the methods of Balco et al. [2008] and the production equations of Lal [1991] as modified by Stone [2000]. Paleoerosion rates, as well as modern erosion rates, were calculated using the equations of Schaller et al. [2004] which allow for the estimation of post-depositional production beneath a terrace deposit that decreases in depth through time.

OSL samples were collected adjacent to the ^{10}Be samples in closed-end metal cylinders with diameters ranging from 7.5 to 12.5 cm. Processing, data collection, and data analysis of the OSL samples (Appendix 1.2 and Appendix 1.3) followed the methods described in Lepper et al. [2007; including GSA data repository item 2007164].

1.4. DATA INTERPRETATION

In calculating the paleoerosion rates reported here, we have made some simplifying assumptions that allow us to constrain post-depositional production of ^{10}Be. First, we assume that the thickness of the terrace deposit was at a maximum immediately after planation of the strath surface. If the terrace deposit accumulated over 10^2 to10^3 years and reached a maximum thickness well after planation, our assumption of rapid burial would result in an underestimation of post-depositional production. Second, we assume that post-depositional production due to lateral exposure of the sample on the valley wall is negligible. Topographic shielding calculations indicate that production due to lateral exposure is only ~50% of the in situ production rate at the terrace surface. In addition, the duration of lateral exposure will be less than the OSL age used in the calculation of post-depositional production depending on the erosion and retreat rate of the incised terrace face. Assuming negligible production from lateral exposure also results in a

potential underestimation of post-depositional production. These two assumptions, along with a correction for post-depositional lowering of the terrace surface (0.07 mm/yr^{-1} based on the lowest erosion rate in our data set), allow us to reasonably estimate post-depositional production in the paleoerosion rate samples. Because both of our assumptions result in a potential underestimation of post-depositional production, the paleoerosion rates should be viewed as minimum rates of erosion.

The OSL ages derived from strath terrace sediment represent the depositional age of the OSL and ^{10}Be sediment samples. Given that the OSL samples were collected underneath large alluvial boulders as close as possible to the strath surface, it is likely that the sediment used for OSL dating is associated with strath planation. We also note that ages derived from material in contact with a strath surface are commonly assumed to be associated with the period of planation that carved the strath surface [Wegmann and Pazzaglia, 2002; Hancock and Anderson, 2002]. Therefore, we interpret the OSL ages in our study as a point in time when active planation was taking place.

1.5. RESULTS

^{10}Be concentrations in strath terrace sediment decrease with strath height such that concentrations from the upper strath are only two-thirds of those found in modern river and Holocene terrace sediment, and one-third of those found in sediment from a Pleistocene-Holocene (P-H) transitional terrace (Table 1.1). OSL ages derived from strath terrace sediment track well with strath height indicating that the upper strath surface is late Pleistocene in age while lower strath surfaces range in age from the P-H transition to the middle Holocene (Figures 1.3 and 1.4). After a correction for post-depositional production, paleoerosion rates from the upper strath terrace are a factor of two greater than nearby modern erosion rates and 3.5 times greater than paleoerosion rates from the P-H transition (Figure 1.5). We have no age control on terrace samples near the mouth of Elder Creek and Jack of Hearts Creek (samples 002 and 009 respectively), and therefore just report the ^{10}Be concentration and uncorrected paleoerosion rate for those samples.

Using LiDAR data of the region, we have identified “flat” regions (average slope ≤ 5%) near the channel with areas greater than 100 m^2. The cumulative distribution of flat area (m^2) as a function of height shows a significant increase in cumulative area

between 13 m and 16 m above the channel (Figure 1.1 (inset)). Based on this vertical distribution, we have categorized the flat regions into two broad categories: *lower* (< 13 m above channel) and *upper* (≥ 13 m above channel). This analysis crudely delineates terraces surfaces and demonstrates the broad extent of the *upper* terrace relative to the *lower* terraces. Field inspection of many of the flat regions identified with this method confirms that they are in fact strath terraces.

The use of ^{10}Be concentrations in strath terrace sediment to estimate sediment supply during strath planation requires that the averaging time scale of the sample is less than the duration of lateral planation. With averaging time scales of ~2.5 ky and preserved terrace widths approaching 100 m (Table 1.1), late Pleistocene planation rates would have to be at least 40 mm yr^{-1} before the averaging time scale would exceed the duration of lateral planation. Based on the difference in age between OSL samples collected at opposite ends of a gently sloping P-H transitional terrace (Figure 1.4, samples collected ~34 m apart), we estimate an average lateral planation rate of 13 mm yr^{-1}during this period. Planation rates would have to increase by a factor of three before the duration of lateral planation equaled the averaging time scale mentioned above. An increase of this magnitude seems unlikely and we believe the ^{10}Be samples from late Pleistocene terraces represent sediment supply conditions that are distinct to the period of lateral planation.

1.6. DISCUSSION

The widest and most extensive strath terraces are mantled with alluvial sediment which was deposited when the landscape was eroding twice as fast as modern erosion rates. This result supports the hypothesis that extensive strath planation occurs under conditions of elevated sediment supply and quantifies for the first time sediment supply conditions during a period of strath planation relative to conditions during a period of vertical incision and sporadic terrace formation.

Sediment supply on the South Fork Eel appears to be controlled by climate and hillslope response to channel incision. Regional paleoclimate reconstructions based on pollen records from Clear Lake, CA (~100 km southeast) indicate that annual precipitation was higher than present for an extended period of time during the late Pleistocene [~70 ky to 18 ky; Adam and West, 1983]. This period of increased

precipitation correlates in time with OSL ages from the upper strath terrace (33.3 ± 4.1 ky and 20.5 ± 3.3 ky) where we have found elevated sediment supply. In addition to a general increase in sediment supply during this wet period, sediment supply conditions were almost certainly influenced by an increase in deep-seated landslide activity. Several studies support this assertion including a study by Hilley et al. [2004] that shows a strong link between precipitation and movement of deep-seated landslides. A study in the nearby Coast Range of Oregon suggests landslide activity increased during the latest Pleistocene and argues that it played an important role in regional strath terrace development [Personious et al., 1993]. In addition to the suggested climate-driven increase in deep-seated landslide activity, Mackey et al. [2006] hypothesize that lateral channel erosion along the South Fork Eel, possibly driven by intense weathering of the mudstone banks due to wetting-and-drying cycles [Stock et al., 2005], provides an important baselevel control on deep-seated landslide activity. This hypothesis provides a potential feedback mechanism between lateral planation and increased sediment supply that likely contributed to extensive strath planation during the late Pleistocene.

Increased deep-seated landslide activity during the late Pleistocene provides an obvious mechanism to increase sediment supply relative to transport capacity, resulting in a channel bed that is armored with sediment and resistant to vertical incision. Our data suggest a link between elevated sediment supply, extensive strath planation and increased precipitation during the late Pleistocene. Given this link, and the susceptibility of the South Fork Eel watershed to deep-seated landslides, we appeal to a climate-driven increase in sediment supply and deep-seated landslide activity, augmented by lateral channel erosion and baselevel-driven landslides, as the primary driver of strath planation during the late Pleistocene.

In general, our data show a positive relationship between terrace area and sediment supply. However, there are two lower terraces, both located at tributary junctions, which do not show this relationship. Sediment from the large terrace at the mouth of Jack of Hearts Creek indicates moderate sediment supply (0.20 mm y^{-1}) while sediment from the small terrace at the mouth of Elder Creek indicates elevated sediment supply (0.28 mm y^{-1}). The unexpectedly high erosion rate from the small Elder Creek terrace could be the result of deep-seated landslide activity within a small drainage basin (~17 km^2), where

localized delivery of ^{10}Be-poor sediment can increase the measured erosion rate above the true basin-averaged erosion rate [Niemi et al., 2005].

Returning to the two OSL samples from the gently sloping P-H transitional terrace, we estimate a vertical bedrock incision rate of 0.6 mm y^{-1}. This estimate is more than an order of magnitude less than our estimate of lateral planation rates (13 mm y^{-1}) from the same continuous surface. In comparison, direct measurements of vertical incision along the South Fork Eel revealed median rates between 0.6 and 0.75 mm y^{-1} [Stock et al., 2005]. In another study of incision on the South Fork Eel, Sklar and Dietrich [2006] used a bedrock incision model that accounts for the effects of sediment cover to show that vertical incision rates of 0.9 mm yr^{-1} are sustainable under current conditions (~85% of the channel bed covered with sediment). Over longer time scales and multiple terrace cycles, we estimate channel lowering rates between 0.4 and 0.5 mm y^{-1} over the last ~20 ky.

A simple comparison of channel lowering rates and basin-averaged erosion rates suggests that topographic relief has been increasing since abandonment of the upper strath surface and a change to drier climate conditions. Based on the OSL ages from the upper strath and the P-H transitional strath, we estimate channel lowering rates of 0.4 mm yr^{-1} from 20 ky to 12 ky ago. Paleoerosion rates averaged over roughly the same time period are 0.1 mm yr^{-1}, suggesting an increase in relief of 0.3 mm yr^{-1}during this period. Over the last ~12 ky, we estimate channel lowering rates of 0.5 mm yr^{-1} compared to basin-averaged erosion rates of 0.2 mm yr^{-1}, again suggesting an increase in relief of 0.3 mm yr^{-1}during this period. These results support the hypothesis of Gabet et al. [2004] which suggests that a change in climate from wet-to-dry can drive an increase in relief by reducing pore pressure, thus enabling the threshold hillslope angle to increase.

1.7. CONCLUSIONS

The elevated paleoerosion rates associated with the extensive upper strath terrace support the hypothesis that strath planation occurs under elevated sediment supply conditions. In addition, these elevated paleoerosion rates correlate in time with increased annual precipitation during the late Pleistocene. The susceptibility of the South Fork Eel watershed to deep-seated landslides provides an obvious mechanism for

increasing sediment supply relative to transport capacity and preventing vertical incision. Thus, our data suggest that a climate-driven increase in sediment supply and deep-seated landslide activity, augmented by the positive feedback between lateral planation and baselevel induced landslide activity, is the primary driver of strath planation in the upper South Fork Eel basin. Our data indicate an increase in topographic relief over the last ~20 ky. This increase in relief could be the result of a climate-driven increase in the threshold hillslope angle.

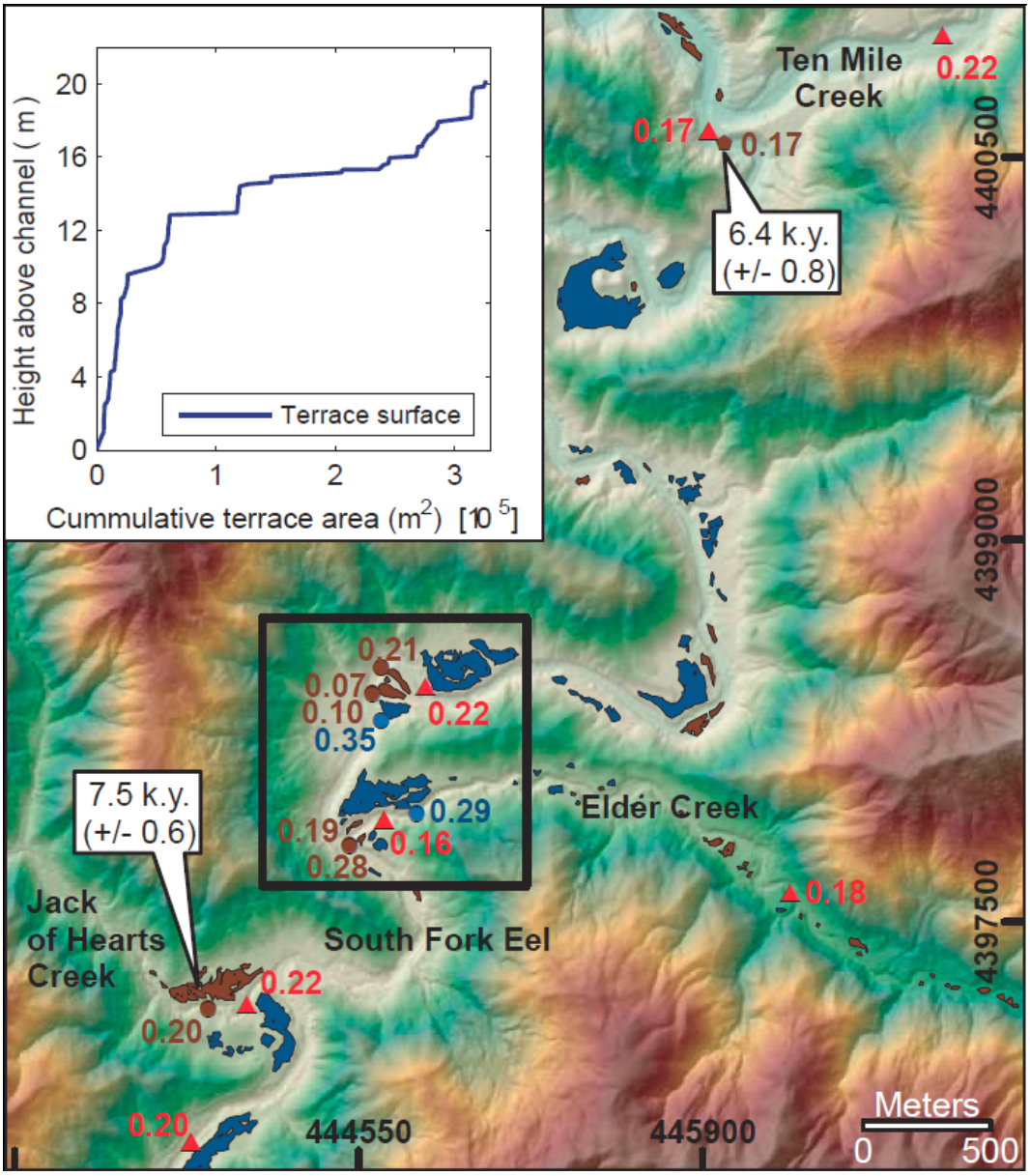

Figure 1.1 - Sample locations and associated basin-averaged erosion rates (mm y^-1): modern stream sediment (red triangles); upper strath terrace sediment (blue circles); and lower strath terrace sediment (brown circles). Delineated areas crudely identify terrace surfaces (slope < 0.05) and are categorized according to height above the channel: lower terraces 0.0 - 12.9 m (brown); upper terrace ≥ 13.0 m (blue). Terrace deposit age shown in callout box. Inset: vertical distribution of terrace area. (UTM-10).

Figure 1.2 - Strath-alluvium contact exposed along the SF Eel at the flight of terraces where samples 013, 014, 015 and 016 were collected. Note the large alluvial boulders in contact with the strath surface. Paleoerosion samples were collected underneath these large alluvial boulders to increase the likelihood that the sediment is in place and representative of the lateral planation phase.

Table 1.1 - Cosmogenic Isotope Data, OSL Results and Terrace Width

Sample ID & Type	Location	$^{10}Be_{total}$ [1] (10^3 atoms g^{-1})	Depth (m)	$^{10}Be_{dep}$ [2] (10^3 atoms g^{-1})	OSL Age (ky)	$^{10}Be_{in}$ [3] (10^3 atoms g^{-1})	Erosion Rate [4,5] (mm y^{-1})	1σ Error [6] (mm y^{-1})	Denudation Time Scale (y)	Terrace Width (m)
Modern										
001	Ten Mile	29.7	-	-	-	29.7	0.22	0.019	4,052	-
003	Elder	40.7	-	-	-	40.7	0.18	0.021	4,691	-
004	Elder	43.8	-	-	-	43.8	0.16	0.017	5,292	-
010	SF Eel	32.0	-	-	-	32.0	0.20	0.017	4,350	-
011	SF Eel	29.5	-	-	-	29.5	0.22	0.023	3,972	-
012	SF Eel	38.8	-	-	-	38.8	0.17	0.022	5,222	-
JOH-21	JOH	28.3	-	-	-	28.3	0.22	0.071	4,090	-
Lower & Middle Strath										
002	Elder	37.1	1.5	-	-	37.1	0.19	0.060	4,459	26
009	Elder	25.8	2.7	-	-	25.8	0.28	0.025	3,133	5
014	SF Eel	65.5	4.2	1.47	11.8 ± 1.1	64.4	0.10	0.005	8,675	41
015	SF Eel	89.0	3.7	1.38	9.2 ± 0.8	88.1	0.07	0.004	11,857	30
016	SF Eel	31.9	3.2	1.62	8.3 ± 0.8	30.4	0.21	0.016	4,089	24
019	SF Eel	40.8	2.0	3.16	6.4 ± 0.8	37.8	0.17	0.024	5,090	5
JOH-06	JOH	31.3	3.5	1.27	7.5 ± 0.6	30.1	0.20	0.028	4,350	110
Upper Strath										
006	Elder	29.7	3.0	5.2	33.3 ± 4.1	24.9	0.29	0.020	2,992	134
013	SF Eel	20.2	6.4	1.65	20.5 ± 3.3	18.7	0.35	0.023	2,522	60

[1]Total ^{10}Be concentration after a correction for analytical blank.

[2]Concentration of ^{10}Be due to post-depositional production. Density of overlying terrace deposit is assumed to be 2.0 g cm^{-3}

[3]Concentration of ^{10}Be due to inheritence.

[4]Calculated using equations in Schaller et al., 2004.

[5]SLHL production rate of 4.5 atoms g^{-1} y^{-1} (Nishiizumi, 2007) and production equations of Lal (1991) as modified by Stone (2000)

[6]Represents one standard deviation due to uncertainty associated with measurement of sample and blank.

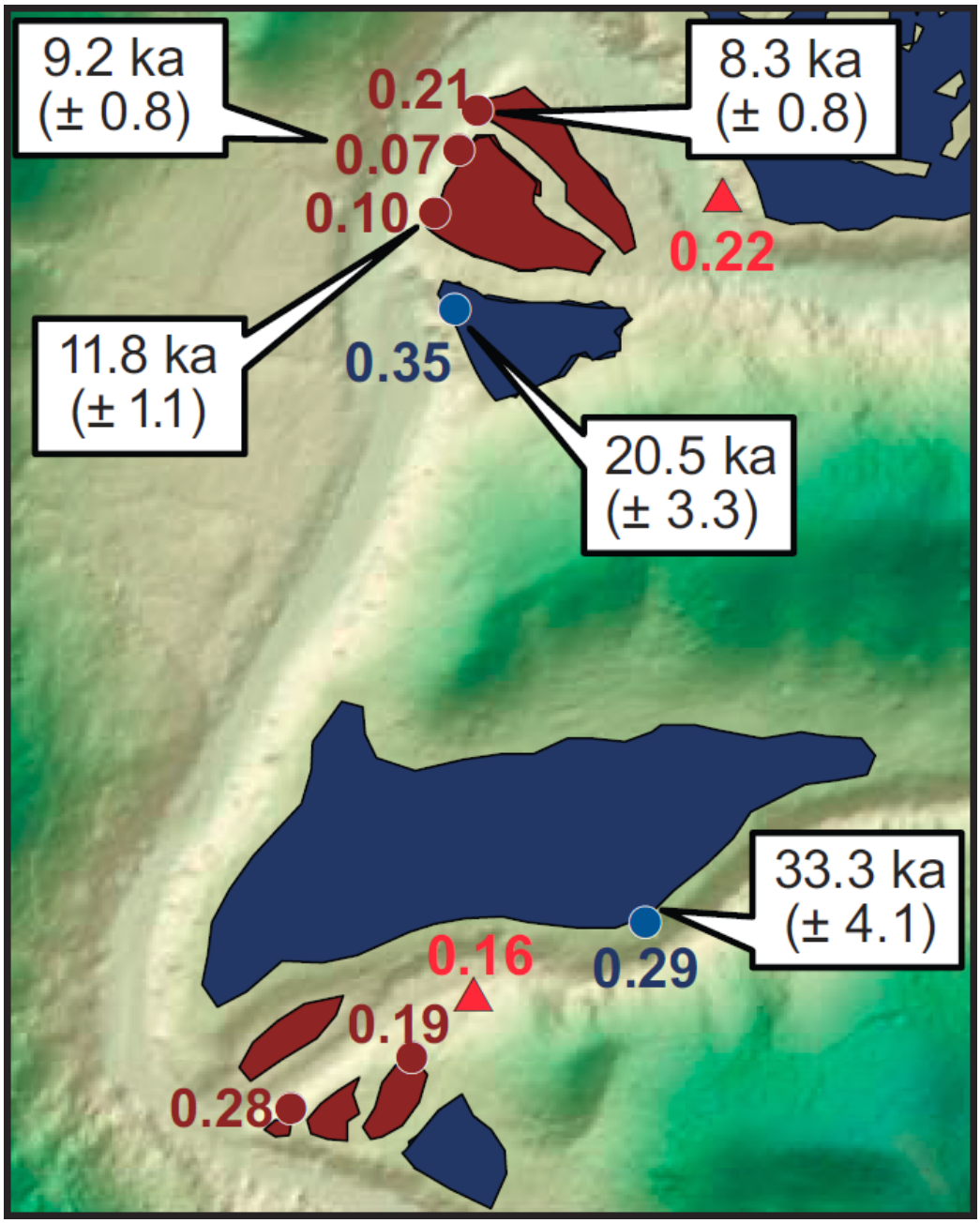

Figure 1.3 - Close-up of boxed region in Figure 1.1. Colors, symbols and erosion rates are as described in Figure 1.1. OSL-derived ages of strath terrace deposits are shown in callout boxes. Lines A-A′, A-B′ and C-C′ represent the locations of valley cross sections shown in Figure 1.4.

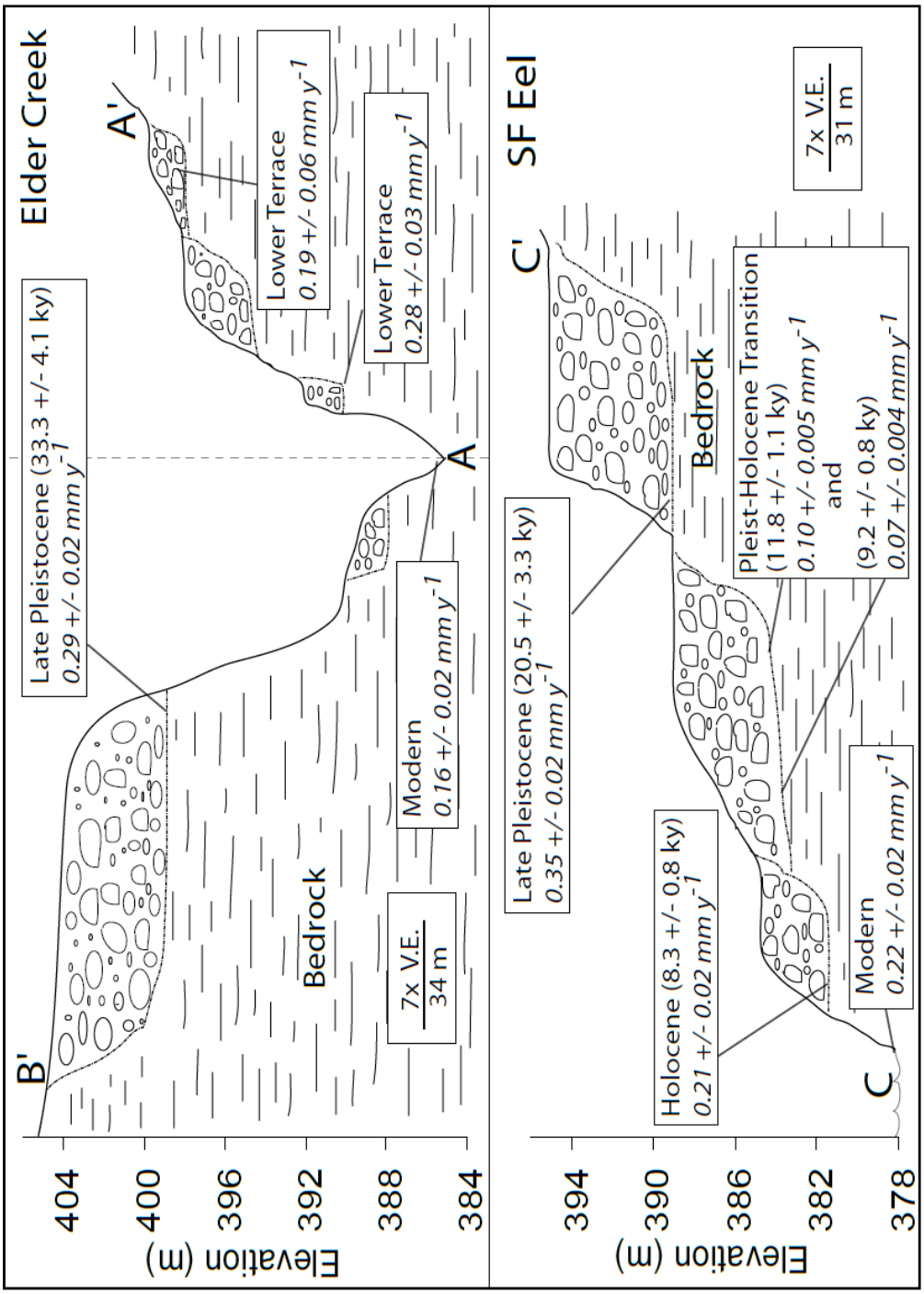

Figure 1.4 - Inferred valley cross sections at sample locations along Elder Creek and the South Fork Eel. Locations of the cross sections are shown as lines A-A', A-B' and C-C' in Figure 1.3. The cross-valley width of the strath surfaces (as drawn with dashed lines) are approximate due to a lack of exposure along the entire valley width.

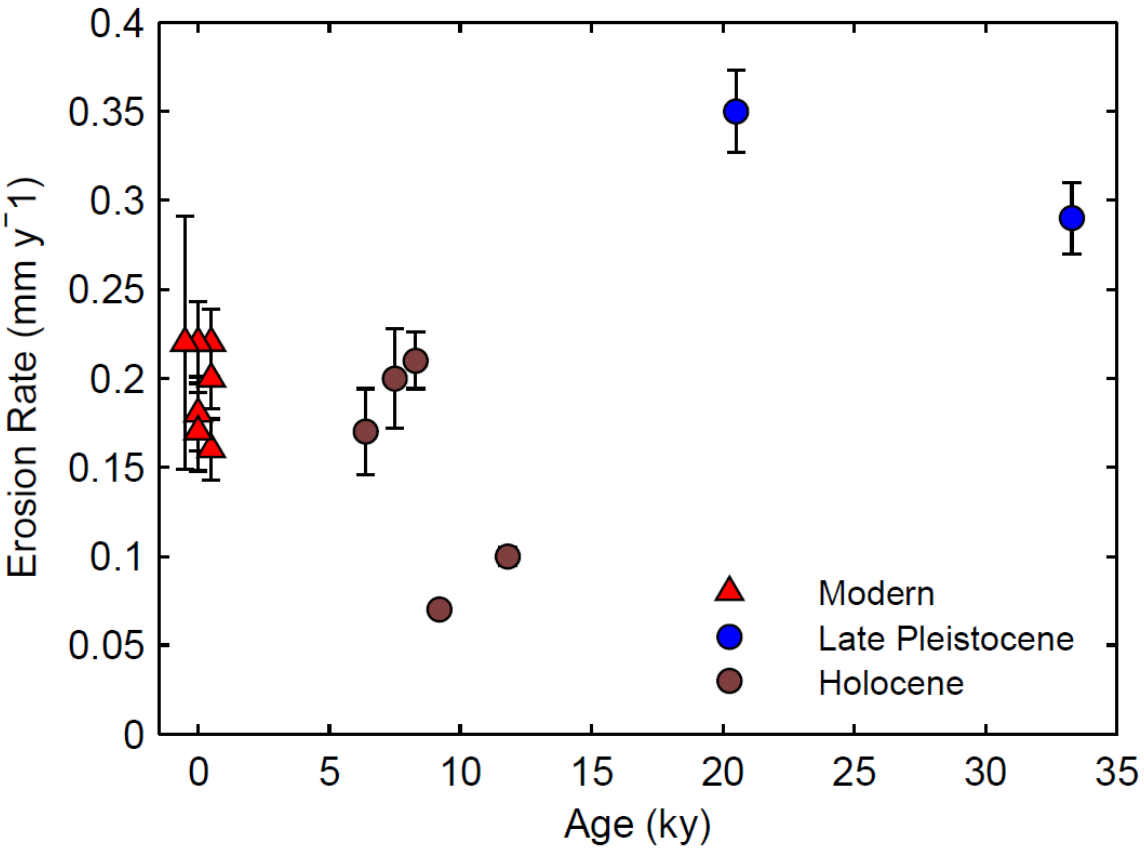

Figure 1.5 - ^{10}Be derived erosion and paleoerosion rates versus OSL age. The two undated terrace samples at the mouth of Elder Creek (samples 002 and 009) are not shown. Error bars show 1σ uncertainty due to AMS measurement error and a correction for the chemical blank. Errors for the two Pleistocene-Holocene transition samples are less than the height of the symbol.

CHAPTER 2

Lateral erosion in an experimental bedrock channel: erosion mechanisms and the influence of bed roughness on rates of erosion.

2.1. INTRODUCTION

It is widely believed that bedrock incision plays a key role in setting the physical boundary conditions for landscape evolution. To date, the majority of bedrock incision studies have focused on the processes and implications of vertical bedrock incision or incision that lowers the channel bed [Howard, 1994; Whipple et al., 2000; Sklar and Dietrich, 2001; Sklar and Dietrich, 2004]. The focus on vertical incision is understandable as it is often the primary response of a bedrock channel system to rock uplift. However, an understanding of vertical incision alone is insufficient to address important knowledge gaps including how bedrock channels respond to a range of changes in boundary conditions (climatic and tectonic), what determines the width of a bedrock channel, and which processes lead to changes in width. To make progress on these questions, we need to improve our understanding of how and why bedrock channels erode their banks.

Evidence of lateral bedrock erosion is plentiful. Strath terraces are perhaps the best example of what happens when lateral erosion significantly outpaces vertical incision for an extended period of time. In this scenario, mechanisms of lateral erosion are able to erode the channel banks and valley walls while mechanisms of vertical incision are limited in their ability to incise the bed of the channel. Over an extended period of time, the channel will cut laterally at a constant elevation, producing a flat bedrock (strath) surface as it migrates laterally. When conditions change such that mechanisms of vertical incision outpace mechanisms of lateral erosion, the river cuts down through these strath surfaces, leaving them abandoned above the channel as preserved evidence of a time in which conditions favored mechanisms of lateral erosion. Evidence of lateral erosion can be seen on smaller scales as well, in the form of undercut banks and longitudinal grooves carved into the walls of slot canyons (Figure 2.1). Some of the earliest field work on bedrock erosion established a hypothesis for lateral erosion that remains viable to this day [Gilbert, 1877]. In his study of the Henry Mountains in Utah, Gilbert posited that a bedrock channel will incise laterally when sediment transport conditions are such that the channel bed is armored with sediment. Gilbert reasoned that an armored bed would prevent vertical incision and provide an opportunity for channel erosion processes, such as bedload particle impacts, to be focused on the walls of the channel. Central to Gilbert's hypothesis is the balance between sediment supply and

transport capacity (relative sediment supply) in determining when and why significant lateral erosion occurs.

Two field-based investigations of strath terrace formation have identified changes in relative sediment supply as the likely cause of bedrock channels alternating between dominantly vertical and dominantly lateral modes of erosion [Reneau, 2000; Wegmann and Pazzaglia, 2002]. Field observations and the correlation of geochemically-derived ages of strath alluvium with paleo climate records have led many researchers to conclude that a climate-driven increase in relative sediment supply is a key driver of lateral bedrock erosion [Personius et al., 1993; Wegmann and Pazzaglia, 2009; DeVecchio et al., 2012]. Measurements of ^{10}Be concentration in strath alluvium showed that denudation rates during a period of widespread lateral erosion were two times greater than denudation rates during a period of vertical incision [Fuller et al., 2009]. This result suggests that increased sediment supply was a primary driver of lateral erosion. Numerical models of strath terrace formation have also found that increased relative sediment supply causes a bedrock channel to cut laterally [Hancock and Anderson, 2002]. These investigations of strath terrace formation provide substantial evidence that an increase in relative sediment supply can be a key factor in causing bedrock channels to incise laterally.

Increased stream power in channels cutting into weathered or weak bedrock has also been identified as a key factor driving lateral bedrock erosion [Merritts et al., 1994; Suzuki, 1982]. Stock et al. [2005] provide field evidence that high flow events, in a channel where the wall rock has been preferentially weathered by seasonal wet-dry cycles, can produce lateral erosion rates that outpace vertical incision rates. In this scenario, variable discharge promotes hydration fracturing of the channel walls and enables detachment of rock fragments during high flows. Similarly, an increase in discharge and rainfall intensity associated with typhoon events has been identified as a primary driver of lateral strath erosion in regions of weak bedrock [Stark et al., 2010]. In addition to these field-based studies, a recent numerical model successfully employed changes in fluid shear stress and meander migration as the driver of lateral erosion and autogenic strath terrace formation in highly weathered bedrock [Finnegan and Dietrich, 2011].

Despite evidence that points to increased sediment supply or high flows as likely drivers of lateral bedrock erosion, identifying the specific mechanism of lateral erosion associated with these drivers remains difficult. Increased fluid shear stress acting on the channel walls has been proposed as the effective mechanism associated with high flows in weak bedrock [Stark et al., 2010]. A specific mechanism of lateral erosion tied to an increase in relative sediment supply has not been firmly established. Numerical models of bedrock erosion that ignore the influence of sediment cover, including models that predict bedrock channel geometry [Stark, 2006; Wobus et al., 2006] and models that simulate strath terrace formation [Finnegan and Dietrich, 2011], effectively assume that fluid shear stress is the dominant mechanism of lateral erosion. Even numerical models that do consider the influence of sediment cover on the process of bedrock erosion assume that lateral erosion scales with fluid shear stress [Hancock and Anderson, 2002; Turowski et al., 2007]. One conclusion to emerge from these numerical investigations of bedrock erosion is that neither sediment cover nor increased sediment supply change the rate of lateral bedrock erosion. These results suggest the only link between an increase in relative sediment supply and lateral erosion of strath surfaces is the prevention of vertical incision.

In an attempt to identify drivers and mechanisms of bedrock incision, several physical experiments have been conducted. The experiments fall into two categories, those that use a brittle analog material to simulate the breakdown of natural bedrock and those that use a cohesive clay-rich analog material. Using a brittle bedrock analog, Carter and Anderson [2006] conducted an experiment meant to simulate lateral wall erosion in slot canyons. They found the most likely mechanism of lateral erosion to be fluid stress associated with back-eddy rotation in the lee of channel wall undulations. Also using a brittle bedrock analog, Finnegan et al. [2007] demonstrated the influence of sediment supply on setting the width of channel incision and documented lateral erosion in the form of channel widening via bedload abrasion. Physical experiments of channel incision using cohesive clay-rich substrates [Shepherd and Schumm, 1974; Wohl and Ikeda, 1997] have focused primarily on incision of the channel bed. These experiments seem to reproduce erosional bedforms via bedload abrasion despite the use of a substrate that deforms plastically. We note that most of the physical experiments designed to investigate bedrock channel incision have tried to isolate the mechanism of

bedload abrasion by using an analog material that is unable to be eroded by fluid shear stress alone under experimental conditions.

The study described in this paper seeks to improve our understanding of the process of lateral bedrock erosion by conducting controlled physical experiments using a bedrock analog material that replicates brittle deformation observed in the field as well as in the laboratory [Sklar and Dietrich, 2001]. In this study, we investigate the potential role that increased relative sediment supply and sediment cover might play in determining rates of lateral erosion and influencing the actual mechanism of lateral erosion. We have two primary goals for this experimental investigation. First, we seek to identify specific mechanisms of lateral erosion given conditions of complete sediment cover of the bed. Second, we hope to determine if rates of lateral erosion change in response to variations in sediment supply and sediment cover or if rates of lateral erosion remain constant through changes in relative sediment supply as has been suggested [Hancock and Anderson, 2002].

A natural avenue of inquiry for the current study is to examine how increased relative sediment supply and sediment cover might influence the transport of bedload particles and their interaction with channel boundaries. We start with a simple premise that transitioning from an exposed channel bed to one that is covered with sediment is likely to change channel bed roughness. Development of an armor layer has the potential to change the nature of roughness elements on the bed from elements with primarily negative relief (i.e. erosional bed forms such as longitudinal grooves, potholes and incised thalwegs), to elements with positive relief (i.e. cobbles and boulders protruding up into the flow). We focus particularly on exploring how the change in channel bed roughness associated with the development of channel bed armor affects bedload transport and the interaction of particles with the channel walls.

To achieve our goals, we have conducted a set of flume experiments in which the primary variable is channel bed roughness. We construct experimental bedrock channels using a sand- cement mixture in order to replicate erosion of a brittle material. We artificially inhibit vertical incision of the bed by using a resistant bedrock mixture on the bed. In order to vary channel bed roughness, we embed sediment particles of different diameter into the resistant mixture that makes up the channel bed. These embedded roughness elements are thus fixed throughout the experiment. Erodible

channel walls are constructed on top of the resistant channel bed using a weaker mixture of sand and cement. The strength of the channel walls is engineered such that no erosion occurs under conditions of clear-water flow. Lateral wall erosion is measured by differencing topographic scans of the channel from one run to the next. Comparison of lateral erosion rates between sections of different channel bed roughness is accomplished by integrating measured erosion along the vertical profile of the channel wall so that we arrive at a cross-sectional erosion rate that represents the area of material removed from the channel cross section.

These experiments show that rates of lateral erosion are sensitive to changes in bed roughness with a substantial increase in lateral erosion rates associated with the addition of roughness elements to an otherwise smooth bed. We identify bedload particle deflection by roughness elements on the bed as a primary driver of lateral bedrock erosion via bedload particle impacts. Our results suggest that a minimum bed roughness must be attained before rates of lateral erosion increase significantly. Once this minimum roughness threshold is crossed, further increases in the size of bed roughness elements do not continue to increase rates of lateral erosion despite a concomitant increase in total shear stress on the bed. This decoupling of lateral erosion rates from total shear stress on the bed reflects a trade-off between increased form drag associated with larger roughness elements (reduces bedload particle velocity) and an increase in the deflection surface area encountered by bedload particles in transport (increases the number of deflected particles and wall impacts).

2.2. METHODS

2.2.1. Fixed Experimental Conditions

All experiments were conducted at Saint Anthony Falls Laboratory, University of Minnesota. We conducted the experiments in a tilting-bed flume equipped with a laser probe to measure channel elevation and an ultrasonic probe to measure water surface elevation. Channel forms were installed within the tilting flume to construct the experimental bedrock channels used in the experiments. All experimental channels were straight in planform, rectangular in cross section and comprised of a non-erodible bed and erodible channel walls (Figure 2.2). Experimental channels were either 6 or 8 m in length with an additional 1.0 to 1.5 m section at the head of the channel to allow channel

flow and bedload transport conditions to reach a uniform steady state prior to entering the experimental sections of the channel. Each channel was composed of three (in the case of a 6 m channel) or four (in the case of a 8 m channel) distinct channel reaches or 'roughness sections' (Figure 2.3). Each distinct roughness section was 2 m in length with a uniform but unique particle size embedded in the non-erodible bed mixture to create channel sections with distinct bed roughness characteristics.

Throughout the set of experiments the following variables were held constant: water discharge, channel bed slope, bedload grain size and sediment supply per unit width. Discharge was set at 12.8 L s^{-1}, resulting in flow depths of roughly 50 to 75 mm depending on bed roughness (Table 2.1). The average bed slope for all experiments was set at 0.025 by tilting the confining flume. The bedload sediment used during periods of constant bedload supply had a narrow size distribution with a median grain size of 4.7 mm. Bedload supply rates were roughly 41 g s^{-1}. This supply rate resulted in a sediment supply per unit width of approximately 100 mm^2 s^{-1}.

During periods of bedload supply, an auger style sediment feeder delivered bedload to the channel at a constant rate from a single location roughly 1.0 to 1.5 m upstream of the first measurement section (Figure 2.3). A sediment diffusion device was attached to the sediment feeder to achieve a more uniform distribution of bedload across the width of the channel. Under the imposed experimental conditions, the transport stage (τ^*/τ^*_c) was much greater than unity resulting in vigorous bedload transport with negligible deposition of bedload particles (Table 2.1). Under these conditions, eroded bedrock material was rapidly transported downstream without being deposited within the experimental channel.

At the downstream end of the experimental channel, water and sediment flowed into a standing pool of water (Figure 2.3). The surface elevation of the standing water was set to match the water surface of the channelized flow at the downstream end of the channel. The surface elevation of the standing water was set at the beginning of each experiment by an adjustable gate at the downstream end of the tilting flume and was held constant for the duration of that experiment. Super critical flow in the experiment channels minimized backwater effects in the downstream section of the channel. Because the channel bed did not erode under the experimental conditions, the mean downstream slope remained constant for the duration of each experiment.

2.2.2. Variable Bed Roughness

The primary independent variable in this set of experiments is channel bed roughness. Bed roughness was varied along the length of the channel by creating distinct 'roughness sections' in which a sediment particle of given size was embedded in the sand-cement mixture used to construct the bed of the channel. To vary channel bed roughness along the length of the channel, the size of the embedded particle changed from one roughness section to the next (Figure 2.3). A mixture of fine quartz sand ($D_{50} \approx$ 0.1 mm) and type I/II Portland cement (4:1 ratio by weight) was used to construct the non-erodible channel bed. This non-erodible mixture was poured into the channel form and leveled such that it covered the entire width and length of the channel form to a depth of 1cm. Before the non-erodible mixture of sand and cement cured, roughness elements were embedded into the mixture by randomly dropping sediment grains into the wet sand-cement mixture. This procedure resulted in roughness elements that were partially embedded on the surface of the sand-cement mixture. The non-erodible channel bed mixture was allowed to cure for 24 hr prior to construction of the erodible walls and 120 hr prior to the beginning of an experiment. The roughness elements became fixed upon complete curing of the sand-cement mixture.

Single experiments consisted of 3 or 4 bed roughness sections, each 2 m in length. The upstream most 1.0 to 1.5 m of the channel served to establish channel flow and minimize the influence of upstream boundary conditions prior to the first measurement section. Bed roughness in this 'equilibration' section was constructed to match the roughness in the first experimental section of the channel (Figure 2.3). Embedded particle size ranged from 1.2 mm to 16 mm over the set of three experiments and varied by as much as a factor of 6.5 within a single experiment channel (Table 2.1). Efforts were made to keep the areal density of roughness elements the same across all roughness sections. Due to the methods used to construct the beds, there is some variability in the areal density between sections. Using an overhead image of the bed, areal density was measured as the number of pixels occupied by roughness elements divided by the total number of pixels in the image. Areal density ranged from 0.23 in the section with 1.2 mm elements to a value of 0.56 in the section with 16 mm elements (both sections are from experiment DR, Table 2.1). Each experimental bed included a

control section that was free of embedded particles. In addition to varying the size of embedded particles, the downstream trend in bed roughness was varied. We report results from three experiments, each with a unique downstream bed roughness trend: increasing roughness ('IR'); decreasing roughness ('DR'); and alternating roughness ('AR') (Table 2.1).

2.2.3. Construction of Erodible Channel Walls

The channel walls were constructed directly on top of the non-erodible bed. This methodology allowed the bed roughness characteristics to be laterally consistent throughout an experiment even as lateral erosion of the channel walls exposed 'fresh' portions of the bed. The channel walls were constructed of a sand-kaolinite-cement mixture using fine quartz sand ($D_{50} \approx 0.1$ mm), industrial grade kaolinite and type I/II Portland cement. The sand and kaolinite were mixed together to form the 'aggregate' material for the channel walls with sand accounting for 98.75 % by weight of the aggregate material. The bulk aggregate material was then mixed dry with cement using a 90:1 ratio by weight of aggregate to cement. This sand-kaolinite-cement mixture was then added to water and mixed using a hand-held mud mixer until well mixed. The wet mixture was then placed in between the channel form and an interior channel cast that was placed directly on top of the channel bed in the center of the channel forms. The width of the channel cast (160 mm) set the width of the experimental channel. The thickness of erodible wall material was approximately 80 mm (Figure 2.2). Once in place, the sand-kaolinite-cement wall mixture was allowed to cure for 96 hours. After 96 hours, the interior channel cast was removed, leaving the channel ready for experimentation.

This experimental set up allowed us to: 1) isolate the process of lateral wear in bedrock channels and determine if rates of lateral bedrock erosion vary with changes in channel conditions; 2) investigate the potential of bedload particle impacts as a mechanism of lateral bedrock erosion and 3) characterize the influence of bed roughness on rates of lateral erosion.

2.2.4. Experimental and Data Collection Procedures

Each experiment started with the construction of a new experimental channel. Experiments consisted of an initial period of clear-water flow followed by multiple periods

in which bedload was introduced at the head of the channel at a constant rate. During each period of clear-water flow, water-surface elevation data were collected with an ultrasonic probe attached to a data acquisition cart. The water surface data were used to estimate initial shear stress conditions within each of the distinct roughness sections (Table 2.1). The duration of each period, typically 2 hr of run time, was chosen as a balance between the desire to capture as much information as possible on channel evolution and changes in erosion rate over time and the need for sufficient lateral erosion to occur such that an accurate signal could be obtained. At the end of each time period, water and sediment inputs were stopped and detailed elevation data of the bare experimental channel were collected using the laser scanning system attached to the flume. In general, experiments were considered complete following a time period in which the rate of lateral erosion within any channel section decreased to less than one-third of the rate from the previous period. Depending on the number of bedload supply periods, experiments lasted between 6 and 8 hr of run time.

The laser scanning system has three axes of motion and is capable of measuring bed and channel topography from overhead with a vertical precision of less than a millimeter. Data points were collected along a 2x2 mm grid oriented in the *x*-*y* plane. A rotating laser mount (Figure 2.4) allowed us to collect data points from the entire channel wall surface including areas that had been undercut by erosion. The laser mount has an axis of rotation oriented parallel to the longitudinal axis of the flume which allows the laser to be oriented at nine different angles (between 60° away from normal toward the right bank and 60° away from normal toward the left bank). A trigonometric correction was applied to the raw data so that the data points were correctly located in the *x*-*y* plane. Data points were also collected from the channel bed to confirm that the bed was not eroding. Each scan of the channel between runs resulted in a series of cross sections, uniformly spaced (2 mm) in the downstream direction, with data points that were non-uniformly spaced in the *y* and *z* directions.

2.2.5. Calculation of Lateral Erosion Rates

Rates of lateral wall erosion were calculated by measuring the change in the *y*-position of the channel wall at a given elevation from one time step to the next. Given the non-uniform spacing of data points in the *y* and *z* directions, an interpolation of the data

had to be performed prior to calculating the change in *y*-position between time steps. We used a triangle-based linear interpolation to create a uniform cross section grid of channel elevation data. All erosion rate calculations are based on the interpolated data. Lateral erosion rates were calculated for all cross sections within the data collection reach defined as the central meter of each roughness section (Figure 2.3). By using only data from the central meter of each roughness section, we minimize the effect of roughness transitions on our results. To calculate the erosion rate for an individual cross section, we integrate the erosion measurements at each elevation along the total height of the channel wall. This methodology produces an erosion rate that represents the area of material removed from the channel cross section per hour of run time. We then take an average of the individual cross-sectional erosion rates within the measurement section to arrive at a reach-averaged cross-sectional erosion rate for a given roughness section.

The primary source of measurement error comes from the precision of the laser itself. The manufacturer of the device (Keyence Corporation) states that the laser is capable of measuring distance to a point with sub-millimeter precision. Based on repeated scans of fixed surfaces in our experiments (i.e. the tops of the channel walls which did not erode), we estimate the measurement error to be ± 0.3 mm. For reference, the maximum change in the *y*-position (lateral erosion) of a particular point on the wall approached 30 mm or two orders of magnitude greater than the estimated measurement error.

2.2.6. Experiment IR – Bed Roughness Increasing Downstream

The length of the experimental channel for the subset of experiments with bed roughness increasing downstream was approximately 6 m with an additional 0.5 m of channel at the upstream end used to establish flow conditions in the experimental portion of the channel. Three distinct bed roughness sections were created each with a length of approximately 2 m. The upstream-most section of the channel was free of embedded particles and represented the control or ‘smooth’ section of the channel (a smooth section was present in all experimental channels to allow an unbiased comparison between roughness sections from all three experiments). The middle bed roughness section had 1.2 mm particles embedded in the non-erodible bed while the

downstream most section had 7.0 mm particles embedded in the non-erodible channel bed. Roughness characteristics of the 7.0 mm and 1.2 mm bed sections are shown in Table 2.1, including average free space between individual roughness elements and the areal concentration of elements (data about particle spacing and concentration is not applicable to the smooth channel sections as there are no embedded roughness elements). Construction of the erodible walls produced an initial channel width of 160 mm. The channel was subjected to an initial time period of clear-water flow followed by three time periods in which bedload was introduced at a constant rate at the head of the channel.

2.2.7. Experiment DR – Bed Roughness Decreasing Downstream

The length of the experimental channel for this experiment was approximately 8 m with an additional 0.8 m of channel length at the upstream end used to establish flow conditions in the experimental portion of the channel. Four distinct bed roughness sections were created, each with a length of approximately 2 m. The upstream-most roughness section was constructed using 16 mm embedded particles (the largest embedded particle size used in the set of experiments). In addition, the upstream 0.8 m of channel used to establish flow conditions also had 16 mm particles embedded in the non-erodible sand-cement mixture. Moving downstream, the next roughness section had 10 mm embedded particles followed by a section with 2.4 mm embedded particles and finally the downstream-most section was free of embedded particles. The characteristics of each roughness section are shown in Table 2.1.

Construction of the erodible walls produced an initial channel width of 180 mm. This experiment consisted of an initial time period of clear-water flow followed by two time periods in which bedload was introduced at a constant rate at the head of the channel. This experimental channel was slightly wider than the channels used in experiments IR and AR (180 mm versus 160 mm and 165 mm respectively). To compensate for the wider channel, we increased the sediment supply rate such that the supply rate of bedload particles per unit width remained constant for all experiments (Table 2.2).

2.2.8. Experiment AR – Alternating Bed Roughness

The length of the experimental channel for this experiment was approximately 8 m with an additional 0.8 m of channel at the upstream end used to establish flow conditions in the experimental portion of the channel. Four distinct bed roughness sections were created, alternating between rough and smooth sections. The upstream-most section had 10 mm particles embedded in the sand-cement bed mixture. In addition, the upstream 0.8 m of channel used to establish flow conditions also had 10 mm particles embedded in the channel bed mixture. Moving downstream, the next roughness section was free of embedded particles followed by a section of 4.7 mm embedded particles and finally another section free of embedded particles at the downstream end of the channel. The roughness characteristics of the distinct roughness sections are shown in Table 2.1. Construction of the erodible walls produced an initial channel width of 165 mm. This channel was subjected to an initial time period of clear-water flow followed by two time periods in which bedload was introduced at a constant rate at the head of the channel.

2.3. RESULTS

2.3.1. Variation in Lateral Erosion Rates

Clear-water Flow vs. Constant Bedload Supply

During periods of clear-water flow, reach-averaged cross-sectional erosion rates were negligible in all channel sections regardless of bed roughness type. During these periods, the reach-averaged cross sectional erosion rate (expressed in units of cross sectional area removed per hour of run time) varied between 2.6 and 9.7 mm^2hr^{-1} across all roughness sections. For channels with wetted cross sectional areas of 13,500 and 8,900 mm^2 respectively, these clear-water erosion rates represent the removal of less than 0.1% of the wetted cross sectional area.

During the first period of constant bedload supply, all roughness sections experienced an increase in reach-averaged cross-sectional erosion rates relative to those from the previous period of clear-water flow (Figure 2.5(a-c)). In smooth channel sections, erosion rates from the first period of bedload supply were 4 to 13 times greater than erosion rates from the previous period of clear-water flow. The effect of constant bedload supply on erosion rates in sections with fixed roughness elements was even more pronounced than it was in the smooth sections. In sections with fixed roughness

elements, erosion rates from the first period of bedload supply were 12 to 50 times greater than erosion rates from the previous period of clear-water flow.

Influence of Bed Roughness on Erosion Rate Variability

During periods of constant bedload supply, reach-averaged cross sectional erosion rates varied by as much as a factor of 7 between sections with and without roughness elements. Erosion rates during the first period of constant bedload supply are lowest in the smooth channel sections regardless of their location along the channel profile or the downstream roughness trend of an experiment (Figure 2.5(a-c)). A comparison of erosion rates between smooth and fixed roughness element sections from the same experiment shows that erosion rates in sections with roughness elements were 2 - 7 times greater than those measured in smooth sections during the first bedload supply period. The greatest difference in erosion rates between smooth and rough sections within the same experiment were observed in experiment IR, where the reach-averaged cross sectional erosion rate in the 7 mm roughness section was 220 mm^2hr^{-1}compared to 30 mm^2hr^{-1} in the smooth section (Table 2.2). The smallest difference in erosion rates between smooth and fixed element sections also occurred in experiment IR, where the reach-averaged erosion rate in the 1.2 mm roughness section (the smallest embedded particle used in the set of three experiments) was 70 mm^2hr^{-1} compared to 30 mm^2hr^{-1} in the smooth section. Expressed in terms of wetted cross sectional area removed per hour of run time, erosion rates in sections with fixed roughness elements are equivalent to the removal of 1-3% of the wetted cross sectional area while erosion rates in smooth sections are equivalent to the removal of less than 1% of the wetted cross sectional area.

To compare lateral erosion rates from all roughness sections in the set of three experiments, we normalized the reach-averaged cross-sectional erosion rate from rough sections by the reach-averaged cross-sectional erosion rate in the smooth section from the same experiment. Using data from the first bedload supply period, a plot of normalized erosion rate versus roughness element size shows that rates of lateral bedrock erosion are variable and are sensitive to changes in channel bed roughness (Figure 2.6). In particular, these results indicate that the addition of roughness elements to an otherwise smooth bed can substantially increase rates of lateral bedrock erosion in the presence of vigorous bedload transport. We also note that the increase in lateral

erosion rates associated with the addition of fixed roughness elements is not a linear function of roughness element size. For example, the addition of 1.2 mm roughness elements resulted in a moderate increase in normalized erosion rate (~1.4 times smooth section rate) while the addition of 2.4 mm roughness elements resulted in a normalized erosion rate four times that measured in the corresponding smooth section. The non-linear behavior of erosion rates as a function of roughness element size can also be seen in the apparent stabilization of erosion rates that occurs as the size of the roughness element continues to increase beyond the 2.4 mm roughness element.

Variation in Erosion Through Time

The reach-averaged cross-sectional erosion rate decreased in all sections with fixed roughness elements between the first and second time periods in which bedload particles were introduced (red line versus blue line in Figure 2.5(a-c)). However, the magnitude of the decrease between time periods varies with the size of fixed roughness element. All smooth sections with the exception of one (smooth section in the increasing roughness experiment) also experienced a decrease in erosion rate between the first and second time periods of bedload supply.

Considering only those sections with fixed roughness elements, we note that the section with the smallest embedded particle (1.2 mm) experienced the smallest decrease in erosion rate between the first and second time periods of bedload supply (Figure 2.5(a)). In the section with 2.4 mm embedded particles (Figure 2.5(b)), the reach-averaged erosion rate during the second time period of bedload supply is roughly half of the erosion rate during the initial period of bedload supply. In roughness sections with embedded particles 4.7 mm or greater, erosion rates from the second period of bedload supply are consistently about 1/3 of those from the first time period.

Longitudinal Variation in Erosion

Simple inspection of the longitudinal profiles of cross-sectional erosion from the first period of bedload supply (red lines in Figure 2.5(a-c)) reveals a correlation between the size of the roughness element on the bed and the magnitude of the variation in erosion among individual cross sections. The correlation is best seen in experiment DR (Figure 2.5(b)) where the size of the roughness element changes from 16 mm at the head of the channel to 2.4 mm near the downstream end of the channel. In the section with the largest roughness elements (16 mm), individual cross-sectional erosion rates along a

single channel wall vary from a minimum of 20 mm^2hr^{-1} to a maximum of 125 mm^2hr^{-1} (roughly a factor of 6), with a standard deviation of 27 mm^2hr^{-1}. In the section with the smallest roughness elements (2.4 mm), individual cross-sectional erosion rates from a single channel wall vary from 50 mm^2hr^{-1} to 125 mm^2hr^{-1} (roughly a factor of 2.5), with a standard deviation of 12 mm^2hr^{-1}. And in the smooth channel section of experiment DR, individual cross-sectional erosion rates along a single channel wall vary from 10 mm^2hr^{-1} to 30 mm^2hr^{-1} (roughly a factor of 3) with a standard deviation of 4 mm^2hr^{-1}. These data indicate that as the mean free path between adjacent roughness elements increases (13 mm between particles in the case of the largest roughness element versus 6 mm between particles in the case of the smallest roughness element), cross-sectional erosion rates display greater spatial variability.

This result supports our hypothesis that lateral bedrock erosion is driven by the deflection of bedload particles into the channel wall by roughness elements on the bed. In the case of smaller roughness elements where the space between adjacent elements is roughly equal to the size of the bedload particle in transport (4.7 mm bedload particles versus a mean free path between roughness elements of 6 mm), the roughness elements behave as a quasi-continuous deflection surface, producing a more longitudinally uniform pattern of erosion. In cases where the mean free path between adjacent roughness elements is larger than the bedload particle size, deflection events are spatially discontinuous and produce greater longitudinal variability in erosion.

2.3.2. Hydraulic Regime and Bedload Transport Conditions

Flow depth measurements collected at the beginning of the first bedload supply run (Table 2.1), allow us to estimate the hydraulic regime and bedload transport conditions present in each of the distinct roughness sections presented in this paper. Using the measured flow depth and approximate roughness height ($k_s = 1.5\mathrm{h_p}$ where h_p is the protrusion height of embedded particles) we calculate the roughness Reynolds number ($u_* k_s/\nu$) to distinguish between hydraulically rough and hydraulically smooth flow for each roughness section. In channel sections with an embedded particle size of 2.4 mm or greater, the roughness Reynolds number (Table 2.1) is well above the minimum value for hydraulically rough conditions ($u_* k_s/\nu > 100$). These results indicate that in sections with an embedded particle size of 2.4 mm or greater, the viscous sublayer is interrupted

by roughness elements on the bed that strongly influence flow turbulence. A roughness Reynolds number of ~105 for the section with 1.2 mm embedded particles indicates that flow conditions are closer to the 'transitional' regime than sections with larger roughness elements. Finally, a roughness Reynolds number of ~8 in the smooth channel sections indicates a transitional to smooth hydraulic flow regime in the absence of embedded particles.

Using the measured flow depths and other fixed experimental variables, we estimate the bedload particle transport stage (τ^*/τ^*_c) in each roughness section. Without correcting for form drag, the bedload transport stage ranged from 9.5 in the section with the largest roughness element to 6.1 in sections without embedded particles (Table 2.1). These high transport stages are consistent with observations of vigorous bedload transport and negligible deposition of bedload particles during the experiments. Water surface elevation data was collected during the initial minutes of experiments IR and AR to produce longitudinal profiles of flow depth (Figure 2.7). In general, the flow depth profiles show greater flow depths in sections with larger roughness elements, indicating greater total boundary shear stress. However, it is important to note that after correcting for form drag, the shear stress available for transport is greatest in the sections with smaller roughness elements. The profile of flow depth for experiment IR (Figure 2.7 (a)) shows the highest flow depth in the smooth section at the head of the channel. This result does not reflect the channel conditions within the smooth section but rather can be attributed to upstream boundary conditions and the lack of an equilibration section upstream of the experimental channel. An equilibration section (1 m in length) was installed upstream of the first experimental section in both experiments DR and AR. The success of this equilibration section in minimizing the effect of upstream boundary conditions can be seen in the flow depth profile for experiment AR (Figure 2.7 (b)) where flow depth is reasonably stable in the upstream most section of that experiment.

2.3.3. Erosion Morphology

Channel wall erosion was limited to a zone near the base of the channel wall with a maximum height of erosion reaching 0.4 to 0.5 times the flow depth (or about six bedload particle diameters above the channel bed). Within this erosion zone, rates of lateral wall erosion were greatest at the elevation where bed and bank intersect and

decreased progressively up to the maximum height of erosion. This spatial pattern of erosion produced channel walls that were largely unaltered from the water surface down to mid-flow depth at which point the walls become increasingly undercut toward the base of the wall (Figure 2.8).

The cross section morphology and maximum height of wall erosion were similar across all sections with fixed roughness elements except the section with sand-sized elements (1.2 mm). Figure 2.9 shows a representative cross section from each roughness section following the first time period in which bedload was introduced. The plots are shown at the scale of a single channel wall to help visualize the undercut morphology and to be able to show the maximum height of erosion and maximum width of lateral incision observed in each roughness section. The maximum height of erosion for a single cross section was defined as the maximum height at which a lateral erosion threshold of 0.5 mm was exceeded. Section-averaged values for maximum height and maximum width of erosion were calculated for each roughness section to permit comparison of these metrics between different roughness sections. For roughness sections with embedded particles 2.4 mm or greater (plots c–g), the section-averaged values for maximum height and maximum width of erosion are very similar following the initial period of bedload supply. The maximum heights of erosion above the bed within these five distinct roughness sections fall within a range of 25 to 31 mm above the bed. The maximum widths of erosion (i.e. the maximum change in the *y*-position of the wall at a given elevation) within these five distinct roughness sections fall within a range of 18 to 23 mm.

2.3.4. Experiment IR – Increasing Roughness Downstream

The longitudinal profile of cross-sectional erosion rates during the first period of bedload supply (red line – Figure 2.5(a)) shows a positive correlation between the size of the fixed roughness element on the bed and rates of lateral erosion in that channel section. As mentioned previously, this particular experiment exhibits the largest difference in erosion rates between a section with fixed roughness elements (7 mm roughness element) and the smooth channel section. We note that reach-averaged erosion rates along the left channel wall in the smooth section of this experiment are anomalously low for all periods with constant bedload supply (Table 2.2 - similar in

magnitude to erosion rates during periods of clear-water flow). The smooth section of this experiment was located at the head of the channel, where influence from upstream boundary conditions associated with the initiation of channelized flow and the introduction of bedload material at a point will be greatest. This experiment also had the shortest distance between the initiation of channelized flow and the first channel section in which data were collected. These channel conditions, along with the large difference between left wall and right wall erosion rates in the smooth channel section (right wall erosion rates are an order of magnitude greater than left wall erosion rates), led us to treat the left wall erosion rate in this section as an outlier.

If we normalize lateral erosion rates for this experiment using the result from the right channel wall as a representative lateral erosion rate in the smooth channel section, we calculate a normalized erosion rate in the 7 mm roughness section of 4.5 times the erosion rate in the smooth channel section (during the first period of bedload supply). Normalizing the lateral erosion rate in the 1.2 mm roughness section in the same manner results in a normalized erosion rate of 1.4 times the erosion rate in the smooth channel section (again during the first period of bedload supply). Using these new values for normalized erosion rates from experiment IR, we again plot normalized erosion rate as a function of roughness element size for all roughness sections used during the set of experiments (Figure 2.10). Instead of showing a distinct erosion rate peak associated with the 7 mm roughness element section (Figure 2.6), the adjusted plot indicates that erosion rates increase significantly with the addition of 2.4 mm roughness elements followed by an apparent stabilization in erosion rates as the size of the roughness element on the bed continues to increase.

Inspection of the variation in erosion rate with time from experiment IR shows that total cross-sectional erosion rates remain relatively stable between the first (BL-1) and second (BL-2) periods of bedload supply in both the smooth section and the section with 1.2 mm roughness element (Figure 2.5(a)). This is in contrast to the total cross-sectional erosion rate between periods BL-1 and BL-2 in the section with 7 mm roughness elements where the erosion rate in period BL-2 is about one third of that from period BL-1. Erosion rates in all sections of the experiment decrease between period BL-2 and BL-3 with reach-averaged cross-sectional erosion rates being very similar in all three sections of the channel during period BL-3.

This experimental channel was subjected to three periods of constant bedload supply compared to only two periods of constant bedload supply for the other experimental channels. This additional period of constant bedload supply allows us to track the evolution of channel width near the base of the wall in more detail for each of the three roughness sections. The 'channel width' data presented here are simply the distance between points of maximum lateral erosion in a cross section, averaged over all cross sections within the data collection reach. These data do not represent the average channel width but rather the width of the undercut zone, providing some sense of how channel width is changing through time and how the width over which bedload particles are transported changes with time. All three channel sections have a width at the base of the wall of roughly 160 mm prior to the first period of bedload supply. The reach-averaged channel widths near the base of the wall at the end of the third period of bedload supply are 170, 177 and 195 mm in the downstream direction (Table 2.2). The greatest rate of change in near-bed channel width occurs during the first period of bedload supply in the section with 7 mm roughness elements, going from an initial width of 160 mm to width of 188 mm at the end of period BL-1 (Table 2.2).

2.3.5. Experiment DR – Decreasing Roughness

Similar to the results from experiment IR, this experiment clearly shows that in the presence of vigorous bedload transport, rates of lateral erosion increase significantly with the addition of fixed roughness elements to an otherwise smooth bed (Figure 2.5(b)). Perhaps the most striking result from experiment DR is the lack of a positive correlation between lateral erosion rate and roughness element size. In simply looking at the longitudinal profile of cross-sectional erosion rates, it becomes apparent that the moving average of cross-sectional erosion rate remains relatively constant between the sections with fixed roughness elements despite decreasing the size of the roughness element from 16 mm at the head of the channel to 10 mm and down to 2.4 mm in the downstream-most section with roughness elements. In contrast to results from experiment IR where the addition of the smallest roughness element used in that experiment (1.2 mm) resulted in only a moderate increase in lateral erosion rates, the smallest roughness element used in experiment DR (2.4 mm particles) resulted in a

significant increase in lateral erosion rates compared to rates in the smooth channel section.

2.3.6. Experiment AR – Alternating Roughness

Similar to the results of experiments IR and DR, results from experiment AR show that rates of lateral erosion increase significantly with the addition of fixed roughness elements to an otherwise smooth channel bed (Figure 2.5(c)). One of the most striking results from this experiment is the short downstream distance over which lateral erosion rates change from being elevated in sections with fixed roughness elements (the first and third channel section of this experiment with 10 mm and 4.7 mm roughness elements respectively) to being very low in smooth channel sections (the second and fourth channel sections in this experiment). To quantify this erosion rate transition, we compare local erosion rates at distances equivalent to one flow depth (~65 mm in the section with 10 mm roughness elements) upstream and downstream of the transition from 10 mm elements to a smooth bed. The local erosion rate one flow depth upstream from the roughness transition is 140 mm^2hr^{-1} compared to a local erosion rate of 69 mm^2hr^{-1} one flow depth downstream of the transition. At a distance of two flow depths downstream of the transition the local erosion rate is 53 mm^2hr^{-1}. These data show that the local erosion rate decreases by almost two-thirds over a distance of two flow depths downstream of the roughness transition.

2.4. DISCUSSION

The results presented in this paper indicate that bedload particle impacts are an effective mechanism of lateral bedrock erosion. Erosion due to this mechanism appears to be confined to a zone near the base of the channel wall. Our results suggest this zone of erosion extends vertically from the channel bed up to a height of approximately 6 bedload particle diameters above the bed (or roughly 2.5 times the maximum saltation hop height of the bedload particle). We note that this vertical range of erosion reflects the simplified conditions of our experiments (single grain size, constant discharge and slope). Natural bedrock channels on the other hand transport a range of bedload particle sizes and are subject to variable rates of discharge. This variability would likely cause

the vertical range of erosion by bedload impacts to be greater than that observed in the experiments.

An investigation into the effectiveness of bedload particle impacts as a mechanism of vertical bedrock erosion showed that impacts of particles as small as sand-sized bedload particles can drive incision of the channel bed [Sklar and Dietrich, 2001]. If this observation is transferable to the process of lateral bedrock erosion, it is likely that lateral erosion due to bedload particle impacts is constrained only by the need for active transport of bedload particles of any size and the presence of roughness elements capable of deflecting those particles. Given that the transport of sediment as saltating bedload is nearly ubiquitous in bedrock channels when the full range of discharge events is considered, lateral erosion by bedload particle impacts is likely an important mechanism of erosion in most bedrock channel systems.

If lateral erosion by bedload particle impacts is an active mechanism in most bedrock channels, we need to account for the fact that the undercut morphology observed in our experiments is not readily observed in natural bedrock channels. While there are some examples of this undercut morphology, as seen along the Kettle River near Sandstone, Minnesota (Figure 2.1), the majority of bedrock channels have cross sections that are more or less trapezoidal in shape with channel walls that slope inward toward the channel thalweg. One possible explanation for the lack of undercut channel walls observed in natural bedrock channels is that the undercut morphology is only a temporary condition that is quickly followed by failure of the channel bank or wall. Another explanation for the apparent lack of undercut banks in natural bedrock channels is a steady lowering of the channel bed due to vertical incision that occurs in concert with lateral erosion. In our experiments, the fixed channel bed allowed bedload particle impacts to attack the same elevation for an extended period of time. If a channel bed is being lowered continuously by the process of vertical bedrock incision, the zone of lateral erosion via bedload particle impacts would gradually shift down as well, thus preventing continuous lateral erosion at a fixed elevation. We also put forth the possibility that undercut channel banks are rarely observed because the zone of lateral erosion occurs below baselevel flow and thus is not easily observable.

In our experiments, rates of lateral erosion via bedload particle impacts are influenced by channel bed roughness through its effect on the deflection of bedload

particles by roughness elements and on transport stage. To our knowledge, the deflection of bedload particles by roughness elements has never been investigated as a potential driver of lateral bedrock erosion. We propose that the deflection of bedload particles plays an important role in directing bedload particles into channel walls and ultimately is the primary process driving lateral bedrock erosion via bedload particle impacts.

The role of this deflection process in driving lateral erosion is supported by at least two key experimental results. First, the minimal rates of lateral erosion in smooth channel sections during periods of constant bedload supply suggest that downstream transport of saltating bedload particles is not sufficient on its own to cause significant lateral erosion. The minimal erosion that does occur in the smooth channel sections is likely due to the transport of bedload particles very close to the wall where slight deviations of those particles from their downstream path (due to turbulence or collisions with other bedload particles) can result in contact with the channel wall. The second experimental result that points to the existence of a deflection process is the longitudinal variation in lateral erosion rates and the greater periodicity found in sections with larger roughness elements. We argue these results support our hypothesis of lateral bedrock erosion being driven by the deflection of bedload particles into the channel wall by roughness elements on the bed. In the case of smaller roughness elements where the space between adjacent elements is roughly equal to the size of the bedload particle in transport (4.7 mm bedload particles versus a mean free space between roughness elements of 6 mm for the section with 2.4 mm roughness elements), the roughness elements behave as a quasi-continuous deflection surface, producing a more longitudinally uniform pattern of erosion. In cases where the mean free space between adjacent roughness elements is larger than the bedload particle size, deflection events are spatially discontinuous and produce greater longitudinal variability in erosion. This variation suggests that bedload particle impacts are driven by localized processes (i.e. deflection by discrete roughness elements) rather than turbulent flow which is more likely to act as a spatially continuous driver of particle impacts when integrated over a sufficiently long time period.

One of the most important observations to emerge from this set of experiments is that rates of lateral bedrock erosion are variable over space and time depending on

channel bed roughness, channel width and bedload transport stage. This observation is in contrast to a numerical modeling study of strath terrace formation in which rates of lateral erosion showed no correlation with changes in sediment supply, remaining almost constant despite an order of magnitude change in sediment supply rates [Hancock and Anderson, 2002]. The discrepancy in the behavior of lateral erosion rates could be due to the implementation of a simplified lateral erosion rule in the numerical model. The authors of the study acknowledge that the specific mechanisms of lateral bedrock erosion are poorly understood and therefore they elected to scale rates of lateral erosion with shear stress on the bed [Hancock and Anderson, 2002]. As one might expect, implementation of this scaling relationship produced rates of lateral erosion that were correlated with discharge and shear stress on the bed, but not with bedload transport rate [Hancock and Anderson, 2002].

Fluid shear stress has been used to predict rates of lateral erosion in other numerical studies of bedrock channel erosion [Wobus et al., 2006; Stark, 2006]. Implementation of a shear stress based lateral erosion rule has been successful in producing flights of strath terraces [Hancock and Anderson, 2002] and reasonable self-formed bedrock channel geometries [Wobus et al., 2006; Stark, 2006]. The success of these models begs the question of whether it is necessary to incorporate specific mechanisms of lateral erosion into bedrock erosion models. To this question, we point out that shear stress based lateral erosion rules produce a roughly linear relationship between shear stress and rates of lateral erosion [Wobus et al., 2006; Hancock and Anderson, 2002]. Our results, however, indicate that rates of lateral bedrock erosion via bedload particle impacts do not scale linearly with shear stress on the bed. Instead, as the size of roughness elements on the bed continues to increase, and with it shear stress on the bed (Table 2.1), the change in rates of lateral erosion flattens out (Figure 2.10). This stabilization in erosion rates is due in part to a trade-off between more frequent particle deflections associated with larger roughness elements (due to a greater deflection surface area) and a corresponding decrease in the shear stress available for bedload transport due to an increase in form drag associated with larger elements.

The non-linear relationship between shear stress and lateral erosion rates is also evident in the behavior of lateral erosion rates at relatively low values of shear stress corresponding to smoother channel sections (Figure 2.11). The low rates of lateral

erosion found in both the smooth channel sections and the section with 1.2 mm roughness elements suggest that a minimum bed roughness is required to cause a significant increase in rates of lateral erosion compared to an otherwise smooth channel bed. In non-dimensional terms, our results suggest the minimum roughness threshold is crossed at a roughness element to bedload particle size ratio of approximately 0.5. We note that rates of lateral erosion appear to be at their maximum when the roughness element is similar in size to the bedload particle, represented by experimental channel sections with roughness elements diameters of 2.4 mm, 4.7 mm and 7 mm (with size ratios of 0.53, 1.0 and 1.5 respectively).

Finally, our results show a significant decrease in rates of lateral erosion through time (Figure 2.5(a-c)). This observation is similar to the numerical predictions of Hancock and Anderson [2002] where lateral erosion rates decrease slightly over time due to a decrease in the likelihood of the channel interacting with the valley wall as the valley widens through time. The decrease in rates of lateral erosion over time within the same roughness section that we observe could be due to several factors: 1) the increase in channel width results in a reduced particle transport rate per unit width (assuming a uniform lateral distribution and constant sediment supply), which reduces the number of particles transported close to the wall and thus limits the number of deflections that result in high energy particle impacts on the wall; 2) the increase in channel width over time, coupled with maintaining a constant discharge over time, results in a reduced shear stress on the bed, a lower particle transport stage and a reduction in the kinetic energy of bedload particles upon impact with the wall; and 3) the undercut morphology may be creating or enhancing secondary flow structures that inhibit lateral particle motion toward the channel wall.

The areal concentration of roughness elements was held roughly constant during the entire set of experiments. Therefore, our experiments do not address the potentially important influence of roughness element density on the deflection of bedload particles. Roughness element density may indeed play an important role in determining particle deflection rates, hydraulic flow conditions and ultimately rates of lateral erosion. In order to maintain a constant areal concentration from one roughness section to the next, we changed the spacing between elements with the mean free path between elements increasing along with an increase in roughness element size. For a given size roughness

element, changes in the mean free path between elements could play an important role in setting lateral erosion rates for that particular size element. The spacing between elements could become very important in cases where the bedload particles are similar or larger in size than the roughness elements on the bed. In this case, tightly packed roughness elements may prevent bedload particles from striking toward the base of a roughness element where collision with a high angle deflection surface can impart significant lateral momentum to the bedload particle. We note that our experiments used partially to well-rounded particles as roughness elements. The shape of roughness elements may be important in determining the amount of deflection surface area with an orientation that maximizes the generation of lateral particle momentum.

2.5. CONCLUSIONS

Erosion via bedload particle impacts appears to be an effective mechanism of lateral bedrock erosion. This mechanism should be active, to some degree, in bedrock channels that transport bedload at high transport stages and that have relatively immobile roughness elements present on the bed. Erosion associated with this mechanism is confined to a small vertical zone of erosion near the base of the channel wall where bedload particles are actively saltating downstream. The deflection of bedload particles by roughness elements on the bed appears to be the primary driver of lateral bedrock erosion via particle impacts.

The influence of channel bed roughness on rates of lateral bedrock erosion emerges through the role that roughness elements play in deflecting bedload particles and through their role in establishing hydraulic and bedload transport conditions. There are two primary ways in which roughness elements influence rates of lateral erosion. First, as roughness element size increases relative to channel width and flow depth a greater fraction of the channel cross section becomes occupied by potential deflection surfaces. The result is that a greater percentage of bedload particles passing through a cross section will be deflected and potentially impact the wall. On the other hand, as the roughness element size increases and the element protrudes higher up into the flow, a greater percentage of the total flow momentum is extracted in overcoming the increase in form drag associated with the larger roughness element. The result is an overall decrease in the ability of the flow to transport sediment and a decrease in the

downstream momentum of bedload particles (prior to deflection). These two effects serve to counter act each other and prevent rates of lateral erosion from continuing to increase as the roughness element size and total shear stress on the bed increase.

Contrary to previous numerical studies of lateral bedrock erosion, our experiments show significant variability in rates of lateral erosion under a constant discharge scenario. The variability in lateral erosion rates is strongly correlated with changes in bed roughness. Most of the variability occurs in the transition from a smooth bed (roughness element diameter << bedload diameter) to a rough bed consisting of roughness elements that meet or exceed the minimum threshold size (approximately 0.5 times the bedload particle size).

In the case of lateral erosion by bedload particle impact, the trade-off between an increase in the number of particles deflected into the wall and the reduction in transport capacity due to greater form drag produces a scenario in which rates of lateral erosion are not linearly related to shear stress on the bed. This result is driven by the fundamental role that roughness elements play in the deflection of bedload particles into the channel wall.

Figure 2.1 - (Top) Undercut bank along the Kettle River near Sandstone, MN. The channel is incised into a weak sandstone along this particular reach. (Bottom) Longitudinal groves and particle impact wear marks in the channel wall of a narrow bedrock canyon (picture courtesy of Leonard Sklar).

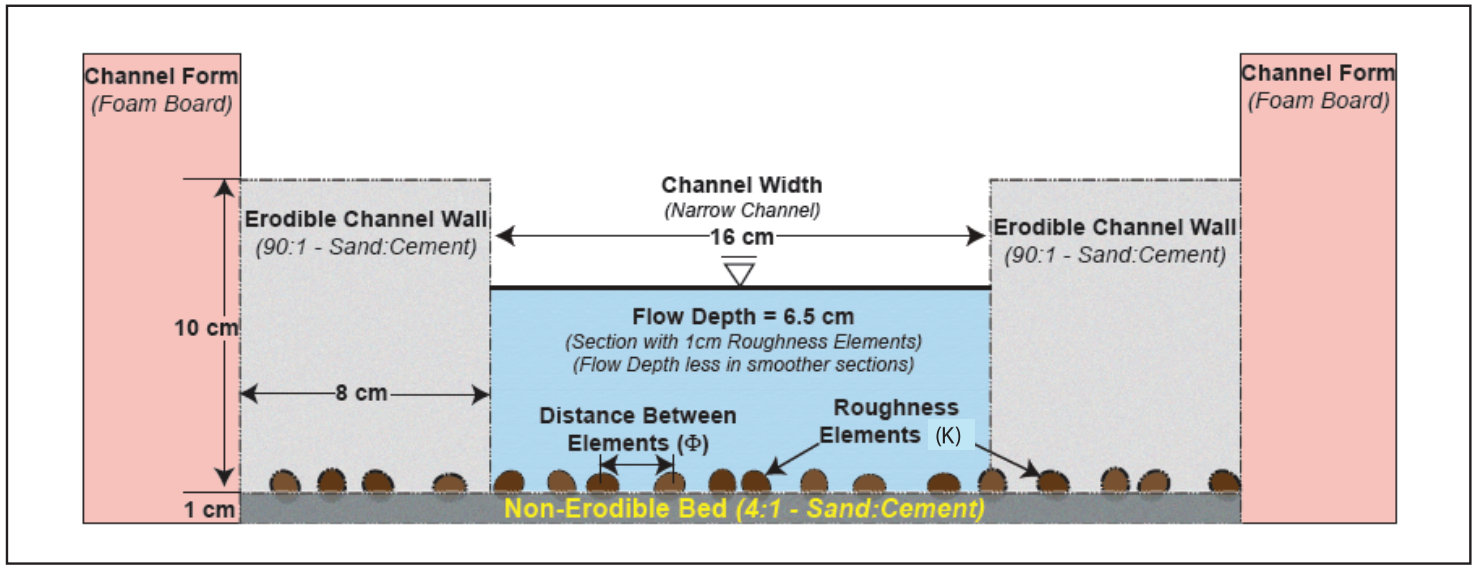

Figure 2.2 – Cross section of experimental channel. Pink foam walls glued to the base of the confining flume served as the lateral boundaries for the experiments. A non-erodible mixture of sand and cement was poured in between the foam walls to a depth of 1 cm, immediately followed by random placement of sediment particles (roughness elements) into the mixture. The bed was allowed to cure for 24 hours creating a non-erodible surface with embedded roughness elements. An erodible mixture of sand and cement was placed on top of the non-erodible bed to construct the channel walls.Each erodible wall was ~80 mm in cross sectional width, creating an experimental channel that was approximately 160 mm in width. With measured flow depths ranging from ~50 to 75 mm depending on the size of the embedded particles, width to depth ratios were in the narrow range of observed bedrock channels (W/H between 2 and 3). The areal concentration of embedded particles was kept roughly constant across different roughness sections different sized embedded particles (D). As a result, the distance between individual elements varied between roughness sections with different embedded particle size.

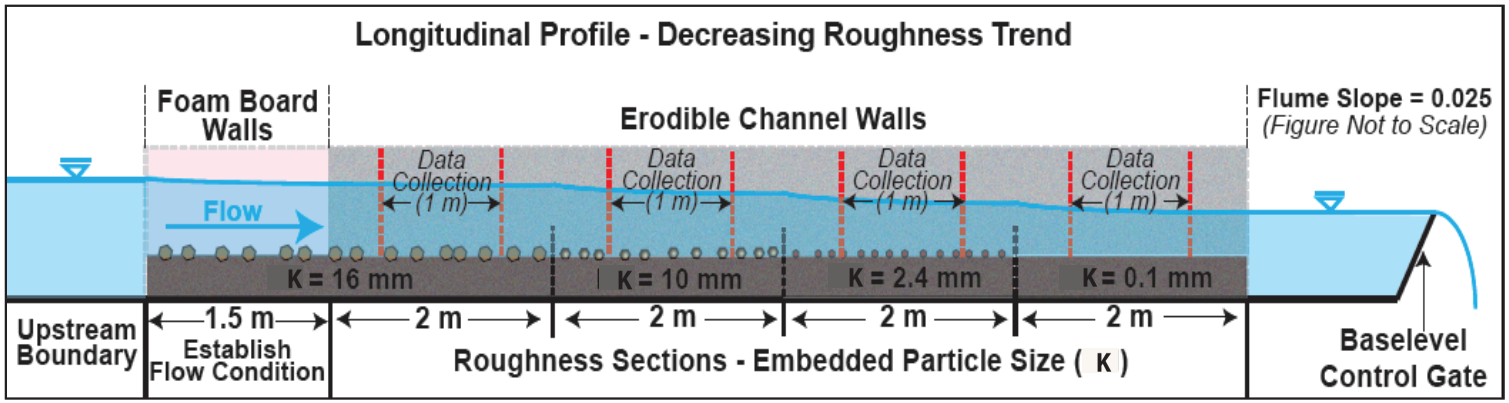

Figure 2.3 - Longitudinal profile of a representative experimental channel. Discharge entered the experimental channel boundaries (formed by the pink foam walls) from a head tank located at the head of the confining flume. The initial 1.0 to 1.5 m of the channel was constructed with foam board walls and a channel bed that was identical to that of the first experimental section of the channel in order to minimize the influence of upstream boundary conditions. Each roughness section in the experimental channel (i.e. erodible walls) is 2 m in length. The transition from one roughness section to the next is abrupt. In order to minimize the influence of these roughness transitions, only data from the central meter of each roughness section was analyzed and included in the results presented here. Base level was held constant for the duration of an experiment using a hinged control gate at the end of the confining flume.

Table 2.1 : Experimental Channels & Initial Conditions

Channel Type by Roughness Trend (Experimental-ID#)	Roughness Element Size [mm] Bed Sections				Particle Concentration Bed Sections				Mean Free Path [mm] Bed Sections				Channel Width [mm]	Initial Conditions: Flow Depth [mm]				Shields Stress [τ*]				Transport Stage [τ*/τ*$_{cl}$]				Roughness Reynolds #			
	A	**B**	**C**	**D**	**A**	**B**	**C**	**D**	**A**	**B**	**C**	**D**		**A**	**B**	**C**	**D**	**A**	**B**	**C**	**D**	**A**	**B**	**C**	**D**	**A**	**B**	**C**	**D**
Increasing (IR)	sm	1.2	7.0	-	na	0.23	0.50	-	na	5.0	8.0	-	160	61	56	62	-	0.21	0.19	0.21	-	7.7	7.1	7.8	-	9	105	647	-
Decreasing (DR)	16.0	10.0	2.4	sm	0.56	0.51	0.34	na	13.0	11.0	6.0	na	180	*75*	*65*	*55*	*50*	0.25	0.22	0.19	0.17	9.5	8.2	7.0	6.3	1627	947	209	8
Alternating (AR)	10.0	sm	4.7	sm	0.45	na	0.47	na	11.0	na	7.0	na	165	65	52	54	48	0.22	0.18	0.18	0.16	8.2	6.6	6.8	6.1	947	8	345	8

All Channels: Bed Slope = 0.025; Discharge = 12.8 L/s.
All 'Bed Sections' are 2 meters in length except: Channel AR-section B = 2.5m and Channel AR-section D = 1.5m.
A = Upstream Most Section; **D** = Downstream Most Section; transition between bed sections is abrupt.
Roughness Element Size = diameter of embedded sediment particle; sm = smooth section (no embedded particles)
Mean Free Path = average distance between centers of adjacent roughness particles
Flow Depth for Decreasing Roughness (DR) is based on hand held measurement.
Roughness Reynolds # (u^*k_s/ν)

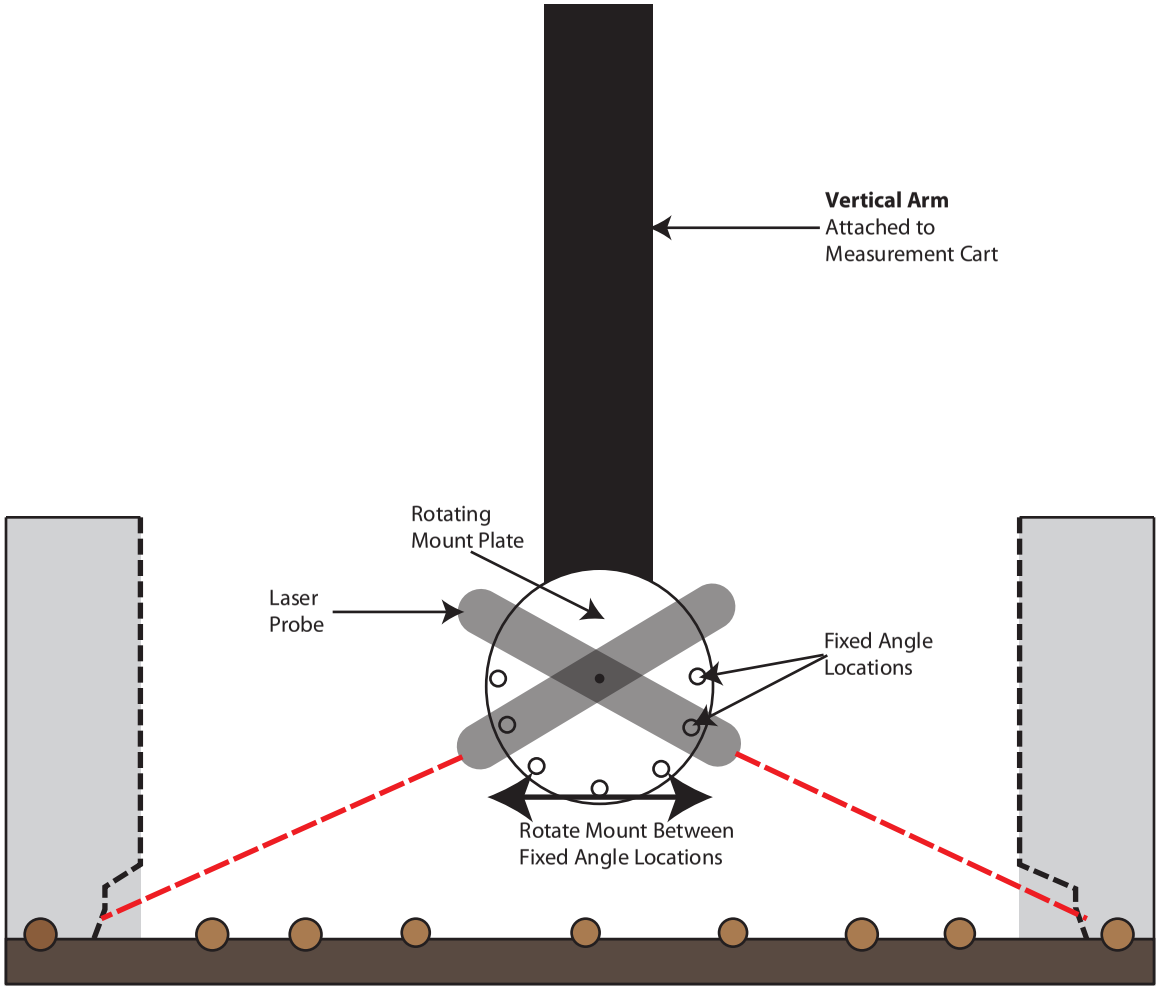

Figure 2.4 – Rotating laser mount used to collect elevation data from wall locations that had been undercut. The laser probe is fixed to a rotating plate. The plate can be locked in 7 fixed positions, allowing the laser probe to be oriented at angles of 30°, 45° and 60° from the bed-normal position.

Table 2.2 : Lateral Erosion Rates Per Roughness Section Through Time

	Bed Sections						Near Bed Width [mm]*				Average Cross Section Erosion Rate (by Bed Section)							
	Element Size [mm]				Run	Q_s	(Beginning of Period)				ErosionRate-LeftWall [mm^2/hr]				ErosionRate-RightWall [mm^2/hr]			
Roughness Trend (ID#)	A	B	C	D	Period	[cm^3/s]	A	B	C	D	A	B	C	D	A	B	C	D
Increasing(IR)	sm	1.20	7.0	-	Clear	0.0	160	160	160	-	1.59	2.14	1.24	-	5.59	3.38	3.57	-
					BL-1	27.0	166	170	188	-	5.33	32.97	110.10	-	23.96	35.88	105.63	-
					BL-2	27.0	169	176	194	-	4.75	17.27	35.83	-	26.80	51.26	32.42	-
					BL-3	27.0	170	177	195	-	2.37	6.10	10.45	-	15.19	12.04	10.47	-
Decreasing(DR)	16.0	10.0	2.40	sm	Clear	0.0	183	181	183	183	1.68	1.91	2.02	0.78	0.98	1.84	2.69	5.24
					BL-1	31.5	203	203	207	191	59.44	63.95	78.88	17.57	73.73	69.22	89.52	22.81
					BL-2	31.5	209	209	219	194	28.09	27.22	48.69	7.49	22.92	24.77	45.17	9.27
Alternating(AR)	10.0	sm	4.70	sm	Clear	0.0	165	165	165	163	7.80	3.47	4.84	5.63	1.08	1.08	4.84	3.59
					BL-1	27.0	194	173	199	174	107.40	33.30	145.03	42.65	111.83	25.76	132.18	38.53
					BL-2	27.0	198	175	206	177	32.99	14.02	46.51	14.44	44.76	8.89	52.80	16.71

*Near bed width is the width between points of maximum lateral erosion on each wall in a cross section, averaged over the data collection reach.

*Near bed width represents the undercut channel width near the channel bed at the beginning of each run period.

sm = smooth section

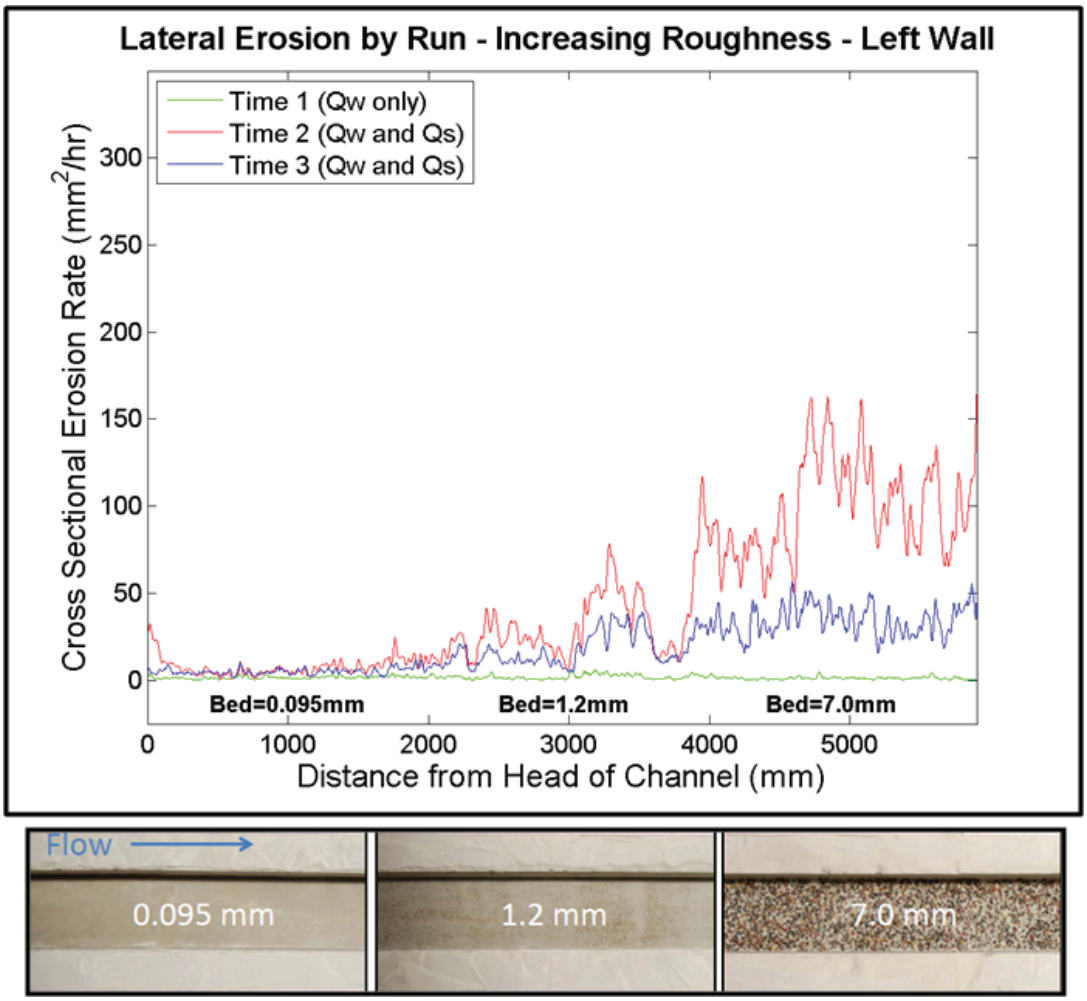

Figure 2.5(a) – Longitudinal profile of cross section erosion rates for the period of clear-water flow (green) and two periods of bed load supply (first period (red), second period (blue)). Erosion rates are for a single wall, expressed as the cross sectional area of bedrock removed per time. The photograph shows the increasing bed roughness conditions of experiment IR. Roughness sections are approximately 2 m in length (see Table 2.1 for exceptions).

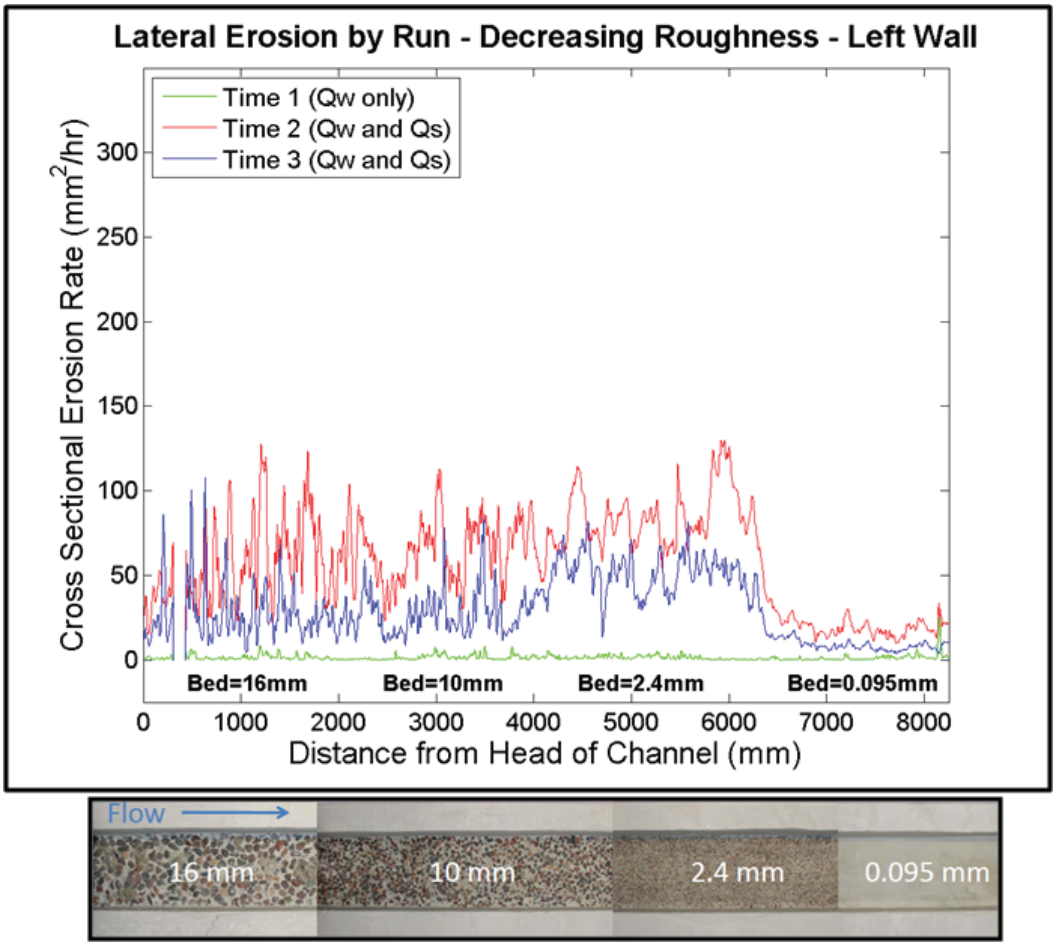

Figure 2.5(b) – Longitudinal profile of cross section erosion rates for the period of clear-water flow (green) and two periods of bed load supply (first period (red), second period (blue)). Erosion rates are for a single wall, expressed as the cross sectional area of bedrock removed per time. The photograph shows the decreasing bed roughness conditions of experiment DR. Roughness sections are approximately 2 m in length (see Table 2.1 for exceptions).

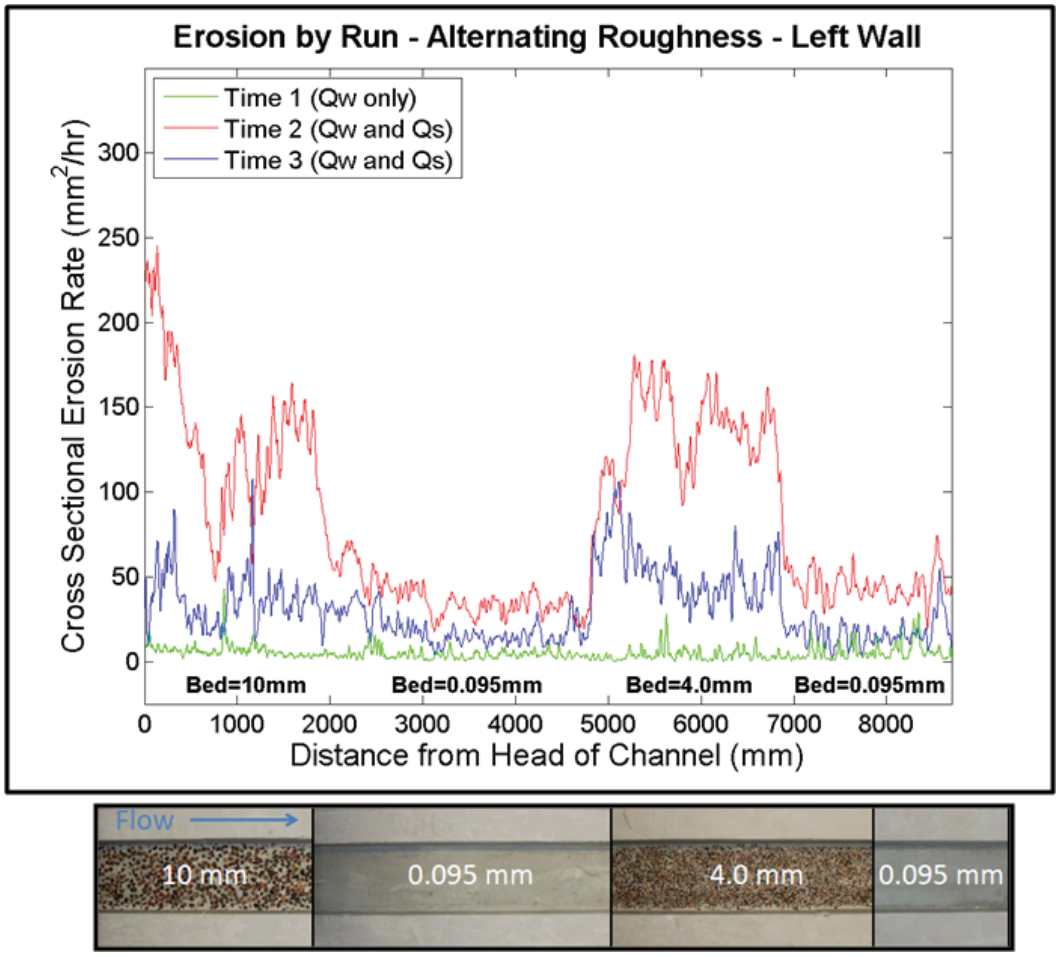

Figure 2.5(c) – Longitudinal profile of cross section erosion rates for the period of clear-water flow (green) and two periods of bed load supply (first period (red), second period (blue)). Erosion rates are for a single wall, expressed as the cross sectional area of bedrock removed per time. The photograph shows the alternating bed roughness conditions of experiment AR. Roughness sections are approximately 2 m in length (see Table 2.1 for exceptions).

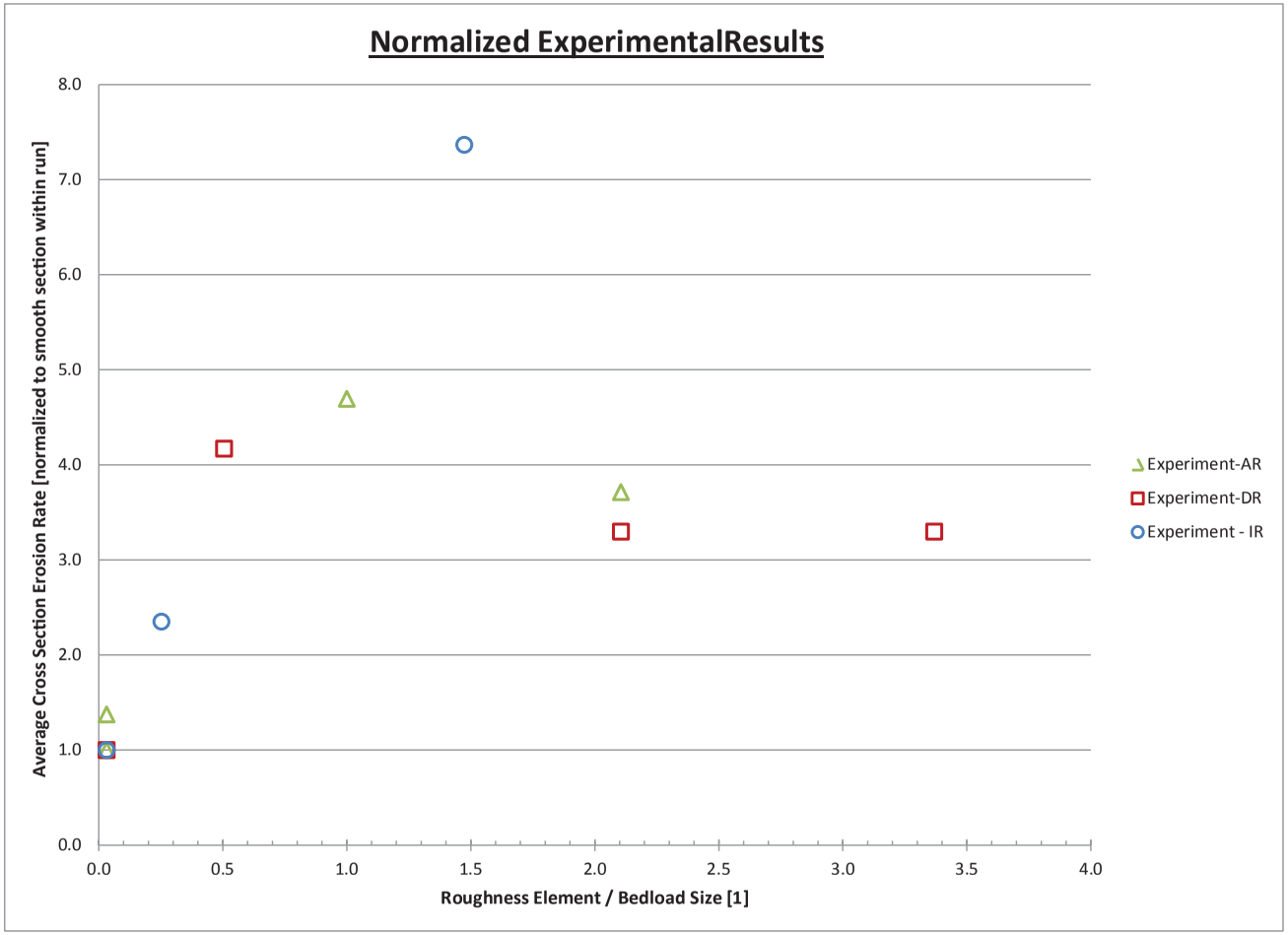

Figure 2.6 – Section averaged cross-sectional erosion rate as a function of roughness element size. Erosion rates are normalized to that found in the smooth section of the same experimental channel. Roughness element size is normalized to the bed load particle diameter. Symbols indicate experimental run: blue circles (IR); red squares(DR); green triangles(AR).

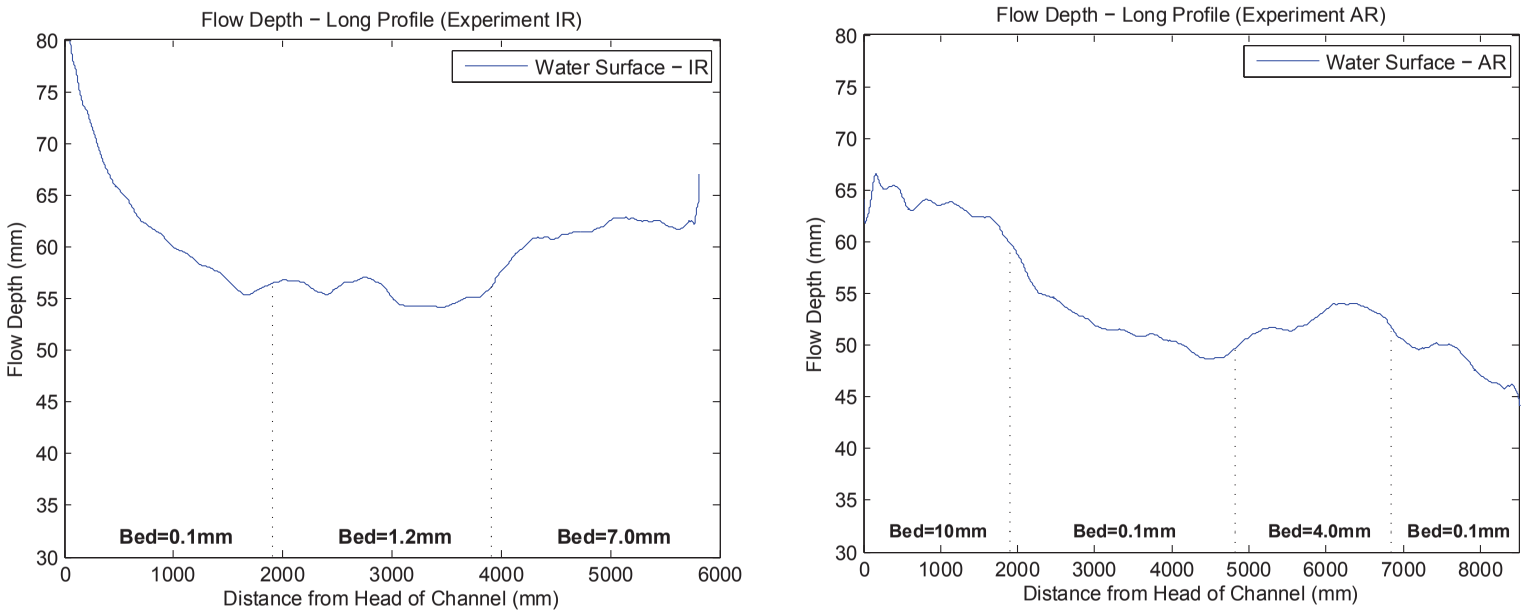

Figure 2.7 - Longitudinal profiles of flow depth for experiments IR and AR. Flow is from left to right. The distinct roughness element sections are indicated by the dashed vertical lines with the element size noted on plot.

1.2 mm Roughness Element

2.4 mm Roughness Element

4.7 mm Roughness Element

7 mm Roughness Element

10 mm Roughness Element

16 mm Roughness Element

Figure 2.8 – Oblique overhead images of lateral wall erosion. Note undercut banks in sections with roughness elements 2.4 mm and greater. Longitudinal variation in erosion becomes more pronounced as the size and space between roughness elements increases.

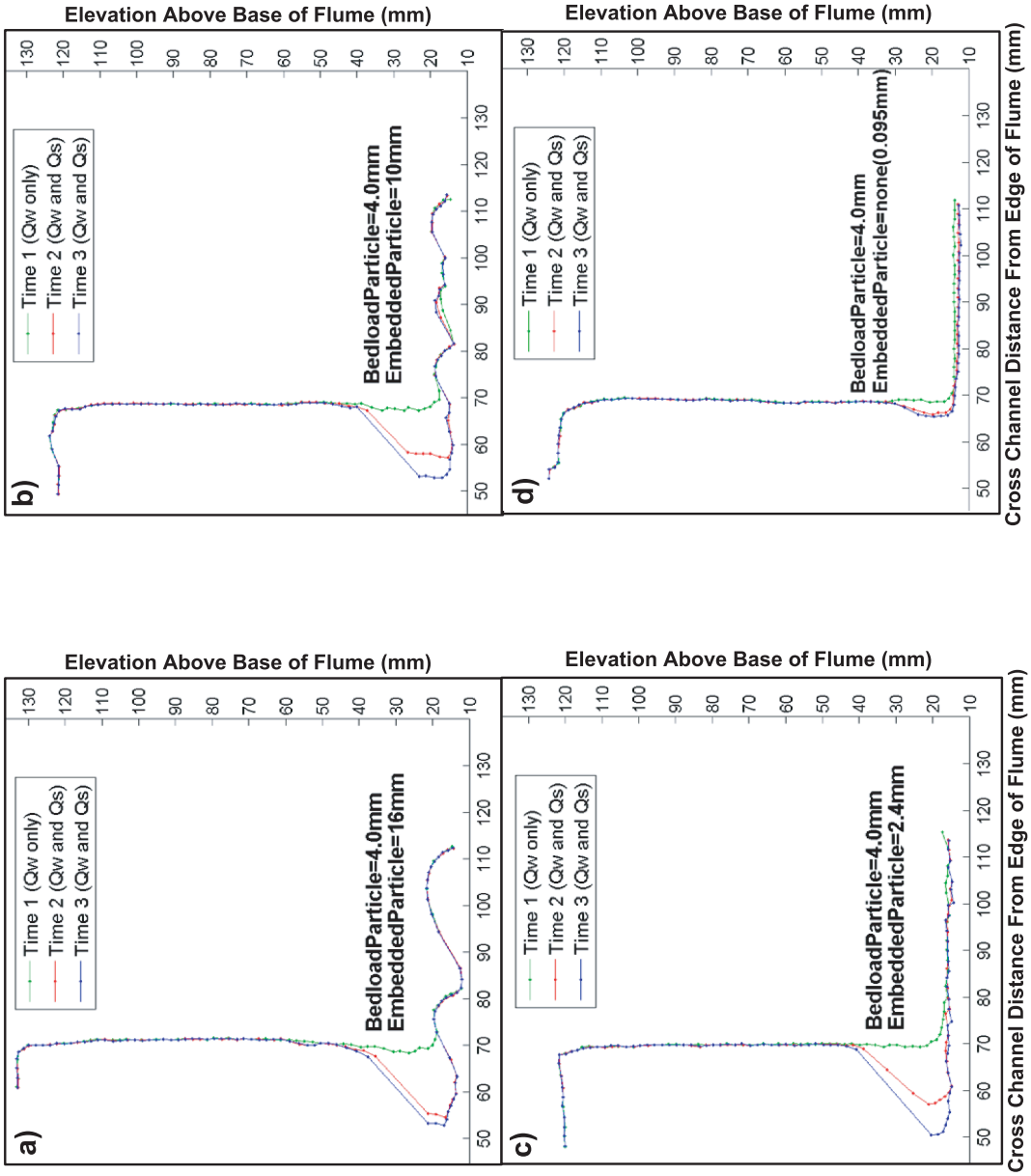

Figure 2.9 – Channel wall profiles through time for roughness sections in experiment DR: a) 16 mm; b) 10 mm; c) 2.4 mm; d) smooth. Profiles represent end of following periods: clear-water flow (green); initial bed load supply (red); second bed load supply (blue).

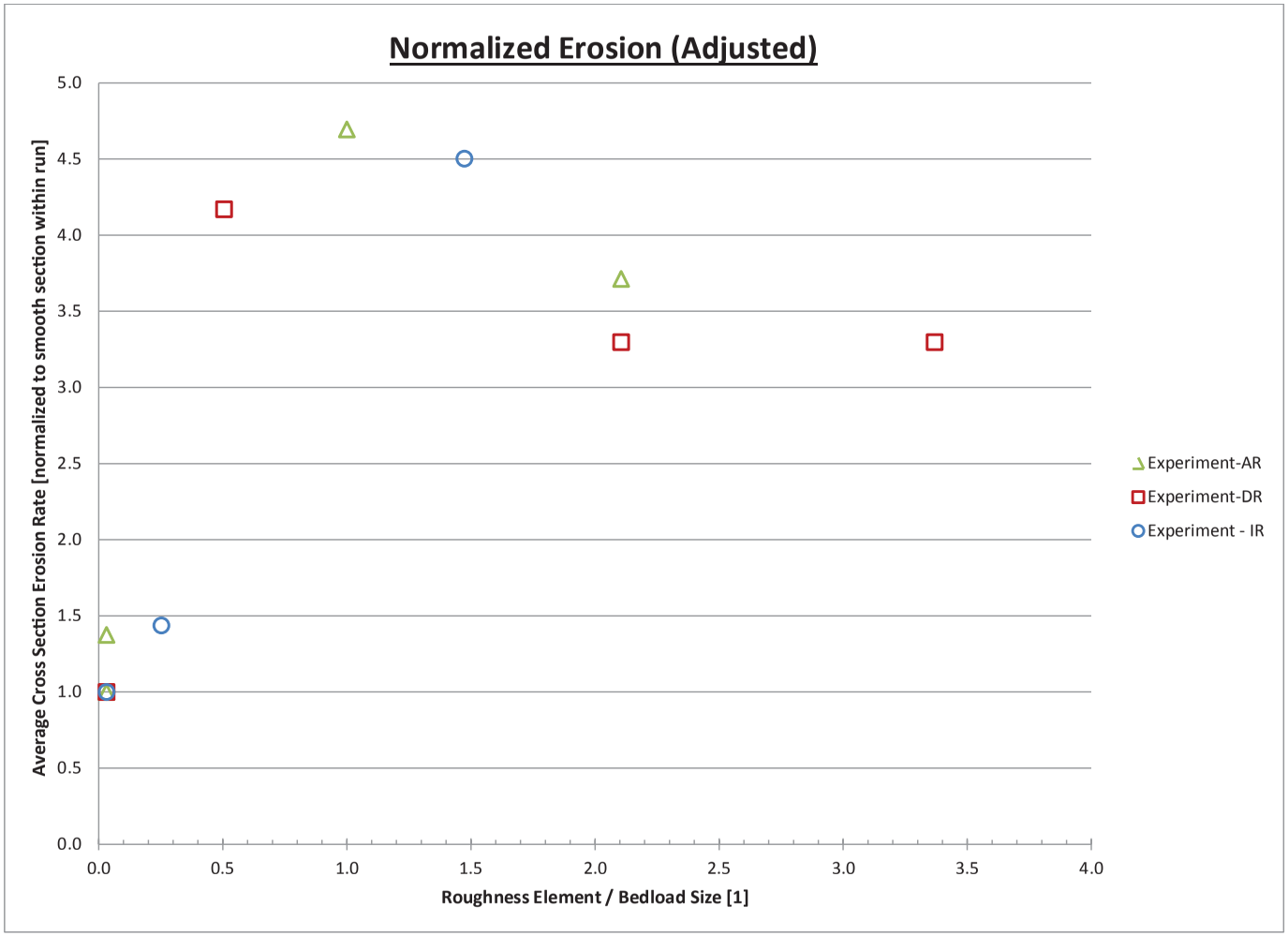

Figure 2.10 – Section-averaged cross-sectional erosion rate as a function of roughness element size after adjustment of values from experiment IR. Symbols are the same as in Figure 2.6.

Figure 2.11 – Section-averaged cross-sectional erosion rate as a function of shields stress. Symbols are the same as in Figure 2.6. Sections with roughness elements that do not meet the minimum roughness threshold plot as a distinct group (circled). Note the inverse relationship between erosion rate and shields stress in sections with significant erosion.

CHAPTER 3

A numerical investigation of lateral bedrock erosion via bedload particle impacts: the influence of channel bed roughness.

3.1. INTRODUCTION

Lateral erosion of bedrock channel walls plays an important role in maintaining equilibrium channel geometries and provides an additional degree of freedom for bedrock channels to respond to changes in boundary conditions. Field and experimental investigations of bedrock channel erosion reveals different mechanisms in specific environments, but the geomorphic community lacks a well-documented, widely applicable and specific mechanism of lateral bedrock erosion. In weak, clay-rich lithologies, for instance, enhanced lateral erosion of the channel wall has been observed at elevations above base flow where the rock is preferentially weakened by wetting and drying during seasonal variations in discharge [Montgomery, 2004; Stock et al., 2005]. While this mechanism is intriguing as an explanation for lateral planation in clay-rich lithologies, field observations indicate that lateral bedrock erosion occurs in more resistant lithologies as well (Larson and Dorn, 2010; Lee et al., 2011; Reneau, 2000). An experimental study of wall erosion in slot canyons indicates that wall erosion is related to fluid flow in the form of back-eddies on the lee side of wall undulations [Carter and Anderson, 2006]. However, the authors of the study note that this particular mechanism may only be applicable in very narrow channels where much of the flow resistance comes from the channel walls. It seems likely that a more universal mechanism of lateral bedrock erosion exists, one that covers diverse lithologies and geometries.

Despite the uncertainty surrounding a universal and well-understood mechanism for lateral bedrock erosion, several researchers have incorporated the process into numerical investigations of bedrock channel processes. These numerical investigations include studies of bedrock channel geometry [Stark, 2006; Wobus et al., 2006] and studies of strath terrace formation [Hancock and Anderson, 2002]. In each of these studies, the authors have incorporated the process of lateral bedrock erosion into their models by assuming that rates of lateral bank erosion scale with shear stress on the bed. The fact that investigators have chosen to incorporate lateral erosion into their models without a clear understanding of the mechanism speaks to the importance of lateral bedrock erosion in determining the overall response of bedrock channels to change. An improved understanding of the

mechanism(s) of lateral bedrock erosion would clearly benefit the geomorphic community.

In contrast to the uncertainty surrounding mechanisms of lateral erosion, mechanisms for vertical incision of the channel bed are well-established [Whipple et al., 2000]. These mechanisms include bedload particle impacts, plucking of fractured or weathered rock and erosion due to cavitation. It has been suggested that bedload particle impacts are the most universal mechanism of vertical bedrock incision given the ubiquitous transport of saltating bedload particles in bedrock channels [Sklar and Dietrich, 2004]. These well-established mechanisms of vertical bedrock incision serve as a basis from which potential mechanisms of lateral bedrock erosion can be investigated. A reasonable place to begin this investigation is by examining the most universal mechanism of vertical incision as a potential mechanism of lateral bedrock erosion.

Applying bedload particle impacts to the problem of lateral bedrock erosion requires consideration of some important differences between bedload particles striking the channel bed versus the channel wall. Unlike the channel bed, which is frequently protected from impacts by channel deposits, the channel walls remain largely exposed to particle impacts. More frequent bedrock exposure on the walls has the potential to increase the susceptibility of channel walls to erosion by bedload particle impact. However, in contrast to the acceleration of particles toward the channel bed by gravity in the case of vertical incision, there is no constant force driving bedload particles into the wall. For bedload particle impacts to be a viable mechanism of lateral erosion, there must be a process through which saltating particles obtain sufficient lateral momentum to cause erosion upon impact with the wall.

Here we present a physical model designed to investigate bedload particle impacts as a ubiquitous mechanism of lateral wall erosion in bedrock channels. The model considers channel wall erosion due to particle impacts associated with a downstream flux of saltating bedload particles. Collisions between saltating bedload particles and bed roughness elements are incorporated as the primary process by which saltating particles obtain ‘erosionally effective’ lateral momentum (see Figure 3.1 for conceptualization of collisions between bedload particles and bed roughness

elements). Depending on the incoming particle velocity and the orientation of the roughness-element surface at the point of collision, the model calculates the initial post-collision velocity components of the deflected bedload particle. Following a collision, the model evaluates the balance of wall-normal and bed-normal forces acting on a deflected particle to determine the wall-normal velocity and elevation of the particle upon impact with the channel wall. The volume of material eroded per unit time is a function of wall-normal particle impact velocity and the rate of particle impacts.

We use the model to evaluate the influence of bed roughness parameters such as roughness-element size, protrusion height and roughness-element spacing on rates of lateral wall erosion via bedload impacts. Form drag associated with the protrusion of roughness elements from the bed proves to be an important control on the variation of lateral erosion rates as a function of roughness-element size. Our model results suggest that rates of lateral erosion due to bedload particle impacts are influenced by a trade-off between an increase in roughness-element size and the concomitant increase in form drag. The increase in roughness-element size increases the rate of particle deflections due to a greater collision surface area. However, that increase in the rate of particle deflections is counter-acted by the increase in form drag that reduces the shear stress available for bedload transport and ultimately reduces the wall-normal impact velocity of deflected particles. Additionally, our model results reproduce the undercut bank morphology that we observed in the set of physical of experiments described in chapter 2 and that we have observed in the field.

3.2. MODEL DEVELOPMENT

3.2.1. Background

The process of vertical bedrock incision via particle impacts has been well-studied, providing potentially valuable insight into the process of lateral bedrock erosion. Erosion of brittle material, including bedrock, by particle impacts is thought to be driven by local increases in rock tensile stress associated with individual particle impacts [Bitter, 1963; Sklar and Dietrich, 2004]. The local increase in tensile stress leads to the generation of small cracks in the brittle material. Repeated

particle impacts lead to the formation and detachment of material fragments, a process referred to as “deformation wear” [Bitter, 1963]. In the case of vertical bedrock incision, the rate of bedrock detachment due to particle impact is thought to scale with the component of particle kinetic energy that is normal to the bed surface upon particle impact [Sklar and Dietrich, 2004]. In the case of lateral wall erosion, the rate of bedrock detachment should scale with the square of the wall-normal component of particle impact velocity (assuming the mass of the bedload particle does not change during deflection or wall impact).

Determining the wall-normal component of particle impact velocity in a model of lateral bedrock erosion requires an adequate representation of the process by which saltating bedload particles acquire significant wall-normal momentum. Detailed studies of bedload particle transport have shown that the collision of saltating particles with the bed at the end of a saltation hop influences the saltation trajectory of the subsequent hop [Wiberg and Smith, 1985; Nino et al., 1994]. The experimental study of Nino et al. [1994] identifies two modes of collision between saltating particles and the channel bed: those that result in particle rebound and successive saltation hops and those that result in sliding or rolling of the particle and a temporary break in saltation. Data from this experimental study show that the saltation trajectory of rebounding particles is both higher and longer than the initial trajectory of a particle that was temporarily at rest. The authors of this study identify bed configuration at the point of collision, as well as general bed roughness, as the channel parameters that determine the particular mode of collision and saltation trajectory. An earlier theoretical study of bedload transport [Wiberg and Smith, 1985] showed that collisions with the bed at the end of a saltation hop can increase the subsequent saltation hop height by almost a factor of two compared to hop heights of particles initially at rest on the bed (i.e. hops not preceded by a collision with the bed).

These two studies provide evidence that collisions between saltating particles and bed roughness elements result in the transfer of particle momentum from one saltation hop to the next. We posit that these collisions are a likely source of wall-normal particle momentum. While Nino et al. [1994] were focused on particle motion in the vertical and downstream directions, their identification of bed parameters that

influence saltation trajectories can be applied to the current problem of determining how saltating particles obtain significant lateral momentum. We propose that the ability of collisions to direct saltating particles into the wall depends on: 1) the orientation of the bed or bed roughness element at the point of collision and 2) the size of a roughness element relative to that of a saltating particle. Bedrock channels in particular exhibit significant bed roughness due to the presence of large grains on the bed and the presence of erosive bedrock features. Thus, bedrock channels seem particularly well suited to produce laterally-effective collisions, where 'laterally-effective' describes a collision in which the bedload particle acquires the lateral momentum necessary to cause erosion on impact with the channel wall.

Before developing expressions to predict the lateral momentum of individual bedload particles, we consider how the mechanism of laterally deflected bedload particles should be modeled at the cross section scale to predict a rate of lateral wall erosion. In their model of vertical incision via particle impacts, Sklar and Dietrich [2004] assert that the rate of bedrock detachment from the channel bed is a function of three primary variables: 1) the rate of particle impacts on the bed; 2) the volume of bedrock removed per particle impact and 3) the fraction of bedrock exposed to direct particle impact. We take a similar approach in developing our model but do not include a term for the fraction of exposed bedrock, effectively assuming that the entire height of the channel wall is exposed to attack by saltating bedload particles. At the cross section scale, we express the bulk rate of lateral wall erosion (E) as the product of two terms: the volume of material removed per particle impact (ε) and the number of particles impacting the wall per unit time (I)

$$E = \varepsilon I \tag{1}$$

Below, we develop expressions for these two terms by considering the forces acting on individual bedload particles and the influence of bed roughness, bedload supply and bedload transport conditions on the rate of laterally-effective particle deflections. Key aspects of the model include: 1) the calculation of sediment transport conditions using a correction for form drag; 2) development of a bed

roughness metric that describes the likelihood of a saltating particle colliding with a roughness element; 3) determination of the wall-normal and bed-normal particle velocity components immediately following a collision and 4) evaluation of wall-normal and bed-normal forces acting on a deflected particle from the instant following collision to the time of wall impact.

3.2.2. Hydraulic and Bedload Transport Conditions

Hydraulic conditions are calculated from a set of fixed input parameters including discharge *(Q_w)*, flow depth *(H)*, channel width *(B)* and slope *(S)*. The following relations are used to estimate mean flow velocity *(U)*, resistance due to skin friction in a smooth reference reach *(C_{ref})* and shear stress available for bedload transport *(τ_{bs})*:

$$U = \frac{Q_w}{HB} \tag{2}$$

$$C_{\mathrm{ref}} = \frac{gR_{\mathrm{ref}}S}{U_{\mathrm{ref}}^2} \tag{3}$$

$$\tau_{bs} = \rho C_{\mathrm{ref}} U^2 \tag{4}$$

where *g* is acceleration due to gravity, R_{ref} is the hydraulic radius within a smooth reference reach and ρ is the density of water. Assuming a longitudinally-constant slope, discharge and channel geometry, the shear stress available for bedload transport (τ_{bs}) is calculated using the flow velocity in the channel section of interest *(U)* and the bed resistance coefficient from the smooth reference reach *(C_{ref})*. The use of equation (4) in sections with roughness elements requires that shear stress due to skin friction can be expressed as: $\tau_{bs} = \tau_b - \tau_{bf}$, where τ_b is total boundary shear stress and τ_{bf} is shear stress due to form drag. In the results section to follow, the model uses the channel geometry, channel inputs and empirical data from the

set of physical experiments conducted in the previous chapter. Flow depth measurements from the set of physical experiments in the previous chapter allow the model to calculate values for C_{ref} using equations (2) and (3) above.

Based on the shear stress available for transport (τ_{bs}), we calculate the mean values of downstream saltation velocity *(u_s)* and saltation hop height *(h_s)* for bedload particles in transport using the empirical relationships of Sklar and Dietrich [2004].

$$\frac{u_s}{\left(\left(\frac{\rho_s}{\rho}-1\right)gd_s\right)^{0.5}} = 1.56\left[\left(\frac{\tau^*_{bs}}{\tau^*_c}\right)-1\right]^{0.56} \quad (5)$$

$$\frac{h_s}{d_s} = 1.44\left(\frac{\tau^*_{bs}}{\tau^*_c}-1\right)^{0.50} \quad (6)$$

In equations (5) and (6) above, ρ_s is the bedload particle density, d_s is the bedload particle diameter, τ^*_{bs} is the Shields stress due to skin friction ($\tau^*_{bs} = \left(\tau_b - \tau_{bf}\right)/(\rho_s - \rho)gd_s$), and τ^*_c is the critical Shields stress for particle motion (τ^*_c = 0.04 for model results presented here). These two equations are the best-fit linear regressions through an ensemble of empirical data taken from multiple saltation trajectory studies. These equations are intended to represent the mean values of particle velocity and hop height at a given transport stage. These equations do not capture the dependence of particle velocity on height above the bed. However, as we discuss below, the model accounts for the bed-normal component of particle velocity in its calculation of the incoming particle velocity vector. As shown below, the bed-normal component of incoming particle velocity is calculated as a function of the height of the collision event relative to the maximum hop height, where a collision very close to the bed will result in a greater bed-normal component of particle velocity than a collision near the top of a saltation hop. While neglecting the variation in downstream particle velocity with height above the bed due to fluid shear, this methodology does capture some of the variation in particle velocity as a function of height above the bed.

3.2.3. Collisions between Bedload Particles and Bed Roughness Elements

It is assumed that saltating bedload particles have negligible lateral momentum during the course of a downstream hop such that we set the wall-normal component of particle velocity prior to collision equal to zero. The downstream component of incoming particle velocity (u_s) is calculated using equation (5) above and the bed-normal component of incoming particle velocity (w_s) is calculated using the following set of equations from Lamb et al. (2008):

$$G = \frac{(\rho_s - \rho)}{\rho_s} g \tag{7}$$

$$C_2 = \frac{1}{2} C_d \left(\frac{\rho}{\rho_s}\right)\left(\frac{a_s}{\ell_s}\right) \tag{8}$$

$$w_s = -\sqrt{\frac{G}{C_2}(1 - e^{-2C_2 dz})} \tag{9}$$

where C_d is the drag coefficient, a_s is the cross-sectional area of the saltating bedload particle, ℓ_s is the volume of the saltating particle and dz is the distance the particle has fallen upon collision with a roughness element (calculated as the difference between the peak hop height (h_s) and the elevation at which the collision occurs). Equation (9), as written above, reflects the coordinate system used in our model in which upward particle velocity has a positive sign.

The collision of bedload particles with roughness elements, and the subsequent conversion of downstream particle momentum into wall-normal and bed-normal components, is modeled using a simple vector reflection methodology shown below.

$$\boldsymbol{p} = \left(\frac{\boldsymbol{i_s} \cdot \widehat{\boldsymbol{n}}}{\widehat{\boldsymbol{n}} \cdot \widehat{\boldsymbol{n}}}\right)\widehat{\boldsymbol{n}} \tag{10}$$

$$\boldsymbol{r} = (\boldsymbol{i_s} - 2\boldsymbol{p})C_r \tag{11}$$

In equations (10) and (11) above, $\boldsymbol{i_s}$ is the incoming saltation velocity vector, $\widehat{\boldsymbol{n}}$ is a unit vector normal to the surface of the roughness element at the point of collision, $\boldsymbol{p}$ is the projection of the incoming particle velocity vector onto the surface normal vector, $\boldsymbol{r}$ is the particle velocity vector following collision and C_r is the coefficient of restitution describing the loss of particle momentum during the collision between bedload particle and roughness element. As shown in Figure 3.1, the incoming velocity vector has a downstream velocity component (u_s) and a fall velocity component (w_s) but no lateral velocity component such that: $\boldsymbol{i_s}$ = [u_s, 0, w_s]. The model assumes that all bedload particles have the same downstream velocity component upon collision with a roughness element. In contrast, the model allows the fall velocity component to vary depending on the height of the collision event (or the distance below the peak hop height). Calculating the fall velocity component as a function of the height of a collision event allows for some variation in the incoming velocity vector ($\boldsymbol{i_s}$) within a given roughness section. Incorporating variation in the fall velocity component also leads to greater total particle momentum as the particle approaches the mean bed surface.

The magnitude of the rebound velocity vector ($\boldsymbol{r}$) and its components immediately after a collision ($\boldsymbol{r}$ = [u_r, v_r, w_r]) is determined by the height of the collision and the orientation of the roughness element surface at the point of collision (see Figure 3.1 for a conceptual illustration of a collision). To illustrate the dependence of the rebound components on the height of a collision and the orientation of the deflection surface, imagine a bedload particle that strikes a roughness element head on at the base of the element. At this location, the magnitude of the incoming velocity vector is maximized because the collision occurs near the bed where w_s is greatest. This should maximize the rebound velocity vector ($\boldsymbol{r}$) for the given set of conditions. However, because the surface normal vector is pointing directly upstream and is parallel with the channel bed, a collision at this location will result in temporary

particle momentum in the upstream direction with negligible wall-normal and bed-normal components. In contrast, imagine a collision near the base of a roughness element where the surface normal vector is parallel to the bed but oriented at a 45 degree angle relative to the incoming particle velocity vector. In this case, the rebound velocity vector will still be maximized, but this time there will be a substantial wall-normal component of rebound velocity (v_r in Figure 3.1) with negligible downstream and bed-normal components.

Using the vector reflection methodology described above, we look to the theoretical analysis of Wiberg and Smith [1985] to determine the coefficient of restitution (C_r), and thus the magnitude of the rebound velocity vector, for a collision between a saltating bedload particle and the channel bed. The work of Wiberg and Smith [1985] suggests that upon collision with the bed, a saltating particle rebounds with a portion of its incoming momentum. Wiberg and Smith [1985] suggest a coefficient of restitution equal to 0.4 to describe the relationship between incoming particle momentum and the fraction of that momentum that is retained by the particle following a deflection event. We use a value of 0.4 for the coefficient of restitution in our model based on this work.

3.2.4. Wall-Normal Particle Velocity: a force balance approach

Given a laterally-effective collision between bedload particle and roughness element, the model needs to estimate how much material will be removed when the deflected particle collides with the channel wall. The volume of material removed on impact is thought to scale with the component of particle kinetic energy normal to the bedrock surface [Sklar and Dietrich, 2004]. Assuming the mass of the bedload particle remains constant, the wall-normal kinetic energy on impact, and thus the volume of material removed, depends solely on the wall-normal velocity of the particle on impact.

Assuming wall-normal particle momentum is negligible prior to deflection and there is no change in particle mass due to the deflection event, the wall-normal particle velocity immediately after deflection (v_r) is set equal to the wall-normal component of the particle rebound vector ($\boldsymbol{r}$). Following deflection, the wall-normal particle velocity will decay with distance and time due to fluid drag (assuming wall-

normal acceleration of the particle due to turbulence is negligible). To track this change in velocity, we construct a first order differential equation that describes the balance of wall-normal forces exerted on the bedload particle following a deflection event.

Assuming fluid drag is the only wall-normal force acting on the particle after deflection, we set the change in the wall-normal component of particle momentum equal to the wall-normal component of fluid drag force:

$$-\frac{d(vm)}{dt} = \frac{1}{2}\rho\pi\left(\frac{d_s}{2}\right)^2 C_d v^2 \tag{12}$$

where v is the instantaneous wall-normal particle velocity, m is the mass of the deflected bedload particle and C_d is the drag coefficient (we set C_d = 0.45 which roughly represents drag on a sphere in flows with Reynolds numbers between 10^3 and 10^5 [Parker, 2004]). The instantaneous wall-normal particle velocity (v) is used to represent the relative velocity between the particle and the fluid for the purpose of estimating fluid drag. We rearrange equation (12) to solve for the change in particle velocity:

$$-\frac{dv}{dt} = Fv^2 \tag{13}$$

where F is the constant part of the drag force equation divided by the bedload particle mass ($F = [0.5\rho\pi(d_s/2)^2 C_d]/ m$). In separated form, equation (13) becomes

$$-\frac{dv}{v^2} = Fdt. \tag{14}$$

Integrating both sides of equation (14) and solving for wall-normal particle velocity as a function of time since deflection gives [Wolfram|Alpha, 2010],

$$v(t) = \frac{1}{Ft + \frac{1}{v_r} - Ft_o} \tag{15}$$

where $1/v_r - Ft_o$ is the constant of integration, v_r is the initial wall-normal velocity following deflection, t_o is the time of the deflection event (set equal to zero in our model) and t is the time passed since the deflection event.

3.2.5. Impact Velocity and Erosion per Particle Impact

Equation (15) gives a wall-normal particle velocity as a function of time and initial wall-normal velocity following deflection. An expression for wall-normal particle velocity as a function of distance traveled is desirable since the lateral distance between an effective roughness element and the channel wall can be measured in the field. Setting t_o equal to zero (indicating the instant of collision), equation (15) is integrated with respect to time to yield an expression for lateral distance traveled by a deflected particle (y) as a function of time

$$y(t) = \int \frac{1}{Ft + \frac{1}{v_r}}\, dt = \frac{\ln(Fv_r t + 1)}{F}. \tag{16}$$

Solving equation (16) for time gives an expression for time since deflection as a function of lateral distance traveled since deflection (y)

$$t(y) = \frac{e^{(Fy)} - 1}{Fv_r}. \tag{17}$$

Equation (17) can then be substituted into the equation for particle velocity (equation (15)) to allow the velocity on impact to be expressed as a function of deflection distance from the wall and the initial wall-normal rebound velocity

$$v_i = \frac{1}{F\left(\frac{e^{Fy}-1}{Fv_r}\right)+\frac{1}{v_r}}. \quad (18)$$

Rearrangement of the terms in equation (18) results in a simplified equation for wall-normal impact velocity as a function of the distance of the deflection event from the wall (y) and the initial wall-normal velocity immediately following deflection (v_r):

$$v_i = v_r e^{-Fy} \quad (19)$$

Using this simplified expression for wall-normal impact velocity (v_i) the model is able to estimate the volume of wall material removed per particle impact. Following the work of Sklar and Dietrich [2004], the volume eroded per particle impact is scaled with the wall-normal component of kinetic energy on impact. Assuming the bedload particle mass remains constant, the volume eroded per particle impact (ε) is scaled with the square of wall-normal impact velocity (v_i) using the equation developed by Sklar and Dietrich [2004]:

$$\varepsilon = \frac{\pi \rho_s d_s^3 v_i^2 \mathscr{y}}{6 b_r \sigma_T^2}. \quad (20)$$

In the equation above, $\mathscr{y}$ is Young's modulus of elasticity for the bedrock (set equal to 5.0 x 10^4 MPa)in our model), b_r is a dimensionless bedrock strength coefficient (set equal to 1.0 x 10^{12} in our model) and σ_T is the bedrock tensile strength (set equal to 4.0 x 10^{-4} MPa in our model). The values for these three material property parameters are based on the work of Sklar and Dietrich [2004]. Equation (20) differs from the original equation of Sklar and Dietrich [2004] only in the use of wall-normal impact velocity (v_i) in place of bed-normal particle velocity.

The model uses a value for bedrock tensile strength (σ_T = 0.0002 MPa) that is roughly two orders of magnitude less than the weakest bedrock material tested by Sklar and Dietrich [2001]. This value was chosen because it provides the best

erosion-rate match between the model and the physical experiments for large roughness element sizes when bulk erosion rates appear to stabilize. The values of σ_T measured by Sklar and Dietrich [2001] range from ~25 MPa for a sample of andesite down to a value of 0.09 MPa for a sample of natural sandstone. The value for σ_T in the model is only approximate but reflects the assumed difference in strength between the analog bedrock material used in the set of physical experiments and the analog material tested by Sklar and Dietrich [2001]. The physical experiments were conducted with an analog material composed of a 90:1 ratio of sand to cement. The weakest analog bedrock material tested by Sklar and Dietrich [2001] was composed of a 20:1 ratio of sand to cement with a measured tensile strength of 0.15 MPa. The value of σ_T used in the model provides a good match in erosion rates when large roughness elements are on the bed and is consistent with the difference in composition between the analog material used in the physical experiments and analog materials tested by Sklar and Dietrich [2001].

3.2.6. Minimum Particle Impact Velocity and Maximum Distance Traveled

As formulated above, the volume of material eroded per impact assumes there is no kinetic energy threshold that must be overcome for detachment to occur. This implies that even sand-sized particles with minimal wall-normal velocity will cause erosion on impact. Studies of the erosion of brittle material by particle impacts have reached contrasting conclusions regarding the existence of an energy threshold for erosion. The abrasion mill experiments of Sklar and Dietrich [2001] indicate a negligible energy threshold in the context of channel bed erosion via sediment particle impacts. Other experiments using synthetic materials (i.e. glass) have shown that there is an energy threshold that must be exceeded for erosion to occur [Bitter, 1963]. Both of these studies consider the physical properties of the materials involved in the impact event (i.e. the resistance to erosion of a brittle bedrock surface) to be of primary importance in determining the existence of an energy threshold required for erosion.

We suggest that the collision dynamics of the impact event can be used to qualitatively distinguish between particle impacts that cause erosion and those that

do not. In particular, the distinction between a partially-elastic collision and a viscously-damped collision provides an intuitive criterion for evaluating the effectiveness of a particle impact (a similar method was used by Lamb et al. [2008] to describe erosion caused by suspended sediment particles). A series of laboratory experiments designed to investigate particle collisions in water showed that a particle collision Stokes number of 105 identifies the transition between a partially-elastic collision and a viscously-damped collision [Schmeeckle et al., 2001]. Using this transitional value of the particle Stokes number to distinguish between impacts that cause erosion and impacts that do not, we estimate the minimum wall-normal impact velocity required for erosion (v_{min}) by rearrangement of the particle Stokes number equation [Schmeeckle et al., 2001]:

$$v_{min} = \frac{(6\pi\mu\ (d_s/2)^2 S_t)}{m} \tag{21}$$

where μ is the dynamic viscosity of water, S_t is the particle Stokes number (set to a value of 105) and m is the mass of the bedload particle.

We use the minimum wall-normal velocity calculated above to establish a maximum distance from the wall at which a bedload particle can be deflected and still cause erosion on impact (Y_{max} in Figure 3.2). Setting the left side of equation (15) equal to the minimum impact velocity required for erosion (v_{min}), we solve for the maximum amount of time (t_{max}) between a particle deflection and an eroding particle impact.

$$t_{max} = \frac{v_r - v_{min}}{F\ v_r\ v_{min}} \tag{22}$$

The maximum distance from which a particle can be deflected and still cause erosion (Y_{max}) is found by solving equation (16) for distance traveled at time t_{max}.

$$Y_{max} = \frac{\ln(F\ v_r\ t_{max} + 1)}{F} \quad (23)$$

Depending on the height above the bed at which a collision takes place, as well as the bed-normal component of particle rebound velocity, a particle deflected from Y_{max} distance may fall back to the channel bed before impacting the wall. Particles that return to the bed prior to impacting the wall are treated as a special case in the model (referred to as 'bouncing' particles). If it is determined that a deflected particle will return to the bed prior to impacting the wall, the same reflection methodology that was used to determine the initial rebound velocity vector (equations (10) and (11)) is used to determine the 'bouncing' velocity vector of the particle. The wall-normal component of this bouncing velocity vector is then used to track the wall-normal particle velocity of the bouncing particle until it impacts the channel wall (unless the particle is intercepted by an adjacent roughness element as discussed below).

When considering a bouncing particle, the model applies a simple 'blocking' function to address the possibility that a bouncing particle will collide with an adjacent fixed roughness element as it rebounds from the bed. This interception of a bouncing particle by an adjacent roughness element will significantly reduce or eliminate the lateral momentum that the bouncing particle acquired during the initial deflection. The blocking function works on the premise that roughness elements which protrude higher above the bed have a greater possibility of intercepting a bouncing particle as it rebounds off a plane bed surface. Specifically, the model compares the maximum 'bounce' height of a bouncing particle with the mean protrusion height of the roughness elements (K_p) in a given channel reach. If the maximum bounce height is less than half the roughness element protrusion height ($H_{bounce} < 0.5K_p$) the bouncing particle is intercepted and does not impact the wall. An exception to this blocking criteria is made for the roughness element nearest to the wall. All particles deflected by the element nearest to the wall are allowed to impact the wall.

The treatment of bouncing particles requires an evaluation of the bed-normal forces, in addition to the wall-normal forces, acting on a particle. A force balance approach, similar to that described for wall-normal forces, is implemented to track the bed-normal velocity of a deflected particle (see the following section for a description

of this bed-normal force balance approach). We believe the treatment of bouncing particles is important because it allows for particles that are deflected very near the bed, but with significant wall-normal velocity, to contribute to the erosion of the channel wall.

3.2.7. Particle Impact Elevation

In addition to predicting the magnitude of lateral erosion via particle impacts for a given set of roughness, transport and bedload supply conditions, the ability to predict the vertical distribution of this erosion is essential to understand how a channel responds to this particular mechanism of lateral erosion. To determine the vertical distribution of lateral erosion, and to account for the special case of bouncing particles noted above, the model performs a separate analysis of the bed-normal forces acting on a deflected particle from the time of collision with a roughness element to the time of wall impact. The impact elevation of a deflected particle depends on the distance from the wall and the height above the bed at which a deflection event occurs (i.e. grid locations in Figure 3.2). Similar to our treatment of wall-normal forces acting on a particle, we use a force balance approach to track bed-normal particle velocity following a deflection event. However, in the case of bed-normal forces acting on a particle, we incorporate acceleration due to gravity as well as fluid drag into the initial force balance equation.

Assuming turbulent fluid acceleration in the bed-normal direction is negligible relative to the bed-normal forces of gravity and fluid drag, we relate the change in the bed-normal component of particle velocity to the drag and gravity forces acting on the particle with the following two equations:

$$-\frac{dw}{dt} = G + Fw^2 \tag{24}$$

$$-\frac{dw}{dt} = G - Fw^2 \tag{25}$$

where G accounts for the force of gravity on a particle submerged in water (defined previously in equation (7)), F is the constant part of the drag force equation divided by the bedload particle mass ($F = [0.5\rho\pi(d_s/2)^2 C_d]/\, m$) and w is the instantaneous bed-normal component of the particle rebound vector ($\boldsymbol{r}$). In the case of a particle that has positive upward velocity following a collision event, both gravity and fluid drag are working to stop the upward momentum of the particle. This case is represented by equation (24) above where downward acceleration ($-dw/dt$) is equal to the gravity force plus the drag force acting on the particle. After a particle loses its upward velocity, or in the case of a particle that never had upward velocity following a deflection, equation (25) is used to evaluate the change in bed-normal velocity during the descending portion of the particle's flight. In this case, gravity is working to accelerate the particle toward the bed but the drag force works to arrest the downward acceleration of the particle. In some cases, the trajectory of the deflected particle may include an intermediate collision with the channel bed prior to wall impact. Evaluation of bed-normal forces through time using equations (24) and (25) allows the model to explicitly treat this type of intermediate collision and ultimately allows the model to predict the elevation at which a 'bouncing' particle impacts the channel wall.

Equations (24) and (25) above are numerically integrated to solve for bed-normal particle velocity as a function of time since deflection. A second numerical integration is performed to determine the vertical position of the deflected particle through time. In the case of a deflected particle with initial upward velocity, equation (24) is numerically integrated until the upward bed-normal velocity goes to zero. If the particle has not reached the wall by the time the upward momentum goes to zero, the model switches to a numerical integration of equation (25) to solve for particle velocity and vertical position during the falling portion of the trajectory.

3.2.8. Rate of Laterally-Effective Collisions

Criteria for Laterally-Effective Collisions

We develop a set of geometric criteria to evaluate the potential for laterally-effective collisions in a channel reach with given bed roughness characteristics. The geometric criteria are based on bedload particle size (d_s), roughness-element

protrusion height (K_p) and the distance between the centers of adjacent roughness elements (λ) (Figure 3.3). Given our treatment of roughness elements (K) as hemispheres protruding from a planar bed, the protrusion height (K_p) is set equal to the radius of the roughness element.

For a bedload particle that is circular in cross section, we define a vertical length scale (d_v) that represents the minimum vertical distance above the base of a bedload particle at which contact with a roughness element must occur in order to generate a laterally-effective deflection (Figure 3.3). This length scale is used to determine if the protrusion height of a roughness element relative to the bedload particle size is sufficient to generate a laterally-effective collision (Figure 3.3a – sufficient protrusion height ($K_p > d_v$)). If the protrusion height is less than the vertical length scale of the bedload particle ($K_p < d_v$), laterally-effective collisions do not occur (Figure 3.3c – insufficient protrusion height). This criterion is relevant in reaches where 'roughness-element' protrusion is minimal. The criterion is based on the set of physical experiments that indicate laterally-effective collisions do not occur in sections where roughness elements are smaller than ~0.5 times the bedload particle diameter. The vertical bedload length scale is calculated as follows:

$$d_v = (d_s/2) - \cos(\alpha)(d_s/2), \tag{26}$$

where α is the angle from vertical at which a line of radius is drawn from the particle center to the particle surface (Figure 3.3a). The height above the base of the particle at which this line of radius intersects the particle surface defines the vertical bedload length scale. We use a value of $\pi/6$ for α based on empirical evidence from the set of physical experiments in the previous chapter.

Next, we define horizontal length scales for both bedload particle (d_h) and bed roughness element (K_y) to determine if there is sufficient free space between roughness elements to allow a saltating bedload particle to strike a high-angle deflection surface (Figure 3.3b and 3.3d). All else equal, a decrease in free space relative to bedload particle diameter will reduce the ability of a bedload particle to

strike a high-angle deflection surface located near the base of the roughness element (Figure 3.3d).

The horizontal bedload length scale is defined as the cross-section width of the bedload particle at height d_v above the base of the particle (Figure 3.3d)

$$d_h = [\sin(\alpha)(d_s/2)] \times 2 \quad (27)$$

where α is assigned a value of $\pi/6$ based on empirical observations as discussed previously. The horizontal roughness-element length scale (K_y) is defined as the cross-section width of the roughness element at vertical distance d_v below the top of the roughness element (Figure 3.3b).

$$K_y = 2 \times \sqrt{(K/2)^2 - (K/2 - d_v)^2} \quad (28)$$

where K is the diameter of the roughness element. We can then calculate the free space between roughness elements at height $K_p - d_v$ above the bed using the following relation:

$$\lambda_{(K_p - d_v)} = \lambda - K_y \quad (29)$$

A comparison between the horizontal bedload length scale (d_h) and the free space between roughness elements at a height just below the top of the roughness element ($\lambda_{(K_p\text{-}d_v)}$) predicts the ability of a bedload particle to strike a high-angle deflection surface (Figure 3.3b) and obtain significant lateral momentum from the collision. If the free space between roughness elements just below the tops of the elements is less than the horizontal bedload length scale ($\lambda_{(K_p\text{-}d_v)} < d_h$), bedload particles will be unable to strike a high-angle deflection surface (Figure 3.3d). In this scenario, the momentum transferred from one saltation hop to the next will be primarily vertical in direction.

For effective particle deflections to occur, both criteria described above must be satisfied. That is, the roughness-element protrusion height must be greater than the vertical bedload length scale ($K_p > d_v$) and the free space between roughness elements at height $K_p - d_v$ must be greater than the horizontal bedload length scale ($\lambda_{(K_p-d_v)} > d_h$).

Likelihood of a Laterally-Effective Collision

The presence of effective deflection surfaces is not continuous across the entire width of a channel cross section. Depending on the mean free space between roughness elements, only a portion of each channel cross section will contain effective deflection surfaces (Figure 3.4). The presence of deflection surfaces will vary horizontally across the channel as well as vertically with height above the channel bed. Cross-channel variability is explained by the free space between roughness elements and the diameter of individual roughness elements. Variability with height above the bed can be explained by the geometry of the roughness elements. In the case of a 2-D cross-section with roughness elements represented by hemispheres protruding from a flat bed, the percent of the cross-section width occupied by deflection surfaces will decrease with height above the bed (Figure 3.4). In order to estimate the likelihood that a particle will be deflected, we develop a metric that describes the fraction of cross-section width occupied by effective deflection surfaces as a function of height above the bed. This metric is distinct from the criteria developed previously that determine if an effective deflection is even possible.

The fractional width occupied by roughness elements (W_k) is calculated as the ratio of roughness-element width at a given elevation above the bed ($K_y(z)$) to the total distance between centers of adjacent roughness elements (λ) (Figure 3.4). We account for the cross-sectional length occupied by a bedload particle by adding the horizontal bedload length scale (d_h) to the cross-section length of the roughness element at a given elevation

$$W_k(z) = \frac{\left(K_y(z) + d_h\right)}{(\lambda)}. \quad (30)$$

In the case of relatively large bedload particles with minimal free space between roughness elements, equation (30) could take on values greater than unity. In this case however, the previously defined criteria ($\lambda_{(K_p-d_v)} < d_h$ and $K_p < d_v$) used to determine if effective deflections are even possible would eliminate deflections from consideration.

Lateral and Vertical Distribution of Bedload Particles

For a given flux of saltating bedload particles, the rate of laterally-effective collisions depends on the lateral distribution of particles across the width of the channel as well as the vertical distribution of particles relative to the availability of effective deflection surfaces with height above the bed. To simplify the model, we have assumed a uniform distribution of particles in the cross-channel direction. In bedrock channels with pronounced channel thalwegs, a uniform lateral distribution of bedload particles is unlikely. However, for a simplified rectangular geometry for which this model is developed, a uniform lateral distribution of bedload particles is not unreasonable.

For a given sediment supply rate in units of mass per time (Q_s [*g/s*]), we calculate the total particle supply rate (Q_p) as

$$Q_p = \frac{Q_s}{m}. \quad (31)$$

Assuming a uniform lateral distribution of particles, we calculate the particle flux per unit width (q_p) and the particle flux within Y_{max} distance of the wall (Q_{Ymax}) as

$$q_p = \frac{Q_p}{B} \quad (32)$$

$$Q_{Ymax} = q_p Y_{max} \quad (33)$$

There are limited data describing the vertical distribution of saltating bedload particles within a cross section. We follow the lead of previous bedrock incision models [Lamb et al., 2008] and invoke a uniform vertical distribution of saltating bedload particles. For model runs that consider multiple roughness-element deflectors, the model uses Q_{Ymax} as calculated here. For model runs that only consider a single roughness-element deflector, we replace Y_{max} in equation (33) above with the radius of the single roughness element. For single-element model runs, this gives us the particle flux that is intercepted by the radius of a single roughness element.

Rate of Effective Collisions with Height above the Bed

The rate of effective particle deflections at a given elevation above the bed ($I_{(z)}$) is calculated as the number of particles transported within the elevation interval multiplied by the fractional width of that elevation interval that is occupied by roughness-element surfaces ($W_{k(z)}$). The key thing to remember here is that the cross-sectional width occupied by a roughness element changes with height above the bed such that the cross-sectional width near the top of the roughness element is minimal compared to the full width at the base of the element.

$$I_{Ymax(z)} = Q_{Ymax}(z) \times W_k(z) \quad (34)$$

Our representation of channel bed roughness as the protrusion of spherical roughness elements above a planar bed results in the rate of bedload particle deflections decreasing with height above the channel bed (Figure 3.2).

3.2.9. Calculation of Bulk Lateral Erosion Rates

Numerical Methods

Given the dependence of volume eroded per impact on distance from the wall of a deflection event and the dependence of particle impact rate on parameters that

vary with height above the bed, a two-dimensional cross-section model is required to adequately predict erosion via deflected bedload particles. We establish a *y*-*z* grid in the vertical plane of the channel cross section with the *y*-axis representing the distance from the channel wall and the *z*-axis representing height above the median bed elevation (Figure 3.2). The *z*-interval of the grid (Δz) is set equal to the vertical length scale of the bedload particle and the *y*-interval of the grid (Δy) is set equal to the horizontal length scale of the bedload particle. The model performs the calculations described in the sub-headings above for each potential collision location within a cross section as defined by a *y*-*z* cross-sectional grid. The height and width of the grid is determined by the bedload particle transport parameters. The model assumes that the given flux of bedload particles is distributed uniformly within the cross-sectional grid such that each potential collision location has an equal probability of being struck by a saltating bedload particle.

Erosion per particle impact (ε_y) is calculated for each Δy increment between the wall and Y_{max} using the procedure described above (the addition of the '*y*' subscript reflects the dependence of ε on distance from the wall of a deflection event). This calculation results in a regularly-spaced series of erosion per impact volumes that are oriented along the *y*-axis of the cross-section and that decrease with distance from the wall (Figure 3.2). Since the volume eroded does not depend on the height of a deflection event above the bed, this series of erosion per impact volumes applies to particles deflected at any height above the bed.

Our assumption of a uniform lateral distribution of bedload particles allows us to calculate the rate of effective particle deflections per unit width for a specific elevation (I_z),

$$I_z = \frac{I_{Ymax(z)}}{(Y_{max}/\Delta y)} \tag{35}$$

where the subscript '*z*' indicates the elevation above the bed at which the rate of deflections per unit width is calculated. This results in a regularly-spaced series of unit width deflection rates oriented along the *z*-axis. The deflection rate per unit width decreases with height above the bed due to a decrease in the availability of effective

deflection surfaces with height above the bed (Figure 3.2). Depending on the model grid size and the particle flux rate, the calculation of I_z, which represents the deflection rate within a single *y*-*z* grid cell, can result in a fractional particle deflection rate for a given *y*-*z* location. This fine-scale discretization of the cross-section width is necessary to capture the 'true' variability of particle impact velocities that exist for particles deflected from different distances between the wall and Y_{max} distance. The number of deflections per time is used in combination with the particle impact velocity and elevation estimates for each potential collision location to calculate the bulk lateral erosion rate associated with a flux of bedload particles through a cross section with specific bed roughness parameters.

3.2.10. Composite Expression for Lateral Erosion

Here we present a composite expression for lateral bedrock erosion via bedload particle impacts. The initial equation for bulk lateral erosion rate (equation (1)) is modified for use in a two-dimensional framework to predict rates of lateral erosion at a particular elevation above the bed. The model assumes there is a one-to-one relationship between deflection location and the elevation of particle impact such that all particles deflected from a specific *y*-*z* location will impact the wall at a single elevation (Z_w). Thus, for a fixed set of transport conditions, the rate of material eroded at a particular elevation on the wall (E_{Zw}) depends on: 1) the number of deflection locations that produce particle impacts at the particular wall elevation; 2) the distance from the wall of each of these deflection locations; 3) the deflection rate associated with each deflection location in the set.

$$E_{Zw} = \sum_{Zw \in h} \left(\varepsilon_y I_z\right)_{Zw} \tag{36}$$

The equation above expresses the rate of wall erosion at a particular elevation (Z_w) as a sum of the product of erosion per impact (ε_y) and impact rate (I_z) for all deflection locations associated with a wall impact elevation equal to Z_w (where *h* is the set of all possible wall impact elevations). The number of deflection locations

associated with a specific wall impact elevation will change if there are changes in transport stage, bedload particle size or bed roughness characteristics.

Substituting the expressions developed earlier for erosion per impact (equation (20)) and impact rate (equation (35)) into the equation above produces a composite expression for lateral wall erosion rate via bedload impact at a particular elevation on the wall.

$$E_{Zw} = \sum_{Zw \in h} \left[\left(\frac{\pi \rho_s d_s^3 V_i^2 \mathcal{Y}}{6 b_r \sigma_T^2} \right)_y \left(\frac{Q_{Ymax(z)} W_{k(z)}}{Y_{max}/\Delta y} \right)_z \right]_{Zw} \quad (37)$$

3.2.11. Assessment of Model Performance

To examine the ability of the model to reasonably predict the magnitude and vertical distribution of lateral wall erosion for a given set of channel conditions, the input parameters and measured flow conditions from the set of physical experiments (CH. 2) are used as inputs to the model (Table 3.1). Individual model runs are conducted using the unique set of conditions that are specific to a distinct roughness section from the physical experiment. Model runs are conducted only for roughness sections that displayed significant lateral erosion during the set of physical experiments (a total of five distinct roughness-element sizes). Model runs were not conducted using parameters from sections where roughness elements were smaller than 2.4 mm because those sections do not meet the minimum protrusion height criteria. In contrast to the physical experiments, the model does not account for real time changes in channel width due to lateral erosion. This limitation of the model minimizes the distance between roughness elements and the channel wall over time and maintains the same bedload particle concentration during the entire model run. By not accounting for real-time changes in channel width, the model has the potential to overestimate rates of lateral erosion.

We conduct two types of model runs for each distinct roughness-element size: runs that consider bedload particle deflection from a single roughness element located near the wall and runs that consider bedload particle deflections from

multiple roughness elements spread laterally across a given channel cross section. For model runs that consider deflections from multiple roughness elements spread across the channel cross section, the model accounts for the mean free space between roughness elements based on the observed free space in the set of physical experiments. In the case of the single-element model, the bedload particle flux intercepted by the cross section of the roughness element varies substantially with the size of the roughness element. In this sense, the comparison of bulk erosion rates between single element model runs with different roughness element size does not necessarily reflect the influence of element size on wall erosion rates. For single element model runs, the model calculates the flux of bedload particles that will interact with the single roughness element at a given elevation ($Q_{K(z)} = q_{p(z)} * K_{(z)}$) by taking the particle supply per unit width at a given elevation interval ($q_{p(z)}$) and multiplying it by the cross-sectional length of the roughness element ($K_{(z)}$) at the particular elevation interval.

In order to calculate the hydraulic and bedload transport conditions using the observed experimental parameters, the model assumes a laterally-uniform flow and laterally uniform distribution of bedload particles. The model uses the laterally-uniform flow assumption to calculate cross-section average bedload particle saltation characteristics (i.e. downstream saltation velocity and saltation hop height). These cross-section characteristics are used to describe bedload particle transport across the entire width of the cross section. In all model runs, we apply the lateral erosion model to a single channel wall within a single cross section to predict the volume of material eroded by bed load particle impacts. As discussed below, the model indicates that the majority of impact erosion comes from particles that are deflected by roughness elements located within a few bedload particle diameters of the wall.

3.3. RESULTS

3.3.1. Hydraulic and Bedload Transport Conditions

Model results indicate that the shear stress available for bedload transport (τ_{bs}) is greatest in sections with smaller roughness elements (2.4, 4.7 and 7.0 mm sections) and is at a minimum in the run with the largest roughness element (16 mm). This result

demonstrates the effect of increased form drag (τ_{bf}) on the transport capacity of the channel (Table 3.1). While total boundary shear stress (τ_b) is greatest in the 16 mm model run, form drag associated with the relatively large roughness elements significantly reduces the ability of the channel to transport bedload material ($\tau_{bs} = \tau_b - \tau_{bf}$).

These initial hydraulic and bedload transport calculations provide the input for the deflection component of the model. The specific bedload transport parameter that gets passed to the deflection component of the model is the mean downstream saltation velocity of the bedload particle (u_s). Calculations using the input parameters from the set of physical experiments show that bedload particles in the section with 4.7 mm roughness elements have the greatest downstream saltation velocity. Since the size of the bedload particle is the same for all model runs, the momentum of a saltating bedload particle just prior to deflection is greatest in the model run with 4.7 mm roughness elements and least in the run with 16 mm elements. This translates to maximum bedload particle momentum following a deflection event for the 4.7 mm model run and limited bedload particle momentum following a deflection event in the 16 mm model run.

3.3.2. Bulk Wall Erosion due to a Single Roughness Element

Influence of Roughness-Element Size and Distance from Channel Wall

We used the model developed above to investigate the influence of roughness-element size and roughness-element distance from the channel wall on bulk rates of lateral wall erosion under conditions of constant discharge and constant sediment supply per unit width. We focused initially on a series of single element model runs to present the simplest case of lateral erosion via deflected bedload particles. For each distinct roughness-element size, we conducted a series of model runs in which we vary the distance between the single roughness element and the channel wall. The results from this series of single element model runs are plotted in Figure 3.5.

Each series of data points in Figure 3.5 represents the bulk erosion caused by a single roughness element of a given size that has been positioned at different distances from the wall. Looking at the first data point in each series (representing a distance of one bedload particle diameter away from the wall) it is easy to see the influence of greater cross-sectional width and height associated with the larger roughness elements

(i.e. the bulk erosion rate for the 16 mm element at a distance of one bedload particle from the wall is much greater than the bulk erosion rate for the 2.4 mm element located at the same distance from the wall). Perhaps more interesting is the difference in the rate at which the bulk erosion rate decays as an element of given size is moved further away from the wall (the lines in Figure 3.5 are exponential fits to each data series). Note that at a distance of two bedload particle diameters away from the wall, the bulk erosion rate associated with the largest roughness element has decreased to zero while the bulk erosion rate associated with smaller roughness elements is still measurable (Figure 3.5). In fact, at a distance of three bedload particle diameters away from the wall, the second smallest roughness element (4.7 mm diameter element) has the highest bulk erosion rate. The rapid decrease in bulk erosion rate as a function of distance in the 16 mm model run is indicative of a trade-off between larger deflection surface area and increased form drag. This trade-off is important in determining rates of lateral erosion via bedload particle deflections.

3.3.3. Wall Erosion Profile due to a Single Roughness Element

Influence of Roughness Element Size and Distance from the Channel Wall

From the same series of single-element model runs in which we vary the distance from the wall of an element of given size, we plot the vertical distribution of wall erosion as a function of the distance from the wall of the element that produced the profile (Figure 3.6 (a-e)). As we saw in the set of physical experiments, the most prominent feature of these wall erosion profiles is the concentration of erosion near the base of the channel wall. The concentration of wall erosion at or near the elevation of the channel bed produces bedrock channel banks that are undercut. The undercut bedrock channel morphology that we see in the model is similar to that found along parts of the Kettle River near Sandstone, MN where the channel is incised into a weak sandstone layer (Figure 3.7).

The undercut wall erosion profile is maintained (although less pronounced) as the distance of the roughness element from the channel wall increases from one bedload particle diameter (Figure 3.6 - blue profile) to three bedload particle diameters (Figure 3.6 - red profile). This suggests that the inclusion of multiple roughness elements at

various distances from the wall into the model would not significantly change the shape of the wall erosion profile.

3.3.4. Bulk Wall Erosion due to Multiple Roughness Elements

Influence of Roughness Element Size

Rates of bulk lateral erosion predicted by model runs that incorporate deflections from multiple roughness elements are similar for all roughness-element sizes except for the smallest element for which the model was run (Figure 3.8) The similarity in bulk erosion rates between roughness elements of different size that we find when incorporating multiple deflectors is in contrast to the significant variability in bulk erosion rates between roughness elements of different size that we find when considering deflections from a single roughness element (Figure 3.5). Multiple element model runs are likely more similar to conditions found in nature as well as to the conditions found in the set of physical experiment described in chapter 2. Bulk erosion rates from model runs with multiple roughness elements shown in Figure 3.8 indicate that bulk erosion rates are maximized when the size of the roughness element is equal to the size of the bedload particle (4.7 mm in the model scenarios presented here). Bulk erosion rates appear to be minimized when the size of the roughness element on the bed (2.4 mm) is significantly less than the bedload particle size (4.7 mm). After reaching a maximum value when the roughness element on the bed is equal in size to the bedload particle, bulk erosion rates decline slightly and then stabilize as the size of the roughness element on the bed continues to increase.

Comparison between Multiple Element Model Results and Experimental Results

A comparison of bulk erosion rates from multiple element model runs and bulk erosion rates from the set of physical experiments conducted in chapter 2 shows a similar erosion rate trend associated with changes in the size of the roughness element on the bed (Figure 3.9). The biggest discrepancy between the model and experimental bulk erosion rates is found at the smaller end of the roughness-element size range (2.4 mm and 4.7 mm roughness elements) where the experimental results are two to three times greater than the model results. The other observation of note in the comparison between model and experimental results is the change from elevated experimental

erosion rates in cases of smaller roughness elements to model erosion rates being slightly above the experimental rates in the case of larger roughness elements. We explore potential drivers of this change in relative erosion rates in the following section. We note that the elevated experimental erosion rates in cases of smaller roughness elements is at odds with our assumption that model erosion rates should be artificially high due to the lack of real time adjustment of channel width in the model.

3.3.5. Wall Erosion Profile due to Multiple Roughness Elements

The multiple-element model provides the best opportunity to compare the wall erosion profiles predicted by the model to those produced by the complimentary set of physical experiments. The comparisons in Figure 3.10 show that the multiple-element model is capable of reproducing the general undercut morphology observed in the physical experiments where lateral erosion is greatest near the bed and tapers off with increasing elevation above the bed. There are however significant differences between the profiles produced by the model and those produced by the experiment.

As observed in the comparison of bulk erosion rates above, the wall erosion profiles from channel sections with smaller roughness elements (Figures 3.10(a) and 3.10(b)) shows that the model under-predicts the total amount of wall erosion. Another prominent difference between the model and experimental results is that the vertical distribution of erosion predicted by the model is weighted more heavily toward the base of the wall than it is in the experimental profiles. Looking at the erosion profiles from the sections with 10 mm and 16 mm roughness elements (Figures 3.10(d) and 3.10(e)), it is readily apparent that the model predicts a greater width of lateral incision (the lateral distance of maximum erosion) close to the bed while predicting minimal erosion at elevations greater than 5 mm above the bed. In all of the roughness element sections, the model under-predicts the maximum height of wall erosion by at least a factor of 2 and by as much as a factor of ~4.5. In the case of the 7 mm roughness element section (Figure 3.10(c)), the model predicts a maximum erosion height of roughly 10 mm above the bed while the experiment shows a maximum erosion height of roughly 22 mm above the bed.

3.4. DISCUSSION

The model results reported here corroborate several of the important conclusions drawn from the experimental study. In general, the ability of the model to reproduce many of the experimentally observed erosion characteristics and relationships between bed roughness and erosion rates supports the idea that the deflection of bedload particles all is a viable mechanism of lateral bedrock erosion. The ability of the model to reproduce the observed erosion morphology (i.e. undercut banks) and trends in bulk erosion rates suggest that the model adequately represents the transport, deflection and impact processes of the proposed erosion mechanism.

The model captures the fundamental trade-off between an increase in deflection surface area (i.e. larger roughness elements) and an increase in form drag that seems to be a first order control on how rates of lateral erosion vary with the size of the roughness element on the bed. Analysis of bulk erosion rates from single roughness elements clearly demonstrates the ability of the model to predict this trade-off (Figure 3.5). When single roughness elements are located just 1 bedload particle diameter away from the channel wall (left side of Figure 3.5), the largest roughness element (16mm – red diamond) produces erosion rates that are roughly seven times greater than the erosion rate produced by the smallest roughness element (2.4 mm – black circle). In this case, deflection surface area exerts the strongest control on erosion rates because deflected particles have a short distance to travel to impact the wall and, therefore, do not require high wall-normal velocities following deflection to cause erosion. However, as the distance between the roughness element and channel wall increases, the bulk rate of lateral erosion decreases rapidly for the larger roughness elements. This rapid decrease in erosion rate demonstrates the influence of form drag on erosion rates. The relatively high form drag associated with large roughness elements leads to a relatively low particle saltation velocity prior to deflection. Low particle saltation velocity results in relatively low momentum upon collision with a roughness element and relatively low wall-normal rebound velocities. Because erosion per impact scales with the wall-normal impact velocity, lower wall-normal rebound velocities translate to lower erosion per impact. For large roughness elements located just 2 bedload particle diameters away from the wall, the effect of high form drag on particle rebound velocities begins to exert a strong control on erosion rates. In the section with 16 mm roughness elements, the effect of form drag is such that particles deflected by a roughness element located just 2

bedload particle diameters from the wall are unable to cause erosion (Figure 3.5). Meanwhile, in sections with smaller roughness elements (4.7 mm), form drag is minimal and particle saltation velocities are relatively high. These high saltation velocities allow particles deflected from small roughness elements located as far as 8 bedload particle diameters from the wall to cause erosion on impact.

The insight gained from the single element model (i.e. the trade-off between increased deflection surface area and increased form drag) is crucial to the interpretation of results from the multiple-element model. In general, the multiple-element model predicts many of the relationships between roughness element size and bulk erosion rates observed in the set of physical experiments. As roughness element size is gradually increased, both the model and experiment show a sharp increase in erosion rates followed by a stabilization of erosion rates (Figure 3.9). The multiple-element model shows a sharp increase in lateral erosion rates as 2.4 mm roughness elements are added to the bed and again as the roughness element size increases from 2.4 mm to 4.7 mm. While the increase in erosion rate caused by adding 2.4 mm elements to the bed is forced (because smaller roughness elements don't meet the protrusion height requirement and erosion rates are assumed to be zero for smaller sized elements), the spike in erosion rate caused by increasing roughness element size from 2.4 mm to 4.7 mm is completely organic. The spike in erosion rates from 60 $3m^3 hr^{-1}$ in the 2.4 mm section to 170 $mm^3 hr^{-1}$ in the 4.7 mm section represents a nearly three-fold increase in erosion rates. It is significant because it constitutes a change in erosion rates from well below the value at which erosion rates stabilize (i.e. erosion rates for the two largest roughness elements), up to rates that are greater than the value at which erosion rates stabilize. We take this erosion rate spike as evidence that the model is able to predict the existence of a roughness threshold that must be crossed in order to get rates of erosion that are similar to, or greater than, the value at which erosion rates stabilize. The existence of a minimum roughness threshold required for significant lateral erosion is one of the key observations to emerge from the set of physical experiments. These model results support the observation that a roughness threshold exists and suggests that we have adequately parameterized bed roughness and bedload particle deflections.

Based on the analysis above, the bed roughness required for significant lateral erosion is predicted by the model to occur at a slightly larger roughness element size

(4.7 mm) than it does in the set of physical experiments (2.4 mm section). The source of this disagreement may be small differences in the actual bed roughness conditions between the model and the physical experiments (i.e. protrusion height, areal concentration and free space between elements) that caused the model to under predict erosion rates in the 2.4 mm section. It is also possible that the model's assumption of a vertically-uniform distribution of bed load particles contributed to the model under predicting erosion in the 2.4 mm section. If the concentration of saltating bedload particles is in fact greater near the bed, the assumption of a vertically-uniform distribution would reduce the frequency of particle deflections and thus under predict erosion rates. There is limited research on the concentration profile of saltating bedload particles. A recent study indicates that the concentration of saltating bedload particles during vigorous transport is slightly greater near the bed [Capart and Fraccarollo, 2011]. The model presented here does not incorporate the concentration profile of Capart and Fraccarollo [2011] because the conditions under which their measurements were made (intense transport over a loose alluvial bed) are different than the mixed bedrock-alluvial conditions represented by this model. Instead, the model presented here follows the lead of an earlier numerical model of *vertical* bedrock erosion in which the authors invoke the assumption of a uniform vertical distribution of saltating bedload particles [Lamb et al., 2008].

In addition to predicting a minimum roughness threshold required for significant erosion, the model predicts a stabilization in erosion rates at large roughness element sizes, similar to the stabilization observed in the physical experiments. To compare the stabilization pattern between the model and the physical experiment we use a non-dimensional measure of roughness element size (K/d_s). Using this dimensionless ratio, the model predicts that erosion rates will stabilize when the roughness-element to bedload-particle size ratio approaches a value of ~1.5 (K/d_s = 1.5). In the physical experiments, erosion rates stabilize when the roughness-element to bedload-particle size ratio approaches a value of ~2 (K/d_s = 2.2). Despite predicting erosion rate stabilization at a slightly smaller roughness-element to bedload-particle size ratio, the model predicts a stabilized erosion rate that is very similar to the erosion rate at which stabilization occurs in the physical experiments (160 $mm^3 hr^{-1}$ vs. 135 $mm^3 hr^{-1}$ respectively). In both the model and the physical experiment, the erosion rate at which

stabilization occurs is less than the peak erosion rate (170 $mm^3 hr^{-1}$ in the model and 270 $mm^3 hr^{-1}$ in the experiment). Both the model and the physical experiments indicate that peak lateral erosion rates occur at a roughness-element to bedload-particle size ratio of unity.

As discussed above, the model is able to reproduce many of the key relationships between erosion rate and bed roughness that were observed in the physical experiments. However, the absolute magnitude of erosion rates predicted by the model are sometimes quite different than those measured in the physical experiments. This is particularly the case with smaller roughness elements (2.4 mm and 4.7 mm) where the model predicts bulk erosion rates that are roughly 1/3 to 1/2 of those measured in the physical experiment. This could be due to differences in the bed roughness characteristics between the model and the experiment in those sections. Inaccurate measurement of the bed roughness characteristics in these sections during the physical experiments could have resulted in inaccurate input values for the model. However, as the roughness elements increased in size in the physical experiments, our image-based analysis of bed roughness characteristics improved considerably. This allowed us to more accurately represent bed roughness conditions for the model and better predict the magnitude of erosion in sections with larger roughness elements.

Another key difference between the model and the physical experiments is the vertical distribution of wall erosion as seen in the comparison plots of wall erosion profiles (Figure 3.10). The concentration of erosion near the bed predicted by the model could be due to the static nature of the model in which the distance between a roughness element and the channel wall remains constant despite lateral wall erosion. The under-prediction by the model of the maximum height of erosion suggests that the model has not captured all the forces that determine the trajectory of a deflected or bouncing particle as it travels laterally toward the wall. The model assumes that the deflected or bouncing particle does not gain any additional momentum anywhere along the trajectory toward the wall. This is probably a good assumption in the case of deflected particles that impact the wall without bouncing. However, it seems possible that a bouncing particle will acquire additional vertical momentum as it bounces off the bed just as a saltating bedload particle acquires vertical momentum from lift forces that act on a particle near the bed surface [Wiberg and Smith, 1985]. Allowing for a bouncing

particle to gain vertical momentum upon impact with the bed could lead to particle impacts occurring higher above the bed.

3.5. CONCLUSIONS

The lateral bedrock erosion model developed here corroborates a previously developed hypothesis that states the impact of deflected bedload particles is an effective mechanism of lateral bedrock erosion. The model presented here conceptualizes the deflection mechanism of erosion and develops a set of equations to describe the path of an individual bedload particle as it moves downstream, collides with a roughness element on the bed, rebounds with significant lateral momentum and impacts the channel wall to cause erosion. Based on this single mechanism of erosion and input conditions that match those of a previous set of physical experiments, the model is capable of predicting the wall-erosion morphology and the relationship between roughness element size and rates of lateral erosion that were observed in the set of physical experiments.

The comparison of model results to experimental data suggests the model: 1) adequately represents the first order processes of this specific mechanism of lateral bedrock erosion including bedload transport conditions, particle collision and rebound and wall impact causing erosion; 2) captures the relationship between roughness element size and erosion rate including the trade-off between increased deflection surface area and increased form drag; 3) considers the appropriate bed roughness parameters when determining the frequency of particle deflections including protrusion height, areal concentration and mean free space between elements; and 4) successfully employs lateral and vertical force balance equations to predict the wall-normal velocity and height above the bed of a deflected particle upon impact with the wall.

Prior to the development of this model and the complimentary set of physical experiments, the geomorphic community had limited insight into the specific mechanisms of lateral bedrock erosion. The lack of information about a specific mechanism caused some in the community to assume that rates of lateral bedrock erosion changed very little over space and time (Hancock and Anderson, 2002) or that rates of lateral erosion scaled linearly with total boundary shear stress (Stark, 2006; Wobus et al., 2006). The model results presented here, combined with data from a set of

physical experiments, provide empirical evidence backed by theory that indicates rates of lateral erosion in bedrock channels are not constant. Instead, rates of lateral bedrock erosion appear to vary as a function of channel bed roughness and the likelihood of laterally-effective bedload particle deflections. The numerical model has also shown that rates of lateral bedrock erosion do not vary linearly with total boundary shear stress on the bed. Instead, a trade-off between an increase in deflection surface area and an increase in form drag associated with larger roughness elements seems to be a primary control on rates of lateral erosion via deflected bedload particle impacts.

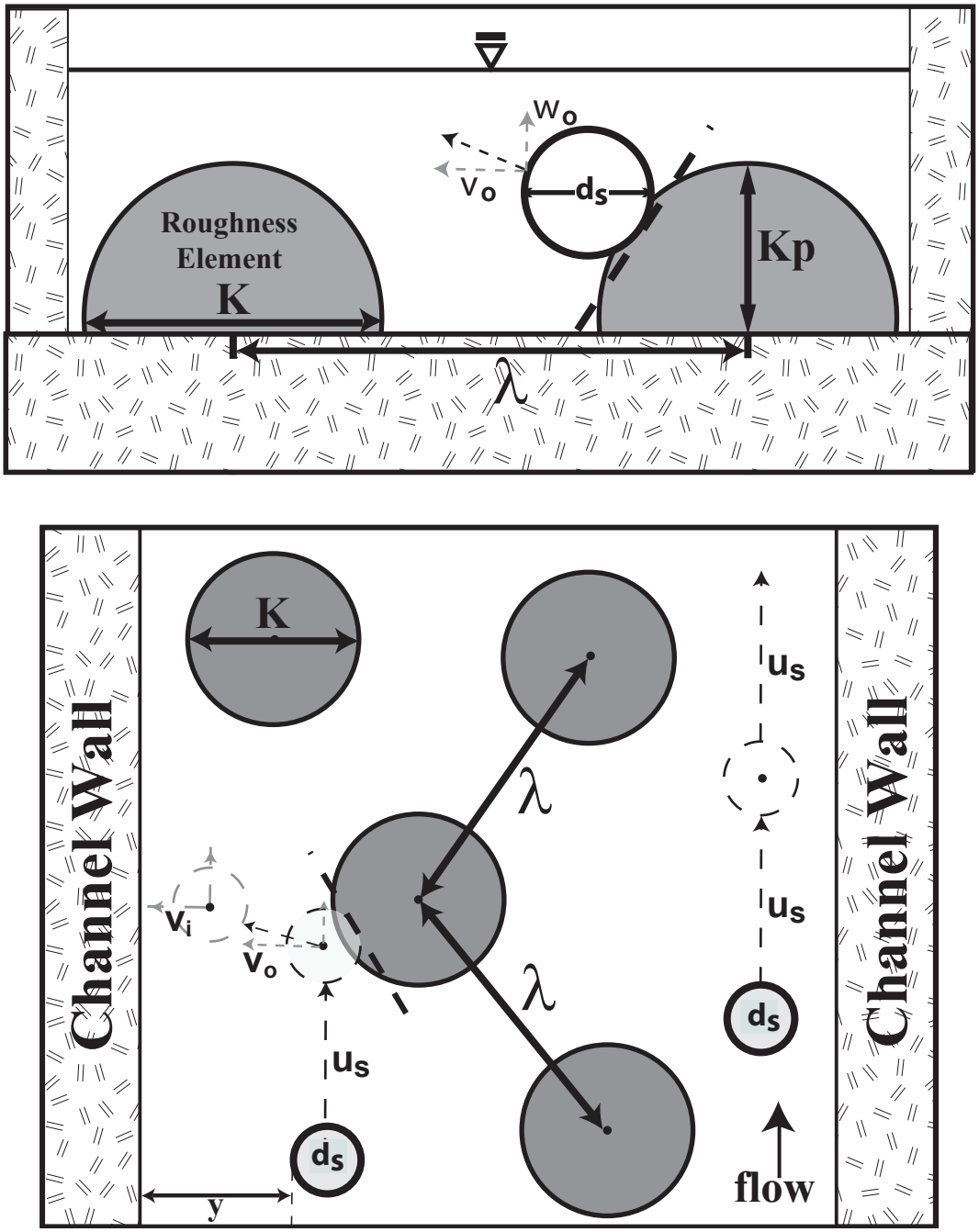

Figure 3.1 – (top) cross section and (bottom) plan view perspectives of collisions between bed load particles (d_s) and bed roughness elements (K). Bed load particles are treated as spheres and bed roughness elements are treated as hemispheres protruding from a planar bed. Protrusion height (K_p) is equivalent to the radius of the roughness element. Dashed lines represent incoming (u_s) and deflected particle velocity components (V_o=initial; V_i=impact). λ is mean free space between roughness element centers, y is the distance from the channel wall of a collision event.

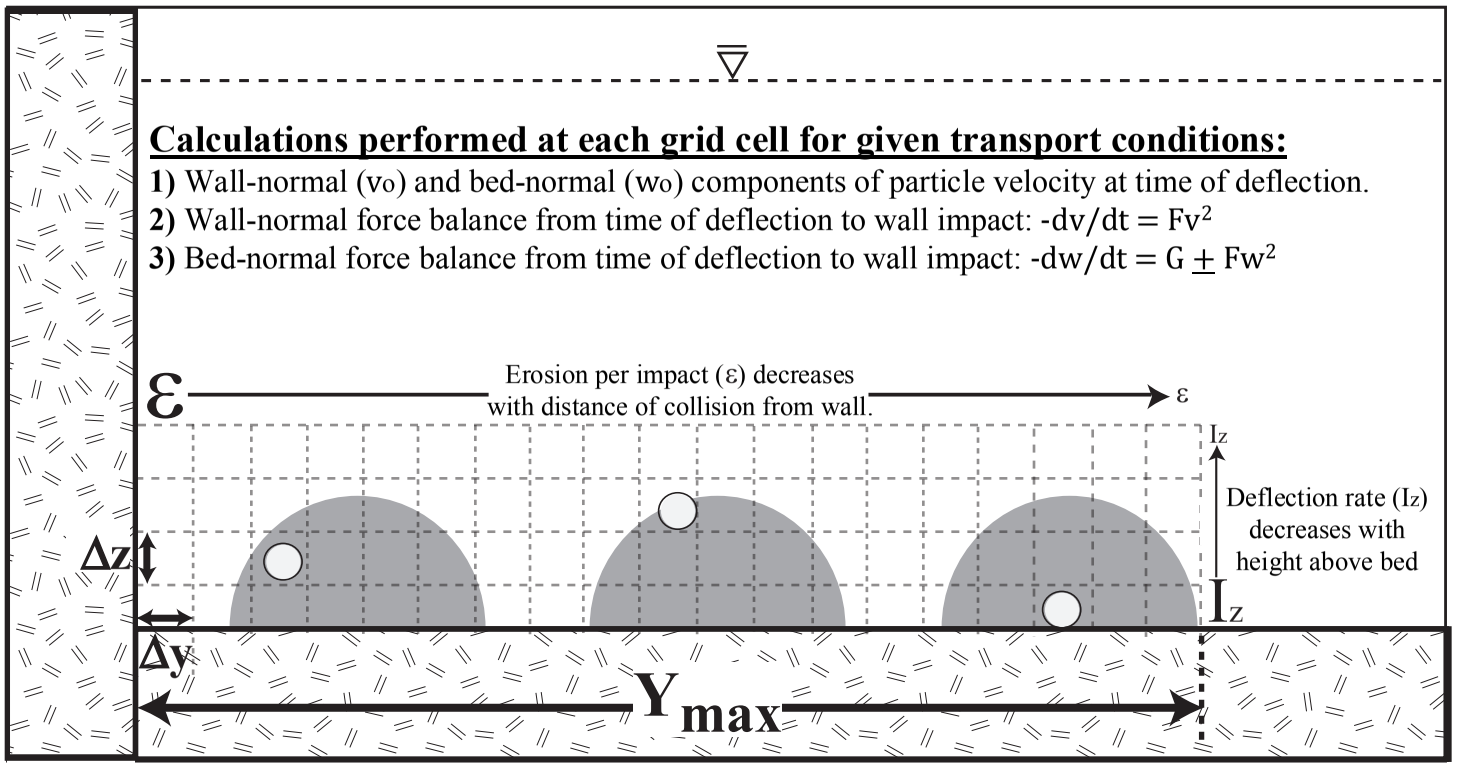

Figure 3.2 - Cross section perspective of the model framework, the calculations performed at each grid cell location and the dependence of the volume of wall material eroded per impact (ε) on the distance from the wall at which a collision occurs as well as the dependence of the rate of particle deflections (I_z) that occur within a given elevation interval (dz) on the elevation of that particular interval above the bed.

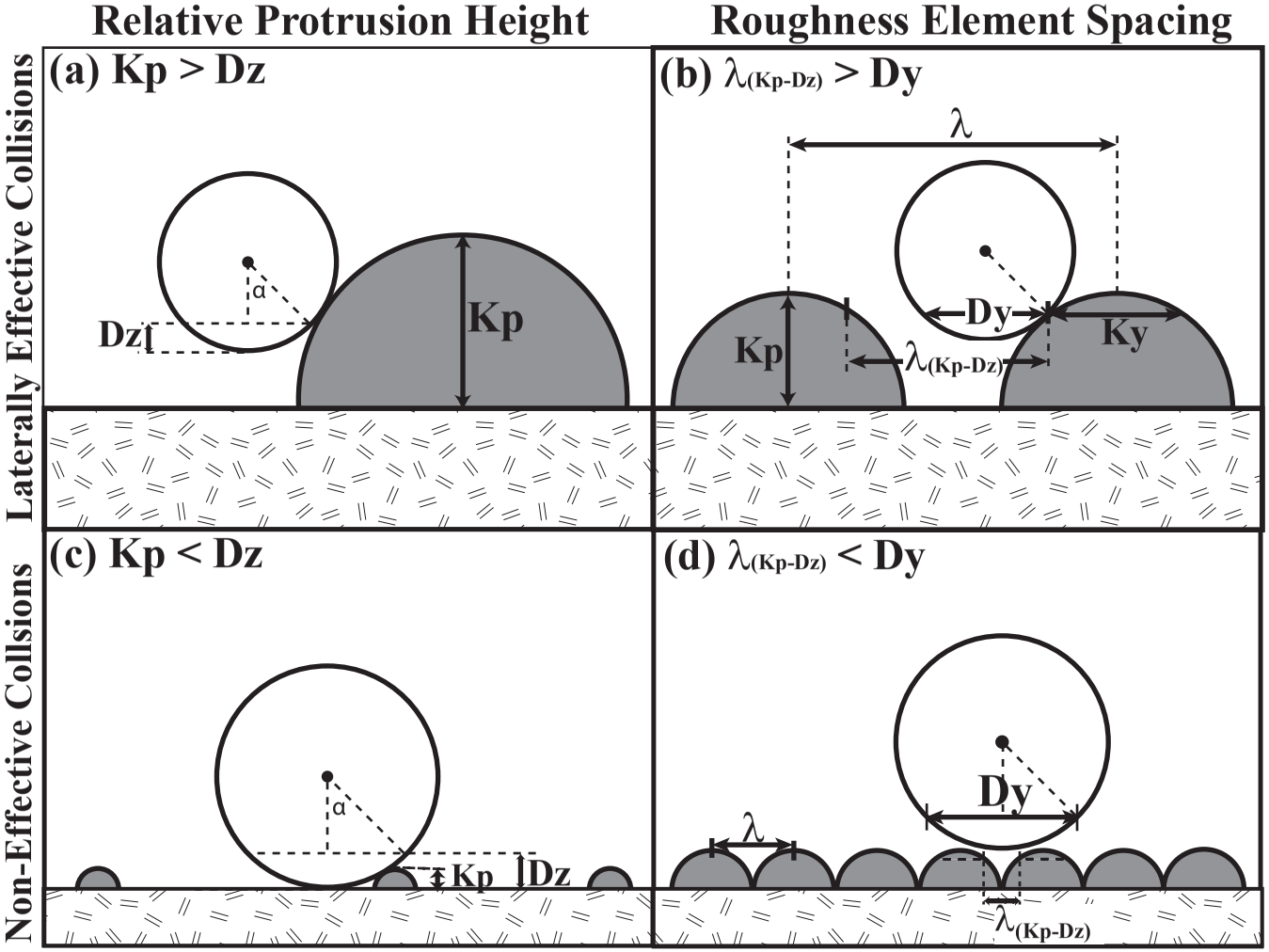

Figure 3.3 – Cross sectional perspectives of criteria for effective collisions. Scenarios (a) and (b) produce laterally effective collisions, scenarios (c) and (d) do NOT. Dz and Dy are the vertical and horizontal bed load length scales, Kp is protrusion height, λ (Kp-Dz) is space between elements at height Kp-Dz.

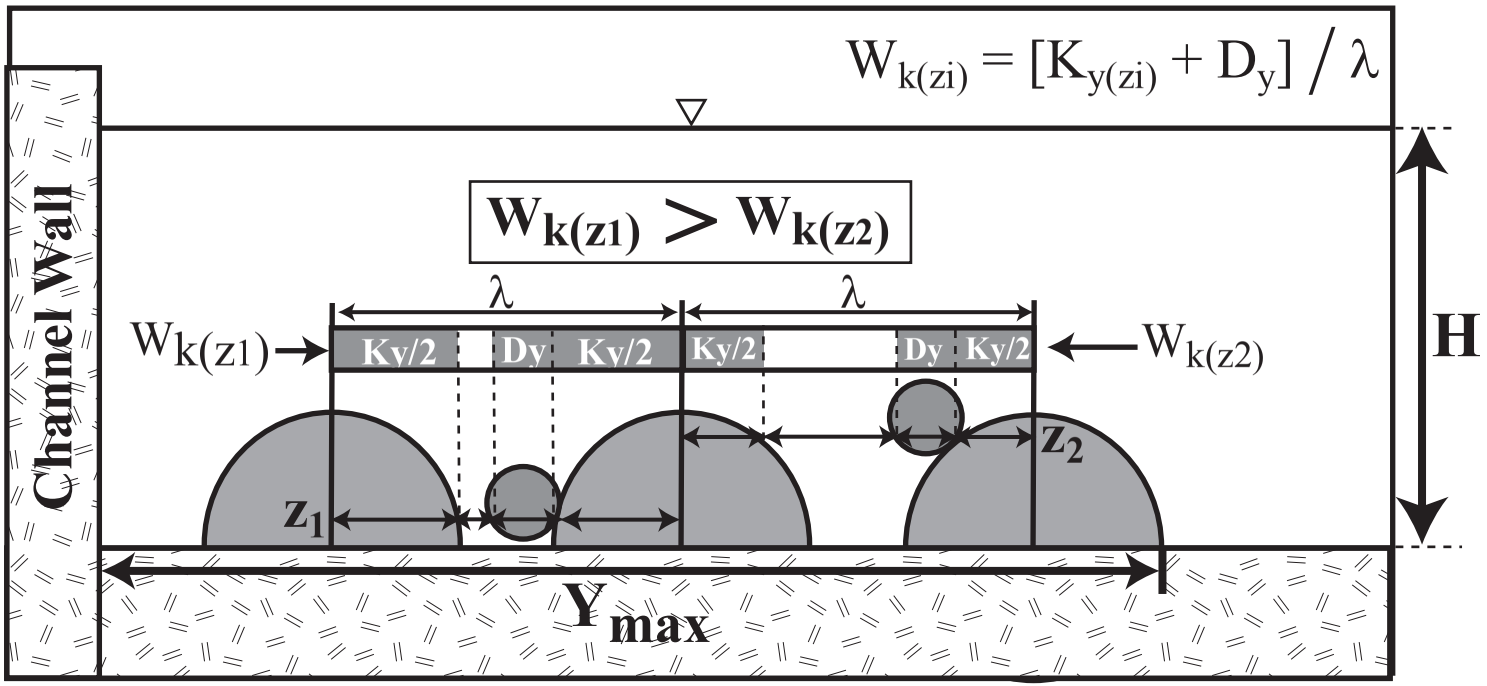

Figure 3.4 - Cross sectional perspective describing methodology used to estimate the likelihood of collisions (Wk(z)) between bed load particles and roughness elements. The likelihood of effective collisions is calculated as the ratio of space occupied by roughness elements at a given height (Ky) to the total space between roughness elements (lambda). Comparison of the left (Wk(z1)) and right (Wk(z2)) side of the figure show how the likelihood of collisions change as a function of height above the bed. Wk(z1) reflects the fractional width that is occupied by roughness element surfaces at an elevation near the bed and Wk(z2) reflects the fractional width occupied by roughness element surfaces at an elevation near the top of the roughness elements. Shaded lengths in the bar above the elements show the fractional width occupied by roughness elements and thus locations where collisions occur while unshaded lengths show the fractional width where no collisions occur.

Table 3.1 - Input Values and Calculated Transport Values

Roughness Element Size [mm]	Bed Load Particle Size [mm]	Flow Depth [mm]1	R_h [mm]	Channel Bed Slope	u_* [mm/s]	C_{f_sk}	τ_b [g/mms2]	τ_{sk} [g/mms2]	τ^*_c	τ_{sk}^*/τ^*_c	u_s [mm/s]	H_s [mm]
2.4	4.7	70	40	0.025	99	0.0064	0.97	0.65	0.045	1.9	373	5.9
4.7	4.7	69	38	0.025	96	0.0067	0.92	0.86	0.045	2.5	505	7.9
7.0	4.7	79	40	0.025	99	0.0061	0.97	0.63	0.045	1.8	354	5.7
10.0	4.7	79	42	0.025	101	0.0064	1.02	0.55	0.045	1.6	292	4.8
16.0	4.7	81	43	0.025	103	0.0064	1.05	0.49	0.045	1.4	229	3.9

[1]Flow depth estimated from pictures of physical experiments to ensure common method of measurement between roughness sections.

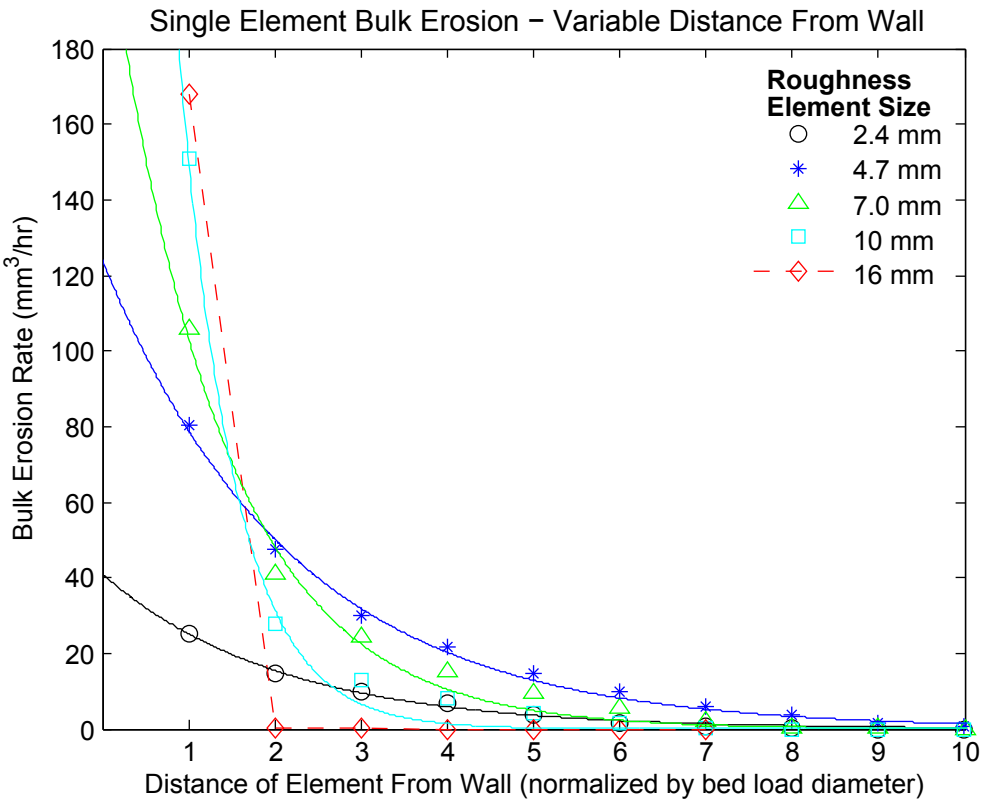

Figure 3.5 - Bulk erosion rate due to a single roughness element as a function of distance from the channel wall. Each data series represents a single roughness element size. Lines are an exponential fit to each data series (except for 16 mm).

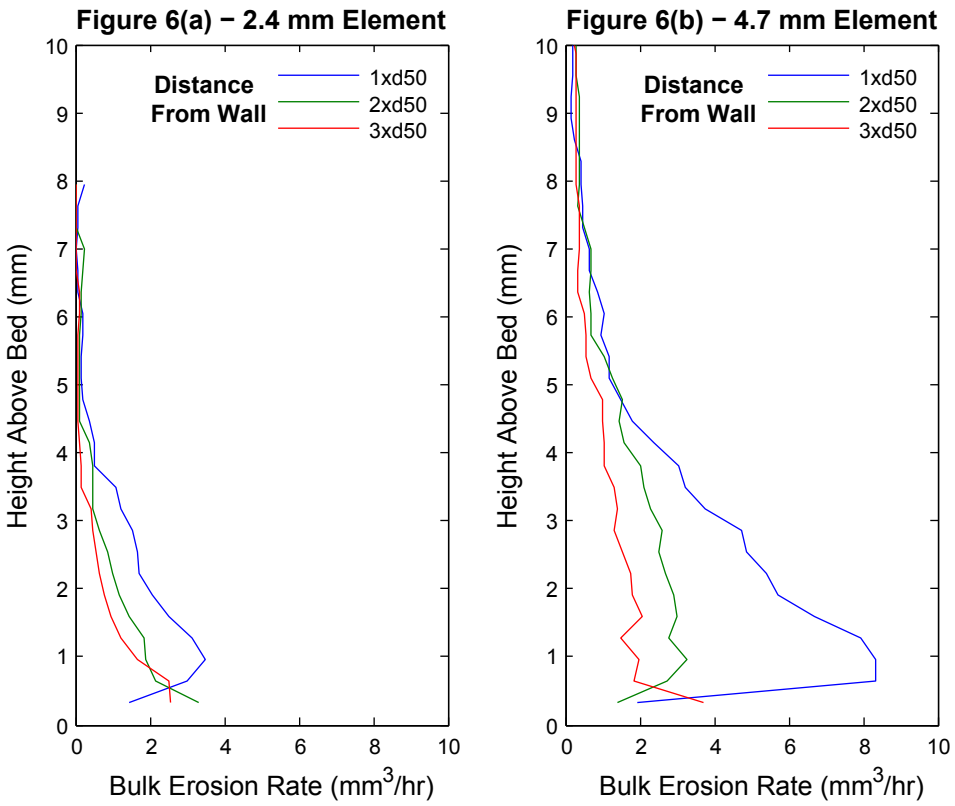

Figure 3.6 (a-b) Curves represent the vertical distribution of erosion from a single roughness element located a given distance from the channel wall. Each curve shows the vertical distribution of erosion from a single element at a given distance from the wall. Blue curve represents erosion from an element located near the wall (1 bed load particle diameter from the wall).Red curve represents erosion from an element located further away from wall (3 bed load particle diameters from wall).

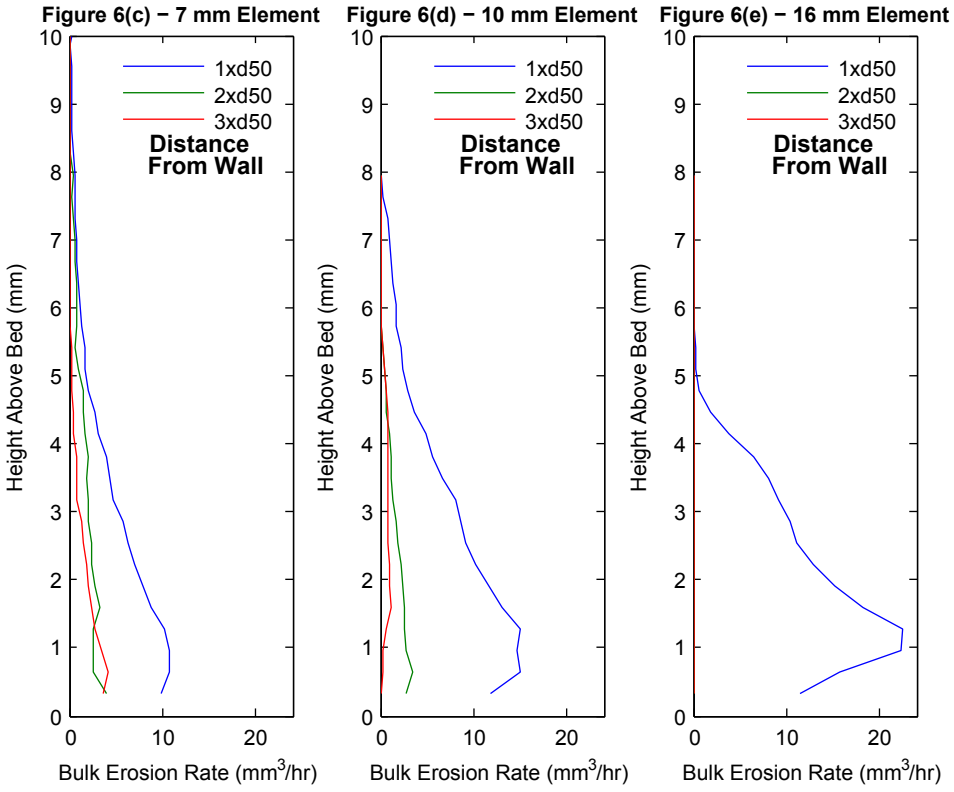

Figure 3.6(c-e) Curves represent the vertical distribution of erosion from a single roughness element located a given distancefrom the channel wall. Each curve shows the vertical distribution of erosion from a single element at a given distance fromthe wall. Blue curve represents erosion from an element located near the wall (1 bed load particle diameter from the wall).Red curve represents erosion from an element located further away from wall (3 bed load particle diameters from wall).

Figure 3.7 - (left) Undercut banks along a bedrock reach of the Kettle River near Sandstone Minnesota. This undercut morphology is similar to that predicted by the model. (right) Bank failure due to undercut channel banks driven by lateral bedrock erosion.

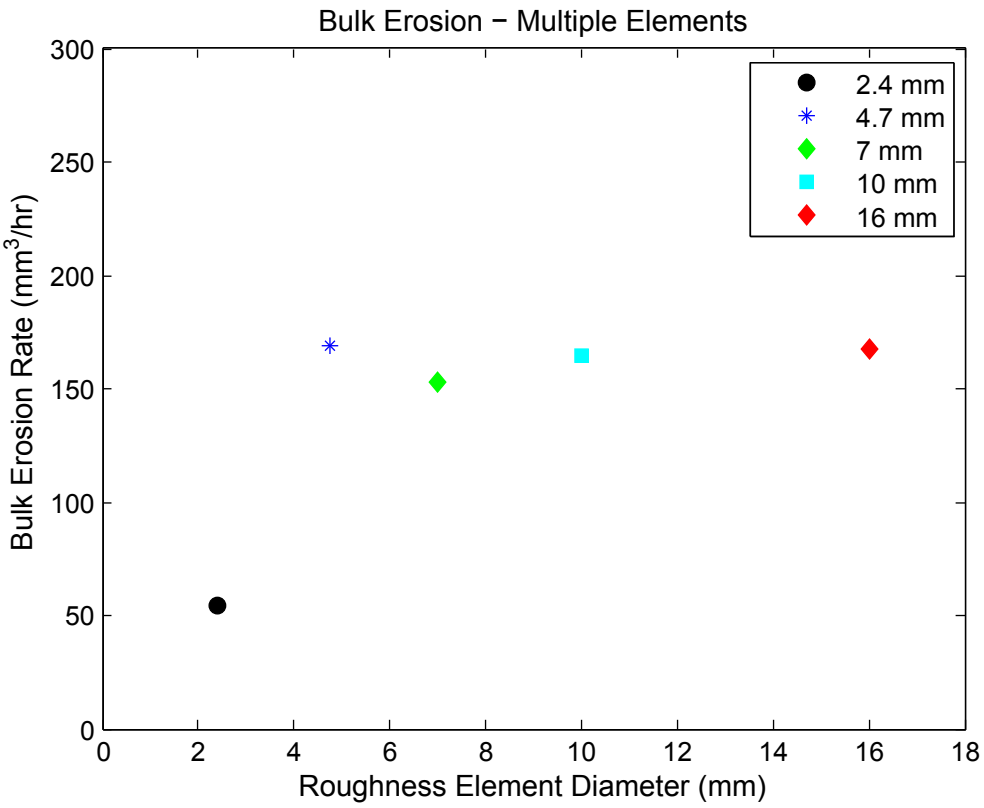

Figure 3.8 - Bulk erosion rates as a function of roughness element size for the case of multiple roughness element deflectors.Each data point reflects erosion from a channel bed composed of multiple roughness elements of a single size. The arealdensity of roughness elements was held constant across different roughness element sizes such that the space betweenindividual roughness elements increases along with the size of roughness

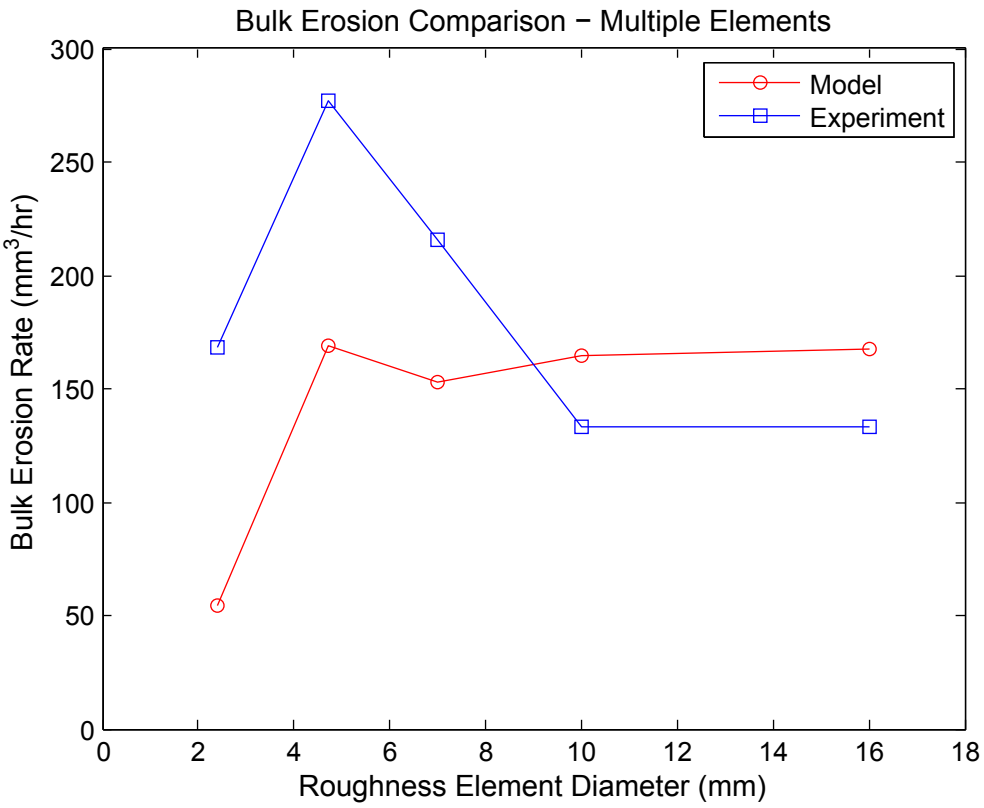

Figure 3.9 - Comparison of bulk erosion rates between experimental data (blue squares) and multiple element modelpredictions (red circles). The predicted model erosion rates show a similar trend as the size of the roughness elementincreases. The biggest discrepency between modeled and experimental erosion rates occurs when roughness elementsare relatively small.

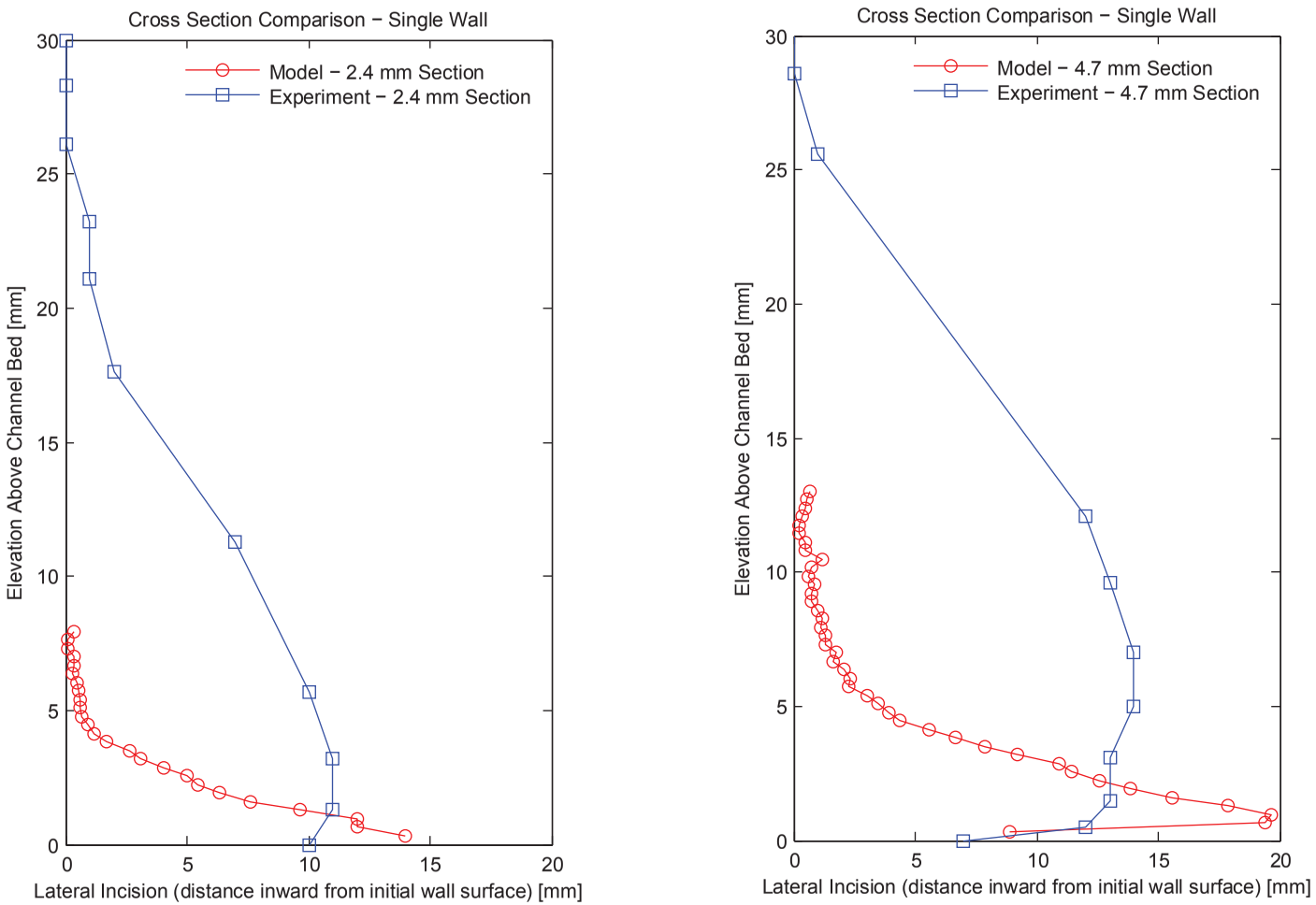

Figure 3.10 (a) - a comparison of the wall erosion profile in the 2.4 mm roughness element section between the model (red line) and the experiment (blue line) and (b) wall erosion profile comparison between the model (red line) and the experiment (blue line) for the 4.7 mm roughness element section. The experimental erosion profiles are from representative cross sections.

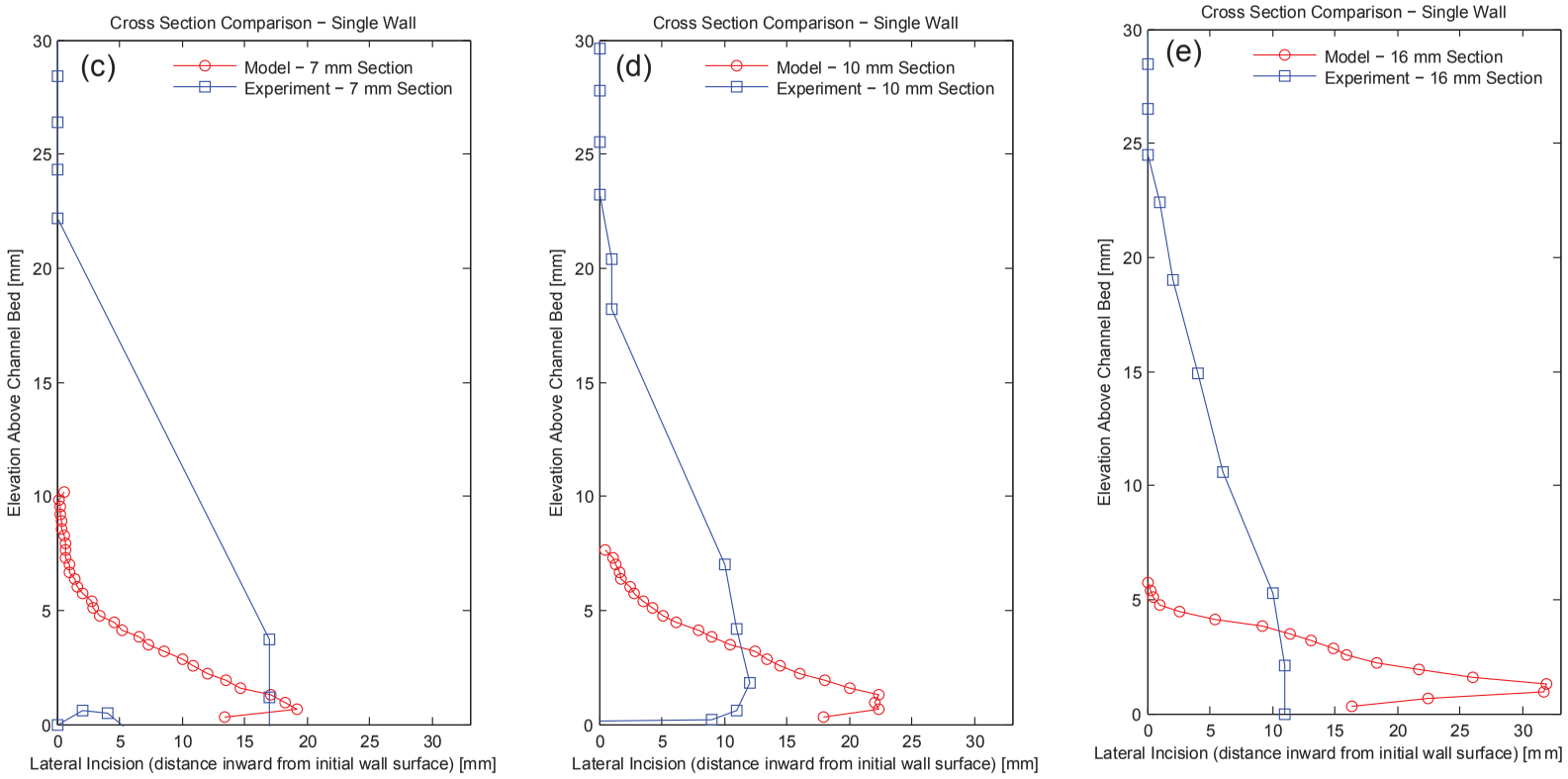

Figure 3.10(c-e) - comparison of wall erosion profiles between the model results (red line) and the physical experiments (blue line). (c) erosion profiles in the 7 mm roughness element section; (d) erosion profiles in the 10 mm roughness element section; (e) erosion profiles in the 16 mm roughness element section.

SUMMARY OF THESIS RESEARCH

Summary

An improved understanding of the mechanisms by which bedrock channels erode their walls will help the geomorphic community make progress on a number of important research fronts surrounding the morphodynamics of bedrock channels. Until now, the bedrock channel community has tried to understand what determines the width and cross sectional geometry of a bedrock channel with very limited knowledge of the processes that drive lateral erosion of bedrock channel walls [Finnegan et al., 2005; Carter and Anderson, 2006; Stark, 2006; Wobus et al., 2006]. Geomorphologists have tried to understand why bedrock channels migrate laterally across the landscape without a solid understanding of the mechanisms of lateral wall erosion [Bull, 1991; Hancock and Anderson, 2002]. In trying to understand what sets the width of a bedrock channel or how a bedrock channel maintains its channel geometry as it cuts down through uplifted rock, researchers have been relying on their knowledge of vertical incision of the channel bed [Whipple et al., 2000; Sklar and Dietrich, 2004]. But vertical incision is only one of the ways in which a channel can change its width or geometry. A better understanding of the process of lateral bedrock erosion will give researchers an extra degree of freedom with which to approach these important problems in bedrock channel morphodynamics. The overall goal of the research reported in this thesis is to develop an understanding of the mechanisms of lateral bedrock erosion and to understand what conditions within a channel facilitate or hinder these mechanisms.

Understanding the mechanisms of lateral erosion and the conditions that influence the efficacy of these mechanisms are intertwined. Field studies have suggested that lateral erosion becomes more efficient relative to vertical incision when relative sediment supply is increased [Gilbert, 1877; Personius, 1993]. But these studies have not suggested how an increase in relative sediment supply might influence the efficacy of lateral bedrock erosion processes. Establishing a link between these field observations and the efficacy of specific mechanisms of lateral erosion is a primary goal of the research presented in this thesis. To establish this link, we considered the change in channel conditions that might accompany an increase in relative sediment supply. One change typically associated with an increase in relative sediment supply is deposition of the sediment load on the channel bed. Sediment deposition can introduce changes in bed roughness.

In order to investigate the potential link between changes in sediment supply and the efficacy of specific lateral erosion mechanisms it was important to provide quantitative field evidence showing that rates of lateral erosion relative to vertical incision are indeed influenced by changes in sediment supply. To accomplish this first research goal, we set out to quantify erosion rates within a watershed at a time when mechanisms of lateral erosion were clearly outpacing mechanisms of vertical incision. Field evidence of such a scenario is preserved in the form of flat bedrock surfaces, or strath terraces, that are carved by laterally eroding bedrock channels at some time in the past. Strath surfaces clearly represent a case in which the channel conditions facilitate the mechanisms of lateral erosion while inhibiting those of vertical incision. Thus, quantifying erosion rates associated with a period of strath planation and comparing them to erosion rates associated with a period of vertical incision provides an excellent opportunity to quantify the effect of sediment supply (assumed to be correlated with the measured erosion rates) on the efficacy of mechanisms of lateral erosion.

Measuring the concentration of ^{10}Be in river-borne sediment deposited on top of strath surfaces allowed us to quantify the rate at which the watershed was eroding while the surfaces were being carved by a laterally eroding channel [Schaller et al., 2002]. We also measured the concentration of ^{10}Be in river-borne sediment from the modern channel, allowing us to quantify the rate at which the watershed was eroding during the most recent period of predominantly vertically oriented incision. A comparison of the rates at which the watershed was eroding during the two distinct erosion regimes, along with the assumption that basin-wide erosion rates are a good proxy for sediment supplied to the channel, enabled us to quantitatively show that during a period when the watershed was eroding twice as fast as the modern rate, conditions within the bedrock channel network favored mechanisms of lateral erosion relative to mechanisms of vertical incision. With quantitative field data showing that changes in sediment supply do indeed influence the relative efficacy of lateral versus vertical mechanisms of erosion, we were able to begin identifying channel conditions associated with changes in sediment supply that might encourage lateral erosion of the channel walls. The results from the field study enabled us to move forward in trying to establish links between previous field observations and channel conditions that might facilitate mechanisms of lateral bedrock erosion.

With evidence from our field study providing quantitative support that changes in sediment supply influence the relative effectiveness of lateral and vertical erosion mechanisms, we began to identify specific channel conditions that accompany variations in sediment supply that could influence mechanisms of lateral erosion. It has been demonstrated that changes in sediment supply result in changes in the size of sediment particles exposed on the bed [Dietrich et al., 1989; Lisle et al., 1993; Buffington et al., 2004; Nelson et al., 2009]. This change in particle size exposed on the bed represents a change in the grain scale roughness of the bed. Following this line of research, we set out to conduct a set of physical experiments designed to investigate how changes in grain scale bed roughness might influence the effectiveness of specific mechanisms of lateral bedrock erosion. For these experiments, we chose to investigate bedload particle impacts as our mechanism of lateral erosion. This choice was based on studies of vertical incision which suggested that bedload particle impacts were likely the most ubiquitous mechanism of vertical incision of the channel bed [Sklar and Dietrich, 2004].

During the set of physical experiments we held all channel input and channel geometry parameters constant except for the grain scale roughness on the bed. This allowed us to isolate the influence of channel bed roughness on the processes of driving bedload particles into the channel wall and to see if rates of lateral erosion remained constant or varied as a function of bed roughness. In order evaluate the influence of the size of roughness elements on the bed, we fixed sediment particles of a given size to a non-erodible bed to create distinct ‘roughness sections’ that maintained their roughness parameters throughout the duration of the experiment. Bed roughness ranged from ‘smooth’ channel sections (fine sand used to construct smooth sections was an order of magnitude finer than bedload particle size), to sections with roughness elements that 4 times the size of the bedload particle. To focus on bedload particle impacts as a potential mechanism, the experimental channels walls were constructed of an analog bedrock material that was resistant to erosion from the applied fluid shear stress but was readily erodible by bedload particle impacts.

The results from this set of physical experiments provide evidence for the following conclusions regarding specific mechanisms of lateral erosion and the potential variability of rates of lateral erosion. First, our results show that bedload particle impacts are an effective mechanism of lateral wall erosion. Second, our results indicate that collisions

between bedload particles and roughness elements on the bed play a critical role in driving bedload particles into the channel wall with enough kinetic energy to cause erosion. Through this collision and deflection process, channel bed roughness directly influences rates of lateral erosion. Third, we find that rates of lateral erosion increase 2 to 7 fold upon the introduction of 'effective' roughness elements to an otherwise smooth bed. Fourth, we find that there is minimum size of roughness element required to cause effective particle deflections. In dimensionless terms, the minimum roughness element size required for effective deflections appears to be about half the size of the bedload particle. Finally our experimental results show that once the minimum roughness element size is reached, further increases in the size of the roughness element do not cause rates of lateral erosion to continue to increase. Instead, rates of lateral erosion gradually stabilize as the size of the roughness element on the bed increases.

Our experimental results confirm what we found in the field in that changes in channel parameters (i.e. bed roughness) brought on by variations in sediment supply can influence the effectiveness of particular mechanisms of lateral erosion. This result is important to the study of strath terrace generation because it shows that the ability of a bedrock river to laterally carve a flat surface is not simply a function of that channel remaining at a fixed elevation because the channel is unable to incise its bed. Rather, our results suggest that rates of lateral erosion are variable and determining the ratio of vertical to lateral erosion rates in a bedrock channel is more complicated than simply turning vertical incision off and on. Our experimental results are also important for identifying an effective mechanism of lateral erosion which can be modeled and tested numerically to help validate and explore the details of this particular mechanism.

Based on the mechanism of lateral erosion identified in our experimental results, we have developed a numerical model of lateral bedrock erosion from first principles. We use this model to predict how rates of lateral erosion vary as a function of bed roughness. A primary goal of the model is to reproduce and confirm the variation in lateral erosion rates as a function of roughness element size that we observed in the physical experiments. In addition, if the deflection of bedload particles by roughness elements is the primary process driving lateral erosion via bedload impacts, the numerical model should be able to reproduce the undercut morphology observed in the set of physical experiments.

Using a force balance approach to track the change in both the lateral and vertical momentum of a deflected particle, the numerical model estimates the wall-normal impact velocity and the impact elevation associated with a collision at all effective collision locations within a cross section. Following the work of Sklar and Dietrich [2004], the numerical model estimates the volume of bedrock material removed per particle impact based on the wall-normal impact velocity. By calculating the volume of material removed per particle impact as well as the impact elevation associated with each effective collision location within a cross section, the model is able to calculate the bulk erosion and the vertical distribution of erosion for a given transport stage and bedload particle flux.

The bulk cross sectional erosion rates predicted by the model display the same trend as a function of roughness element size that was observed in the set of physical experiments. Specifically, the model predicts two important aspects of the erosion rate trend observed in the experiments: 1) a sharp increase in erosion rates with the addition of roughness elements to an otherwise smooth bed and 2) a stabilization in erosion rates as the size of the roughness element on the bed continues to increase beyond the minimum threshold size. In addition to predicting an erosion rate trend that is similar to the one observed in the set of physical experiments, the model also predicts that lateral erosion via particle impacts is concentrated within a narrow vertical range near the base of the channel wall. In doing so, the model predicts the undercut channel morphology that was observed in the physical experiments.

While confirming from first principles that the mechanism identified in the set of physical experiments is a viable mechanism of lateral bedrock erosion, the numerical model also provides valuable insight into the stabilization of erosion rates that was observed in the experiments. The stabilization of erosion rates likely represents a trade-off between an increase in the area available for collisions between bedload particles and larger roughness elements and a decrease in the shear stress available for bedload transport due to increased form drag associated with larger roughness elements.

The results from our field, experimental and numerical investigations into lateral bedrock erosion paint a coherent picture that improves the general understanding of how bedrock channels erode their banks and confining valley walls. Further exploration of how lateral erosion via deflected bedload particles responds to changes in sediment

supply, discharge and other external forcing mechanisms an important next step in the evolution of this line of research. The numerical model developed in chapter 3 is the logical starting place for this next step in our exploration of lateral bedrock erosion and we are hopeful it will provide exciting new research paths to explore just as our initial work in the field was able to provide an exciting path for us to follow as part of this research project.

BIBLIOGRAPHY

Adam, D. P. and G. J. West (1983), Temperature and precipitation estimates through the last glacial cycle from Clear Lake, California, pollen data, *Science, 219*(4581), 168-170.

Balco, G., J. O. Stone, N. A. Lifton, and T. J. Dunai (2008), A complete and easily accessible means of calculating surface exposure ages or erosion rates from ^{10}Be and (26)Al measurements, *Quaternary Geochronology, 3*(3), 174-195, doi:10.1016/j.quageo.2007.12.001.

Bitter, J. G. A. (1963), A study of erosional phenomena, part I, *Wear, 6*, 5-21.

Buffington, J., D. Montgomery, and H. Greenberg (2004), Basin-scale availability of salmonid spawning gravel as influenced by channel type and hydraulic roughness in mountain catchments, *Can. J. Fish. Aquat. Sci., 61*(11), 2085-2096, doi:10.1139/F04-141.

Bull, W. B. (1991), *Geomorphic responses to climatic change*, Oxford Univ. Press, New York, NY, United States (USA), United States (USA).

Capart, H. and L. Fraccarollo (2011), Transport layer structure in intense bed-load, *Journal of Geophysical Research-Earth Surface, 38,* L20402, doi:10.1029/2011 GL049408

Carter, C. L. and R. S. Anderson (2006), Fluvial erosion of physically modeled abrasion-dominated slot canyons, *Geomorphology, 81*(1-2), 89-113, doi:10.1016/j.geomorph.2006.04.006.

DeVecchio, D. E., R. V. Heermance, M. Fuchs, and L. A. Owen (2012), Climate-controlled landscape evolution in the Western Transverse Ranges, California: Insights from Quaternary geochronology of the Saugus Formation and strath terrace flights, *Lithosphere, 4*(2), 110-130, doi:10.1130/L176.1.

Dietrich, W., J. Kirchner, H. Ikeda, and F. Iseya (1989), Sediment Supply and the Development of the Coarse Surface-Layer in Gravel-Bedded Rivers, *Nature, 340*(6230), 215-217, doi:10.1038/340215a0.

Finnegan, N. J., L. S. Sklar, and T. K. Fuller (2007), Interplay of sediment supply, river incision, and channel morphology revealed by the transient evolution of an experimental bedrock channel, *Journal of Geophysical Research-Earth Surface, 112*(F3), doi:10.1029/2006JF000569 ER.

Finnegan, N., G. Roe, D. Montgomery, and B. Hallet (2005), Controls on the channel width of rivers: Implications for modeling fluvial incision of bedrock, *Geology, 33*(3), 229-232, doi:10.1130/G21171.1.

Finnegan, N. J. and W. E. Dietrich (2011), Episodic bedrock strath terrace formation due to meander migration and cutoff, *Geology, 39*(2), 143-146, doi:10.1130/G31716.1.

Fuller, T. K., L. A. Perg, J. K. Willenbring, and K. Lepper (2009), Field evidence for climate-driven changes in sediment supply leading to strath terrace formation, *Geology, 37*(5), 467-470, doi:10.1130/G25487A.1 ER.

Gabet, E., B. Pratt-Sitaula, and D. Burbank (2004), Climatic controls on hillslope angle and relief in the Himalayas, *Geology, 32*(7), 629-632, doi:10.1130/G20641.1.

Gilbert, G. K. (1877), *Report on the Geology of the Henry Mountains: Geographical and Geological Survey of the Rocky Mountain Region*, U.S. Gov. Print Office, Washington, D.C.

Hancock, G. S. and R. S. Anderson (2002), Numerical modeling of fluvial strath-terrace formation in response to oscillating climate, *Geological Society of America Bulletin, 114*(9), 1131-1142, doi:10.1130/0016-7606(2002)114<1131:NMOFST>2.0.CO;2.

Hilley, G., R. Burgmann, A. Ferretti, F. Novali, and F. Rocca (2004), Dynamics of slow-moving landslides from permanent scatterer analysis, *Science, 304*(5679), 1952-1955, doi:10.1126/science.1098821.

Howard, A. D. (1994), A Detachment-Limited Model of Drainage-Basin Evolution, *Water Resour. Res., 30*(7), 2261-2285.

Howard, A. and G. Kerby (1983), Channel Changes in Badlands, *Geological Society of America Bulletin, 94*(6), 739-752, doi:10.1130/0016-7606(1983)94<739:CCIB>2.0.CO;2.

Jayco, A. S., M. C. Blake, R. J. McLaughlin, H. N. Ohlin, S. D. Ellen, and H. M. and Kelsey (1989), Reconnaissance geologic map of the Covelo I:l00,000 quadrangle: U.S. Geological Survey Miscellaneous Field Investigations Map, *1:100,000*.

Kohl, C. P. and K. Nishiizumi (1992), Chemical isolation of quartz for measurement of in-situ-produced cosmogenic nuclides, *Geochim. Cosmochim. Acta, 56*(9), 3583-3587.

Lal, D. (1991), Cosmic ray labeling of erosion surfaces; in situ nuclide production rates and erosion models, *Earth Planet. Sci. Lett., 104*(2-4), 424-439.

Lamb, M. P., W. E. Dietrich, and L. S. Sklar (2008), A model for fluvial bedrock incision by impacting suspended and bedload sediment, *J. Geophys. Res. -Earth Surf., 113*(F3), F03025, doi:10.1029/2007JF000915.

Larson, P.H., R.I. Dorn, J. Douglass, B.F. Gootee, and R. Arrowsmith (2010), Stewart mountain terrace: A new salt river terrace with implications for landscape evolution of the lower salt river valley, Arizona, Journal of the Arizona-Nevada Academy of Science 42(1): 26-35.

Lee, S.Y., Y.B. Seong, Y.K. Shin, K.H. Choi, H.C. Kang, and J.H. Choi (2011), Cosmogenic ^{10}Be and OSL dating of fluvial strath terraces along theOsip-cheon River, Korea: tectonic implications, *Geosciences Journal,* Vol. 15, No. 4, DOI 10.1007/s12303-011-0036-6

Lepper, K., T. G. Fisher, I. Hajdas, and T. V. Lowell (2007), Ages for the Big Stone Moraine and the oldest beaches of glacial Lake Agassiz; implications for deglaciation chronology, *Geology (Boulder), 35*(7), 667-670, doi:10.1130/G23665A.1.

Lisle, T., F. Iseya, and H. Ikeda (1993), Response of a Channel with Alternate Bars to a Decrease in Supply of Mixed-Size Bed-Load - a Flume Experiment, *Water Resour. Res., 29*(11), 3623-3629, doi:10.1029/93WR01673.

Mackey, B., J. Roering, J. McKean, and W. Dietrich (2006), Analyzing the Spatial Pattern of Deep-Seated Landsliding Evidence for Base Level Control, South Fork Eel River, California, paper presented at AGU Fall Meeting Abstracts.

Merritts, D. J., K. R. Vincent, and E. E. Wohl (1994), Long river profiles, tectonism, and eustasy; a guide to interpreting fluvial terraces, *Journal of Geophysical Research, 99*(B7), 14-14,050.

Montgomery, D. R. (2004), Observations on the role of lithology in strath terrace formation and bedrock channel width, *Am. J. Sci., 304*(5), 454-476.

Montgomery, D. and K. Gran (2001), Downstream variations in the width of bedrock channels, *Water Resour. Res., 37*(6), 1841-1846, doi:10.1029/2000WR900393.

Nelson, P. A., J. G. Venditti, W. E. Dietrich, J. W. Kirchner, H. Ikeda, F. Iseya, and L. S. Sklar (2009), Response of bed surface patchiness to reductions in sediment supply, *Journal of Geophysical Research-Earth Surface, 114*, F02005, doi:10.1029/2008JF001144.

Niemi, N. A., M. Oskin, D. W. Burbank, A. M. Heimsath, and E. J. Gabet (2005), Effects of bedrock landslides on cosmogenically determined erosion rates, *Earth Planet. Sci. Lett., 237*(3-4), 480-498, doi:10.1016/j.epsl.2005.07.009.

Nino, Y., M. Garcia, and L. Ayala (1994), Gravel Saltation .1. Experiments, *Water Resour. Res., 30*(6), 1907-1914, doi:10.1029/94WR00533.

Parker, G. (2004), 1-D Sediment transport morphodynamics with applications to rivers and turbidity currents, http://hydrolab.illinois.edu/people/parkerg//morphodynamics_e-book.htm

Personius, S. F., H. M. Kelsey, and P. C. Grabau (1993), Evidence for regional stream aggradation in the central Oregon Coast Range during the Pleistocene-Holocene transition, *Quatern. Res., 40*(3), 297-308.

Reneau, S. L. (2000), Stream incision and terrace development in Frijoles Canyon, Bandelier National Monument, New Mexico, and the influence of lithology and climate, *Geomorphology, 32*(1-2), 171-193.

Schaller, M., F. von Blanckenburg, A. Veldkamp, L. A. Tebbens, N. Hovius, and P. W. Kubik (2002), A 30 000 yr record of erosion rates from cosmogenic ^{10}Be in middle European river terraces, *Earth Planet. Sci. Lett., 204*(1-2), 307-320.

Schaller, M., F. von Blanckenburg, N. Hovius, A. Veldkamp, M. W. van den Berg, and P. W. Kubik (2004), Paleoerosion rates from cosmogenic ^{10}Be in a 1.3 Ma terrace sequence; response of the River Meuse to changes in climate and rock uplift, *J. Geol., 112*(2), 127-144.

Schmeeckle, M., J. Nelson, J. Pitlick, and J. Bennett (2001), Interparticle collision of natural sediment grains in water, *Water Resour. Res., 37*(9), 2377-2391, doi:10.1029/2001WR000531.

Seidl, M. A. and W. E. Dietrich (1992), The problem of channel erosion into bedrock; Functional geomorphology; landform analysis and models, *Catena Supplement, 23*, 101-124.

Shepherd, R. G. and S. Schumm (1974), Experimental study of river incision, *Geological Society of America bulletin, 85*(2), 257, doi:10.1130/0016-7606(1974)85<257:ESORI>2.0.CO 2.

Sklar, L. S. and W. E. Dietrich (2001), Sediment and rock strength controls on river incision into bedrock, *Geology (Boulder), 29*(12), 1087-1090.

Sklar, L. S. and W. E. Dietrich (2004), A mechanistic model for river incision into bedrock by saltating bedload, *Water Resour. Res., 40*(6), 21, doi:10.1029/2003WR002496.

Sklar, L. S. and W. E. Dietrich (2006), The role of sediment in controlling steady-state bedrock channel slope: Implications of the saltation-abrasion incision model, *Geomorphology, 82*(1-2), 58-83, doi:10.1016/j.geomorph.2005.08.019.

Stark, C. P. (2006), A self-regulating model of bedrock river channel geometry, *Geophys. Res. Lett., 33*(4), doi:10.1029/2005GL023193 ER.

Stark, C. P., J. R. Barbour, Y. S. Hayakawa, T. Hattanji, N. Hovius, H. Chen, C. Lin, M. Horng, K. Xu, and Y. Fukahata (2010), The Climatic Signature of Incised River Meanders, *Science, 327*(5972), 1497-1501, doi:10.1126/science.1184406.

Stock, J. D., D. R. Montgomery, B. D. Collins, W. E. Dietrich, and L. S. Sklar (2005), Field measurements of incision rates following bedrock exposure; implications for process controls on the long profiles of valleys cut by rivers and debris flows, *Geological Society of America Bulletin, 117*(1-2), 174-194, doi:10.1130/B25560.1.

Stone, J. O. (2000), Air pressure and cosmogenic isotope production, *Journal of Geophysical Research, 105*(B10), 23-23,759.

Suzuki, T. (1982), Rate of lateral planation by Iwaki River, Japan, *Trans.Jpn.Geomorphol.Union, 3*(1), 1-24.

Turowski, J. M., D. Lague, and N. Hovius (2007), Cover effect in bedrock abrasion: A new derivation and its implications for the modeling of bedrock channel morphology, *Journal of Geophysical Research-Earth Surface, 112*(F4), F04006, doi:10.1029/2006JF000697.

Wegmann, K. W. and F. J. Pazzaglia (2002), Holocene strath terraces, climate change, and active tectonics; the Clearwater River basin, Olympic Peninsula, Washington State, *Geological Society of America Bulletin, 114*(6), 731-744.

Wegmann, K. W. and F. J. Pazzaglia (2009), Late Quaternary fluvial terraces of the Romagna and Marche Apennines, Italy: Climatic, lithologic, and tectonic controls on terrace genesis in an active orogen, *Quaternary Science Reviews, 28*(1-2), 137-165, doi:10.1016/j.quascirev.2008.10.006.

Whipple, K., G. Hancock, and R. Anderson (2000), River incision into bedrock: Mechanics and relative efficacy of plucking, abrasion, and cavitation, *Geological Society of America Bulletin, 112*(3), 490-503, doi:10.1130/0016-7606(2000)112<0490:RIIBMA>2.3.CO;2.

Wiberg, P. L. and J. D. Smith (1985), A Theoretical-Model for Saltating Grains in Water, *Journal of Geophysical Research-Oceans, 90*(NC4), 7341-7354.

Wobus, C. W., G. E. Tucker, and R. S. Anderson (2006), Self-formed bedrock channels, *Geophys. Res. Lett., 33*(18), doi:10.1029/2006GL027182 ER.

Wohl, E. and H. Ikeda (1997), Experimental simulation of channel incision into a cohesive substrate at varying gradients, *Geology, 25*(4), 295-298, doi:10.1130/0091-7613(1997)025<0295:ESOCII>2.3.CO;2.

Wolfram Alpha LLC. 2011. Wolfram|Alpha.

http://www.wolframalpha.com/input/?i=2%2B2 (access July 10, 2011).

APPENDIX TABLES

Appendix 1.1 - Cosmogenic ^{10}Be Sample Data

		Basin Averaged		Scaling Factors				Inheritance Production Rates[5]			Sample Site			Post-Depositional Production Rates			Raw Geochemical Data[6]	
		Latitude[1]	Altitude[2]	Preliminary[3]		Corrected[4]		$P_{0,n}$	P_{0,μ_stop}	P_{0,μ_fast}	Lat	Long	Altitude	$P_{0,n}$	P_{0,μ_stop}	P_{0,μ_fast}	Sample Mass	^{10}Be
Sample ID & Type	Location	(dd)	(m)	S_λ	M_λ	S_λ	M_λ	(atoms/g/yr)	(atoms/g/yr)	(atoms/g/yr)	(dd)	(dd)	(m)	(atoms/g/yr)	(atoms/g/yr)	(atoms/g/yr)	(g)	(atoms)
Modern																		
001	Ten Mile	39.7	665	1.69	1.29	1.64	1.25	7.13	0.108	0.095	39.76	-123.62	357	-	-	-	40.02	1,745,777
003	Elder	39.7	865	1.99	1.41	1.95	1.38	8.44	0.119	0.105	39.73	-123.63	441	-	-	-	20.03	1,367,014
004	Elder	39.7	799	1.89	1.37	1.86	1.35	8.05	0.116	0.102	39.73	-123.65	388	-	-	-	20.02	1,418,986
010	SF Eel	39.7	649	1.66	1.28	1.65	1.27	7.15	0.109	0.096	39.72	-123.65	395	-	-	-	40.04	1,840,247
011	SF Eel	39.7	661	1.68	1.28	1.66	1.27	7.22	0.110	0.096	39.73	-123.64	377	-	-	-	39.99	1,740,054
012	SF Eel	39.7	661	1.68	1.28	1.66	1.27	7.22	0.110	0.096	39.75	-123.63	345	-	-	-	20.14	1,383,546
JOH-21	JOH	39.7	585	1.57	1.24	1.55	1.22	6.73	0.105	0.092	39.72	-123.65	393	-	-	-	40.05	1,743,568
Lower & Middle Strath																		
002	Elder	39.7	801	1.89	1.37	1.85	1.34	8.03	0.116	0.102	39.73	-123.65	399	-	-	-	23.89	1,015,324
009	Elder	39.7	795	1.89	1.37	1.85	1.34	8.03	0.116	0.102	39.73	-123.65	390	-	-	-	26.17	758,029
014	SF Eel	39.7	661	1.68	1.28	1.66	1.27	7.22	0.110	0.096	39.73	-123.65	385	5.75	0.0971	0.0852	41.10	2,815,930
015	SF Eel	39.7	661	1.68	1.28	1.66	1.27	7.22	0.110	0.096	39.73	-123.65	383	5.75	0.0970	0.0851	35.82	3,312,677
016	SF Eel	39.7	661	1.68	1.28	1.66	1.27	7.22	0.110	0.096	39.73	-123.65	382	5.74	0.0970	0.0851	35.28	1,205,970
019	SF Eel	39.7	661	1.68	1.28	1.66	1.27	7.22	0.110	0.096	39.75	-123.63	348	5.57	0.0954	0.0837	42.11	1,801,491
JOH-06	JOH	39.7	585	1.57	1.24	1.55	1.22	6.73	0.105	0.092	39.72	-123.65	401	5.83	0.0978	0.0858	67.68	2,198,415
Upper Strath																		
006	Elder	39.7	809	1.91	1.38	1.87	1.35	8.11	0.117	0.102	39.73	-123.64	404	5.85	0.0980	0.0860	29.37	954,476
013	SF Eel	39.7	661	1.68	1.28	1.66	1.27	7.22	0.110	0.096	39.73	-123.65	389	5.77	0.0973	0.0853	21.68	519,849

[1]A latitude of 40° was used for all samples to calculate the scaling factors based on the equations in Stone, 2000

[2]Altitude is shown as a reference but was not used in calculation as all calculations were performed for each grid cell in the basin and then average

[3]Calculated for each grid cell in the basin and then averaged. S_λ and M_λ are the scaling factors for production due to spallation and muon capture respectively.

[4]Reflects the scaling factors after a correction for topographic shielding. These corrected scaling factors were used to calculate the production rates

[5]Based on a SLHL total production rate of 4.5 atoms g^{-1} yr^{-1} and production equations of Stone (2000). The fraction due to spallogenic production (f_s) is 0.964 based on Schaller, 2002.

[6]Blank values: modern samples = 555,288 atoms; strath samples 002, 014 and 015 = 123,287 atoms; other strath samples = 82,017 atoms

Appendix 1.2. - OSL dating results.

TCN ID	OSL ID	N[1]	M/m[2]	Equivalent Dose[3] (Gy)	Dose Rate (Gy/ky)	OSL Age (ky)
006	ELD-05	19/20	1.00	79.62 ± 5.94	2.395 ± 0.210	33.3 ± 4.1
013	SFG-25	93/96	1.03	46.42 ± 1.85	2.265 ± 0.142	20.5 ± 3.3
014	SFI-24	97/99	1.04	27.65 ± 1.02	2.353 ± 0.181	11.8 ± 1.1
015	SFK-23	89/92	1.06	22.30 ± 1.06	2.418 ± 0.159	9.2 ± 0.8
016	SFN-22	47/48	1.04	19.58 ± 0.88	2.366 ± 0.161	8.3 ± 0.8
019	SFE-20	62/64	1.02	12.35 ± 0.47	1.927 ± 0.215	6.4 ± 0.8
JOH-06	JOH-07	108/110	1.08	14.54 ± 0.47	1.943 ± 0.119	7.5 ± 0.6

[1]Number of aliquots suitable for analysis / number of aliquots measured; governed by the amount of clean quartz that could be extracted from each sample.
[2]Mean/median ratio used as a measure of asymmetry (see Lepper et al., 2007).
[3]Mean and std. err. used in all cases except JOH-07, the distribution with the highest asymmetry, in which case the “leading edge” dose was used (see Lepper et al., 2007).

Appendix 1.3. Sample depth and concentrations of dosimetrically significant elements.

OSL ID	Sample depth (cm)	[K] (ppm)	[Rb] (ppm)	[Th] (ppm)	[U] (ppm)
ELD-05	150	15908 ± 2233	67.75 ± 9.31	5.779 ± 0.494	2.522 ± 0.275
SFG-25	644	15505 ± 1388	76.67 ± 8.97	5.636 ± 0.448	2.318 ± 0.310
SFI-24	415	16190 ± 1959	64.39 ± 7.62	6.220 ± 0.507	2.307 ± 0.242
SFK-23	369	16319 ± 1657	69.39 ± 8.07	6.229 ± 0.509	2.521 ± 0.257
SFN-22	318	16377 ± 1709	79.04 ± 7.76	5.873 ± 0.475	2.325 ± 0.232
SFE-20	130	10521 ± 2288	77.21 ± 6.57	6.276 ± 0.500	2.236 ± 0.213
JOH-07	180	11227 ± 1101	58.88 ± 6.99	5.564 ± 0.456	1.941 ± 0.206

Elemental analysis by INAA performed at the Ohio State University Research Reactor.
Pore water content of 12±3% used for all samples.
Beta attenuation coefficient of 0.90 was used for all samples corresponding to the grain size range 90-250 μm.